ENERGY RESOLVED DIFFRACTION FOR INVESTIGATING X-RAY PARAMETRIC DOWN-CONVERSION

DISSERTATION ZUR ERLANGUNG DES DOKTORGRADES
DES FACHBEREICHES PHYSIK
DER UNIVERSITÄT HAMBURG

vorgelegt von

CHRISTINA BÖMER

Hamburg
2020

Promotionsinformationen

Gutachter der Dissertation:	Prof. Dr. Christian Bressler Prof. Dr. Nina Rohringer
Gutachter der Disputation:	Prof. Dr. Christian Bressler Prof. Dr. Nina Rohringer Prof. Dr. Ralf Röhlsberger Prof. Dr. Robert Feidenhans'l Prof. Dr. Daniela Pfannkuche
Datum der Disputation:	21.09.2020
Vorsitzender des Fach-Promotionsausschusses:	Prof. Dr. Günter H. W. Sigl
Leiter des Fachbereiches Physik:	Prof. Dr. Wolfgang Hansen
Dekan der Fakultät für Mathematik, Informatik und Naturwissenschaften:	Prof. Dr. Heinrich Graener

Abstract

This thesis covers the nonlinear process of parametric down-conversion in the x-ray regime. It provides an extensive review of x-ray frequency conversion phenomena - covering theoretical and experimental studies. It focuses specifically on the investigation of parametric down-conversion of x-rays into visible photons. With the aim to identify and investigate the effect's characteristic scattering signature, an energy-resolved diffraction setup is implemented at different synchrotron sources. The nonlinear process is experimentally investigated by a systematic mapping of its parameter space, yet the effect's anticipated signature is not observed in the measured scattering patterns. Instead, the intensity distributions therein are attributed to regular elastic scattering. This identification is achieved on the basis of instrumental function considerations as known from high-resolution x-ray diffractometry and comparable reciprocal space map studies. Nevertheless, the achieved resolution of the experimental setup allows a new determination of an upper bound of the effect's conversion efficiency. The results are fully compatible with novel theoretical approaches to x-ray optical wave-mixing based on quantum electrodynamics. These results are in stark contrast to earlier experimental studies that identify similar scattering signals as parametrically generated photons. As such, the methodology developed in this thesis will serve to revisit these reports with increased accuracy and - beyond that - provide the basis for future studies and applications of x-ray nonlinearities. In particular, its conclusions provide a clear path of optimizations to achieve the outstanding proof of parametric down-conversion of x-rays into visible photons.

Kurzzusammenfassung

Diese Arbeit behandelt den nichtlinearen Prozess der parametrischen Abwärtskonvertierung von Röntgenlicht. Sie bietet einen umfassenden Überblick über die theoretischen und experimentellen Studien der Röntgen-Frequenzumwandlung. Sie konzentriert sich speziell auf die Untersuchung der parametrischen Abwärtskonvertierung von Röntgenstrahlen in sichtbare Photonen. Mit dem Ziel, die charakteristische Streusignatur des Effekts zu identifizieren und zu untersuchen, wird ein energieaufgelöster Beugungsaufbau an verschiedenen Synchrotronquellen implementiert. Der nichtlineare Prozess wird experimentell durch eine systematische Kartierung seines Parameterraums untersucht, doch die erwartete Signatur wird in den gemessenen Streumustern nicht beobachtet. Stattdessen werden die darin enthaltenen Intensitätsverteilungen auf regelguläre elastische Streuung zurückgeführt. Diese Identifizierung erfolgt auf der Grundlage von Instrumentenfunktionen, wie sie aus der hoch-auflösenden Röntgendiffraktometrie und vergleichbaren reziproken Raumkartenstudien bekannt sind. Dennoch erlaubt das Auflösungsvermögen des experimentellen Aufbaus die Bestimmung einer neue oberen Grenze für die Konversionseffizienz des Effekts. Die Ergebnisse sind kompatibel mit neuen theoretischen Ansätzen zur röntgenoptischen Wellenmischung, die auf Quantenelektrodynamik basieren. Diese Ergebnisse stehen in starken Gegensatz zu früheren experimentellen Studien, die ähnliche Streusignale als parametrisch erzeugte Photonen identifizieren.
Daher wird die in dieser Arbeit entwickelte Methodik dazu dienen, jene Studien mit erhöhter Genauigkeit zu überprüfen und - darüber hinaus - die Grundlage für zukünftige Experimente und Anwendungen von Röntgen-Nichtlinearitäten schaffen. Insbesondere bieten die Schlussfolgerungen einen klaren Weg für Optimierungen, um den austehenden Nachweis der parametrischen Abwärtskonvertierung von Röntgenstrahlen in sichtbare Photonen zu erreichen.

Contents

Chapter 1

Introduction

The nature of light-matter interactions is manifold and exhibits various phenomena that are yet unexplored. Among these are the x-ray wave mixing processes, in which the energy of the participating photons is redistributed during their interaction with the material. These nonlinear phenomena are pertubative multiphoton processes and intrinsically yield low conversion rates. The systematic investigation of these effects is thereby becoming accessible by the ascent of highly brilliant x-ray sources.
Of specific interest is the spontaneous down-conversion of x-rays (XPDC), in which one photon is converted into a correlated pair of lower energy photons. The initial photon energy can be distributed symmetrically or asymmetrically among the down-converted pair, allowing a continuous distribution of energy in the latter case. Specifically for the largely unexplored asymmetric regime, this study on the XPDC process is motivated by the intriguing potential applications it promises, which include imaging capabilities similar to regular x-ray diffraction [1], yet in combination with spectroscopic sensitivity. This sensitivity is provided by the influence of the lower energy, photon field, which can be selected to be equivalent to the characteristic valence electron energies of the studies sample.
To enable these application, this nonlinear x-ray process requires a more thorough and detailed understanding.
Therefore, this thesis focuses on providing a systematical, experimental approach to measure the characteristic scattering signature for the parametric down-conversion of x-rays into optical photons. It attempts to go beyond the mere proof of principle and to measure the extended parameter space of the effect.

Fundamentally, the x-ray parametric down-conversion process is a scattering effect. Hence, the general concepts of x-ray scattering are explained in Chapter 2 together with an introduction to the specific effect of XPDC and its determining phase-matching condition.
The subsequent Chapter 3 gives a review on the theoretical understanding and previous experimental investigations of the process in the degenerate and non-degenerate regime. Within this chapter the theoretical approaches and developments to describe the effect are summarized, critically discussed and finally a novel, fully quantized ap-

proach is presented. The experimental setups and methodologies used for investigations of XPDC are presented from the early proof-of-principle experiments at tube sources towards detailed studies at synchrotron radiation sources.
Starting from the effect's theoretical proposal in 1969 both theoretical and experimental studies first examined the degenerate regime and continued investigations towards the non-degenerate regime. As such, XPDC was observed for idler energies down to the UV-range, which constitutes the starting point of this thesis. For the applications connected to idler photons in the visible regime the proof-of-principle of xpdc to VIS needed to be provided, as well a comprehensive understanding of its associated parameter space to push the effect towards application. For that purpose, an experimental setup, which is based on energy resolved diffraction, is presented in Chapter 4). Together with a detailed description of the data acquisition method, the analysis of the obtained experimental data is presented and results discussed in detail with respect to concurrent background effects in Chapter 5.
The results obtained in the scope of this thesis are set into the wider scientific context by discussing the direct implications on published results in Chapter 6.
A summary and conclusion of the presented experimental work is given Chapter 7. Finally, possible extensions and refinements of the experimental setup are presented and applications of the nonlinear effect are envisioned in the outlook Chapter 8.

Chapter 2

Fundamental Concepts

Fundamentally, the process of scattering describes the deviation of a particle's trajectory by the interaction with a local object - the scattering center. In the case of light-matter interactions, photons scatter on the atom's electronic shell or the nucleus. If a comprehensive understanding of the scattering process is available, the interaction can be used to determine the structure and composition of the sample medium.
Beyond the study of materials, the scattering process grants access to investigate the nature of the light-matter interaction itself. This work focuses on the latter case and investigates a theoretically predicted, yet (almost) unexplored, nonlinear, spontaneous interaction, which occurs during the scattering process of x-rays with structured matter. The central problem of this work is the experimental observation of the parametric conversion of x-ray photons into visible photons.
A brief review of the concepts of x-ray scattering is presented in this chapter (2.1) [2], before introducing the nonlinear effect of parametric conversion in detail (2.2). Subsequently, the kinematic solutions of the effect's characterizing phase-matching condition are presented (2.3).

2.1 The Fundamental Scattering Experiment

Conceptually, a scattering experiment is realized by an incident flux of particles (here photons) impinging on a sample system, which is initially in the ground state. The incident radiation ($\vec{k}_{in}$) interacts with the sample and is consequently scattered ($\vec{k}_{out}$), under potential variation of its direction, intensity and energy (Figure 2.1).
The incident radiation is defined by the intensity[1] I_0 with the photon energy $E_{in} = \hbar\omega_{in} = hc/\lambda_{in}$. After interaction with the sample, the rate of scattered photons Γ_{sc}, number of photons per second, is observed within a solid angle $\Delta\Omega$, at a distance R.
Microscopically, the process can be understood in the following way: In reaction to the incident light field, the electronic charges start to oscillate and act as a secondary emitters of radiation themselves. The direction and energy of the (re-)emitted photons

[1] The incident intensity is described by the magnitude and direction of a flow of particles. It is defined as number of photons per unit time and unit area multiplied by the photon energy E_in.

may differ from the incident conditions.
If such a difference occurs for the energy of the involved photons, the process is referred to as *inelastic scattering*. Whereas in the case of equal energies, the process is referred to as *elastic scattering*.

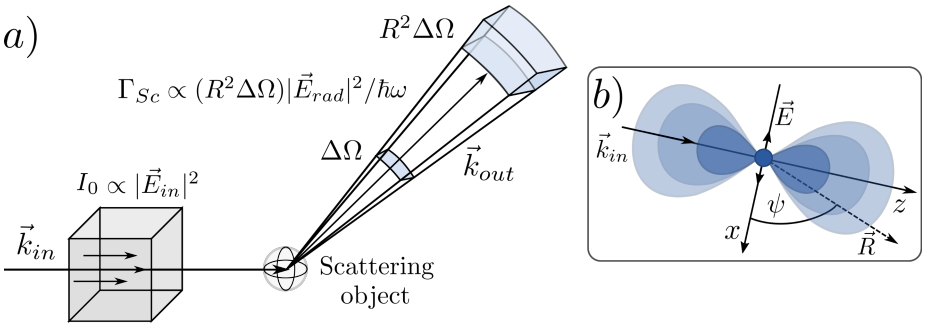

Figure 2.1: Schematics of a fundamental scattering experiment (a): The incident intensity I_0 impinges on the scattering object. The rate of scattered photons Γ_{sc} is observed in a distance R by the detector, which covers a solid angle of $\Delta\Omega$. The microscopic response of an electron in the case of Thompson scattering is depicted in (b): The electric field of an incident plane wave causes oscillations of the charge, which (re-)radiate electromagnetic waves in a dipolar pattern.

The differential cross section for a scattering process, i.e., a measure of its efficiency, can be written as the fraction of scattered (Γ_{sc}) over incident intensity (I_0) per solid angle [2]. For the fundamental process of radiation being elastically scattered by a single electron, also known as Thomson scattering, this reads

$$\left(\frac{\mathrm{d}\sigma}{\mathrm{d}\Omega}\right) = \frac{\Gamma_{sc}}{I_0/\hbar\omega \cdot \Delta\Omega} = \frac{|\vec{E}_{rad}|^2}{|\vec{E}_{in}|^2} R^2 = r_0^2 \cdot P$$

for which $r_0 = \frac{e^2}{4\pi\varepsilon_0 mc^2} = 2.82 \cdot 10^{-5}$Å is the Thomson scattering length and P the polarization factor. The latter needs to be distinguished for three different cases. On storage ring facilities x-rays are generated with a polarization which is most commonly orientated along the horizontal plane of the ring. The polarization factor depends now the geometry of the scattering experiment as

$$P = \begin{cases} 1 & \text{for the vertical scattering plane} \\ \cos^2\Psi & \text{for horizontal scattering plane} \\ \frac{1}{2}\left(1+\cos^2\Psi\right) & \text{for an unpolarized source} \end{cases}$$

where the angle Ψ is determined relative to the polarization axis (x), orientated orthogonal to the propagation direction z (Figure 2.1 b).

Scattering from perfect crystals

X-ray scattering has become a versatile method to study matter in various forms and is frequently applied to investigate gaseous, liquid, solid and plasma-like sample materials.
For elastic scattering from flat perfect crystals a brief introduction is presented in the following.
Perfect crystals are defined as crystalline materials without point, linear or planar defects, nor impurities or crystallographic imperfections. They are characterized by their atoms (or ions) periodic positions in space, i.e., by the lattice constants. For an arbitrary crystal, the lattice vector $\vec{R}_n$ is defined by a set of basis vectors describing the lattice in real space (Figure 2.2 a)

$$\vec{R}_n = n_1\,\vec{a}_1 + n_2\,\vec{a}_2 + n_3\,\vec{a}_3.$$

where n_1, n_2 and n_3 are integers. The real space basis vectors $\vec{a}_i$ can be transferred into reciprocal space coordinates $\vec{a}_i^*$ via

$$\vec{a}_1^* = 2\pi\frac{\vec{a}_2\times\vec{a}_3}{\vec{a}_1\cdot(\vec{a}_2\times\vec{a}_3)},\quad \vec{a}_2^* = 2\pi\frac{\vec{a}_3\times\vec{a}_1}{\vec{a}_2\cdot(\vec{a}_3\times\vec{a}_1)},\quad \vec{a}_3^* = 2\pi\frac{\vec{a}_1\times\vec{a}_2}{\vec{a}_3\cdot(\vec{a}_1\times\vec{a}_2)}. \tag{2.1}$$

and the reciprocal lattice vector $\vec{G}_{\mathrm{hkl}}$ is thereby defined as

$$\vec{G}_{\mathrm{hkl}} = h\,\vec{a}_1^* + k\,\vec{a}_2^* + l\,\vec{a}_3^*.$$

For cubic crystal structures specifically, as is the case for diamond and silicon (which are face-centered cubic crystals), a single lattice constant defines the structure. The integer variables h, k and l are called Miller indices. For each reciprocal lattice vector, a set of atomic planes exist, which are orthogonal to $\vec{G}$ and referred to as (hkl).
Since the periodicity of the crystal is in the same order of magnitude as the illuminating x-ray wavelength (Å-regime) constructive interferences (*Bragg reflection*) can be observed for specific scattering geometries among various other diffraction phenomena. These interferences lead to strong scattering intensities, despite the relatively low (Thomson scattering) cross sections for the interaction of x-rays with matter.
An approach to geometrically determine the condition for these constructive interferences to occur was presented by Ewald [3]. The Ewald's sphere is constructed from the origin of the real space coordinate system (O) with the radius of $|\vec{k}| = 1/\lambda$. The intersection of the sphere with the reciprocal lattice points (grey, Figure 2.2 b) yields the origin of the reciprocal space (O'). Rotation of the crystal around these origin might cause an overlay of the sphere with additional reciprocal lattice points. In the case of two points on the sphere, the wave vectors fulfill the relation

$$\vec{k}_{in} + \vec{G} = \vec{k}_{out}, \tag{2.2}$$

known as the Laue condition, for which a constructive interference is observed (Figure 2.2 b).
An equivalent formulation of this relation is given by Bragg's law

$$n\lambda = 2d_{hkl}\sin\theta \tag{2.3}$$

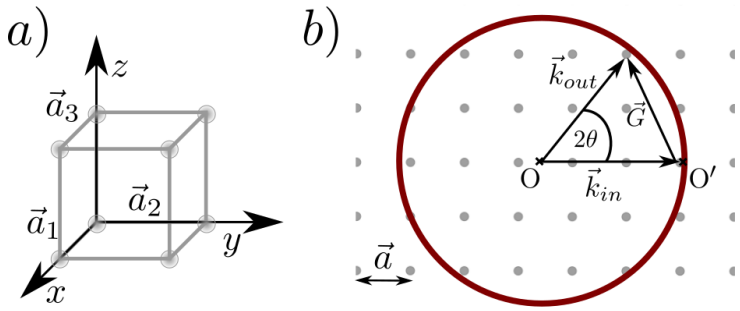

Figure 2.2: The scattering from a perfect crystal is determined by the crystal structure (a) here shown in real space coordinates $\vec{a}_i$ with $i = 1,2,3$. The direction of possible interferences can be constructed via the Ewald sphere (b), which is constructed in reciprocal space.

which describes the constructive interference on the basis of the path difference, resulting from reflections off the various lattice planes, that belong to the same Miller indices (hkl). The angle θ describes the incident, as well as the scattering angle (2θ), relative to the lattice plane defined by the Miller index and is commonly denoted as the *Bragg angle* θ_B. The variable d_{hkl} refers to the real space lattice constant of the selected plane. It can be shown [2, Chapter 5.1.5] that Bragg and Laue condition can be transformed into one another.
The scattering plane is determined by the samples orientation towards the incident beam and the plane is spanned by the surface normal and the wave vector of the incident photons.
For the case that the incident and scattered beam are on the same side of the crystal and scattering planes are parallel to the crystal's surface, is commonly referred to as *symmetric Bragg* scattering. For scattered beams leaving the crystal not at the incident surface and lattice planes being orientated perpendicular to the surface, the process is referred to as *symmetric Laue*. All other cases are referred to as *asymmetric scattering* [4].

In general, since the x-rays scatter on the electronic charges, elastic scattering provides a probe of the electron density - or more specifically a probe of the Fourier components[2] of the density. The resolution of this method is determined by the wavelength of the incident radiation and in the case of hard x-rays ($\hbar\omega > 5$ keV) corresponds to atomic scale resolution.

2.2 Introduction to X-ray Parametric Down-Conversion

The parametric conversion of x-ras can conceptually be described as a nonlinear scattering process: an incident photon - conventionally referred to as *pump* photon - st sn

[2] defined as $F(\vec{G}) = \int \mathrm{d}^3\vec{r}\,\rho(\vec{r})\,e^{\pm i\vec{G}\cdot\vec{r}}$

energy $E_p = \hbar\omega_p$ is scattered and thereby converted into a correlated pair of photons. These converted photons labeled as the *signal* ($\hbar\omega_s$) and the *idler* photon ($\hbar\omega_i$), respectively, and share the energy of the pump $\hbar\omega_p = \hbar\omega_s + \hbar\omega_i$ (Figure 2.3). For the degenerate regime of the effect, the energy ratio of the generated photon pair ω_s/ω_i is equal to unity. Beyond this, the effect can be observed for various energy splitting ratios, i.e., $\omega_i/\omega_s < 1$, which are collectively referred to as the non-degenerate case.

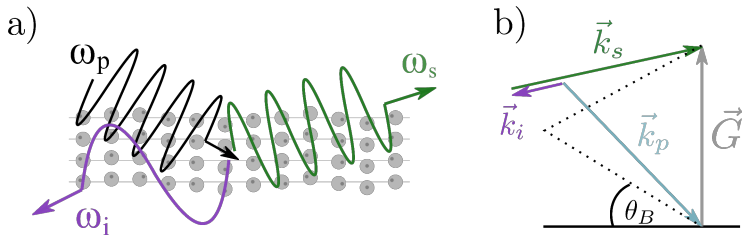

Figure 2.3: Principle of parametric conversion: (a) an incident photon of frequency ω_p is converted into a correlated photon pair: the signal (ω_s) and the idler (ω_i) photon. For down-conversion of x-rays into optical photons, the wave-vector geometry (b) resembles elastic x-ray diffraction (dotted line) and is predominantly determined by the reciprocal lattice vector $\vec{G}$. The solid line at the bottom indicates the sample's surface.

The effect of parametric conversion has its equivalent in the optical regime, where it is best known as a source for entangled photons [5–7]. The transfer to the x-ray regime was theoretically first proposed by Freund and Levine [8] in 1969. Since then various experimental and theoretical studies have extended nonlinear optics into the high photon-energy regime of x-rays. A review of these previous works is given in chapter 3.

2.3 Phase-matching Condition

Fundamentally, energy and momentum need to be conserved as an essential criterion to observe the parametric process of down-conversion. Even though a comprehensive theory needs to consider the microscopic interaction (as it is done by the quantum electrodynamic approach presented in chapter 3.3), the behavior of scattering angles can be obtained by fundamentally considering the kinematic relations, i.e., momentum and energy conservation

$$\omega_p = \omega_s + \omega_i \tag{2.4}$$

$$\vec{k}_p + \vec{G} = \vec{k}_s + \vec{k}_i \tag{2.5}$$

These relations combined constitute the kinematic phase-matching condition, which needs to be fulfilled to allow for the nonlinear scattering. From equation 2.5 it becomes apparent, that the reciprocal lattice vector $\vec{G}$ governs the process.
For the highly non-degenerate case of XPDC, in which x-ray photons are converted into a pair of x-ray and optical photon for which the energy difference spans over four

orders of magnitude the difference in scattering angle between linear and nonlinear scattered photons is small (Figure 2.4). For regular elastic scattering (Figure 2.4 a), the pump beam with wave vector $\vec{k}_p$ is scattered by the reciprocal lattice vector $\vec{G}$ at twice its corresponding Bragg angle θ_B. This yields the scattered wave vector $\vec{k}_B$.
Concurrent to the linear scattering process, the nonlinear effect of XPDC occurs for the same incident angle of the pump field. The pump photon is split into the signal ($\vec{k}_s$) and idler ($\vec{k}_i$) photon pair (Figure 2.4 b). Notably, the sum of $|\vec{k}_s|$ and $|\vec{k}_i|$ is slightly larger than $|\vec{k}_p|$ due to the influence of the sample's refractive index n on $\vec{k}_i$ at optical wavelengths.
In contrast to Bragg reflection, which occurs in a narrow angular range given by the Darwin width[3], the phase-matching condition of XPDC allows for (theoretically) a broader angular spread of the effect.
When rotating the sample crystal and thus the reciprocal lattice vector $\vec{G}$ by $\Delta\Omega$, another phase-matching condition can be fulfilled (Figure 2.4 c).

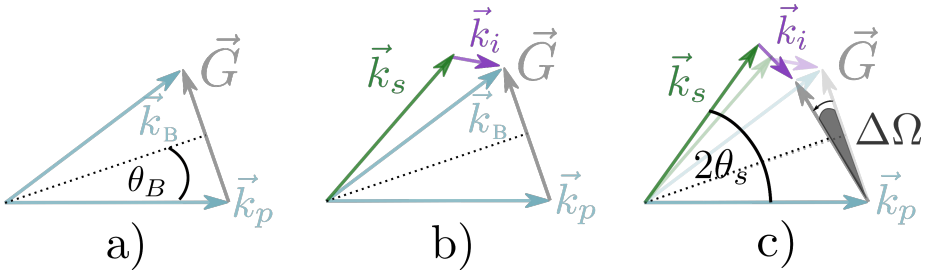

Figure 2.4: Schematics for elastic and PDC scattering: a) scattering for Bragg condition, b) PDC fulfilling energy and momentum conservation at the same Bragg condition and c) phase-matching condition for different sample angle Ω. Wave vectors $\vec{k}_p$, $\vec{k}_s$ and $\vec{k}_i$ refer to pump, signal and idler, respectively. The reciprocal lattice vector is given by $\vec{G}$ and the sample rotation by $\Delta\Omega$.

On the basis of these considerations, scattering angles for a fixed energy conversion ratio ω_i/ω_s can be calculated via vector algebra in the following manner (Figure 2.5): The selected lattice plane (hkl), on which the diffraction process takes place, is defined by the reciprocal lattice vector $\vec{G}$. The incident angle Ω is defined with respect to this lattice plane. The direction (incident angle Ω) and length of the incident wave vector $|\vec{k}_p| = 2\pi/\lambda_p$, with $\lambda_p = hc/E_p$, defines the point r_A. Due to the selected conversion ratio, the lengths of the signal and idler wave vectors $|\vec{k}_s|$ and $|\vec{k}_i|$ are known. The directions of signal and idler photons are constructed by the intersection of the two circles with radii $|\vec{k}_s|$ and $|\vec{k}_i|$ (Figure 2.5). The center of the idler circle, r_B, is located at the end of the reciprocal lattice vector.
Three scenarios can be differentiated: 1.The two circles do not intersect, i.e., for the given incident angle the phase-matching condition cannot be fulfilled. 2. The circles intersect in one point, yielding a single solution for the expected scattering angles of

[3]The Darwin width w_h^θ is the full width at half-maximum (FWHM) of the total reflective curve of a crystal. It is calculated on the basis of dynamical diffraction theory.

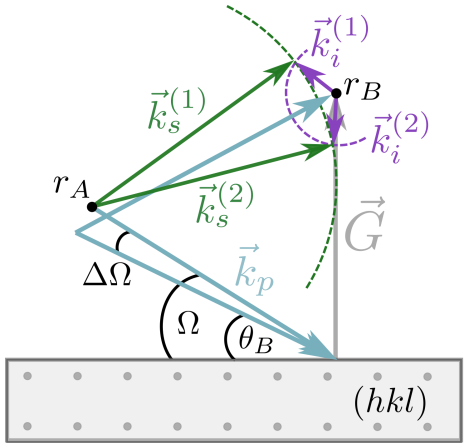

Figure 2.5: Schematic construction of scattering angles on the basis of vector algebra. The photon $\vec{k}_p$ incides on the lattice planes (hkl) under an angle of Ω. The lattice vector $\vec{G}$ is orientated normal to the lattice planes (here for a symmetric reflection). The directions of the nonlinearly scattered signal and idler photons, i.e. $\vec{k}_s$ and $\vec{k}_i$, are constructed by the intersection of two circles around the points r_A and r_B with radii $|\vec{k}_s|$ and $|\vec{k}_i|$.

idler and signal photon. 3. Phase-matching can be achieved such, that two angles fulfill energy and momentum conservation (Figure 2.5).
The scattering angle for $\vec{k}_s$ can be measured in different reference systems, for example with respect to elastic scattering, as is mostly done within this work, or relative to the sample surface.
As an example, the scattering angles of the signal photon are calculated for a diamond sample in 220 orientation (Figure 2.6). The photons are generated from a pump photon of $E_p = 10$ keV for a non-degenerate conversion, yielding $\hbar\omega_i = 2$ eV and $\hbar\omega_s = E_p - 2$ eV, respectively.
Most notable is the broad angular acceptance for the incident angle Ω, which is provided by the phase-matching condition - spanning 60 mdeg for the specific case presented. A similar large angular range is covered by the corresponding scattering angles $2\theta_s - 2\theta_B$. The angle θ_B refers to the Bragg angle for photons of the fundamental energy $E_p = 10$ keV.
The kinematic considerations of the phase-matching condition can be used to predict characteristic scattering signatures for the nonlinear process of x-ray parametric down-conversion (Figure 2.6). Experimental investigations should aim to detect these characteristic signatures in order to correctly identify the nonlinear process. As such the evaluation of scattering data in this work is (later) performed on the basis of the here presented approach.

Notably, the actual scattering signal is expected to shows intensity modulations on top of these signatures due to effects beyond the purely kinematic considerations.

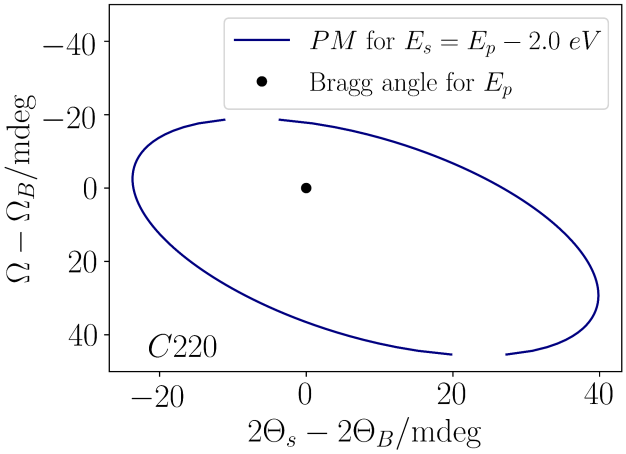

Figure 2.6: Exemplary calculation via phase-matching (PM) of the scattering angles of the signal photon for parametric down-conversion of $E_p = 10$ keV incident photons in diamond (220). The conversion ratio is fixed by the pump energy together with a selected idler energy $\hbar\omega_i = 2$ eV. The sample rotation angle is given relative to the Bragg angle of 10 keV by $\Omega - \Omega_B$ and the scattering angles are given by $2\theta_s - 2\theta_B$ relative to the expected elastic signal. The position of the Bragg scattered photon is indicated by the black dot.

A comprehensive theoretical description should account for these modulations of the scattering pattern and establish a connection to the microscopic properties of the probed sample.

Chapter 3

Review of preceding studies and novel approaches

This chapter gives an overview of the established understanding of the XPDC process, for the degenerate and the non-degenerate regime. It reviews theoretical and experimental investigations of the effect, from its first theoretical proposal by Freund and Levine in 1969, to current theoretical developments to understand the nonlinear interaction within the highly non-degenerate regime. The chapter furthermore reviews experimental works, beginning with proof of principle studies conducted by Eisenberger and McCall in 1970, shortly after the theoretical proposal. The chapter continues with presenting the transfer of experiments from laboratory x-ray sources to synchrotron sources and then reviews experiments aiming towards observing higher non-degeneracy, i.e., smaller idler energies. These experimental proceedings are presented in order to set the scientific context for the here presented work. Furthermore, the XPDC process is compared to similar nonlinear wave mixing phenomena and consecutive studies with respect to specific parameters or first applications are presented.

3.1 Parametric x-ray conversion in the degenerate regime

Early theoretical models are based on classical and semi-classical approaches to explain the nonlinear phenomenon and mainly originate from formulations of parametric conversion within the optical domain. These concepts are transferred to the x-ray regime, where they are applicable under specific conditions.

3.1.1 Early theoretical works

The very first work to be mentioned in the context of the parametric conversion of x-rays is the effects' theoretical proposal by Freund and Levine in 1969 [8], which was followed by a publication *Parametric down-conversion of x-rays* [9] in 1970, discussing potential experimental parameters in greater detail.
The conversion process in a semi-classical, non-relativistic framework, which excludes

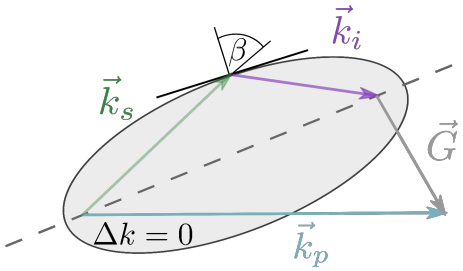

Figure 3.1: Phase matching surface adapted from [8]: Possible combinations of signal ($\vec{k}_s$) and idler ($\vec{k}_i$) wave vectors are predicted to lie on a nearly ellipsoidal surface.

resonances and associated phase shifts. Moreover, their description is limited to incident x-ray frequencies above the K-absorption edge of the nonlinear medium. Microscopically, the effect is explained via the nonlinear polarization of the medium, that is induced by the incident x-ray field. Freund and Levine obtain this polarization from an earlier result by Armstrong et al. [10], who calculated the coherent, nonlinear response of an atom to applied electromagnetic fields [9]. The polarization includes contributions at the signal and idler frequencies, for which spontaneous parametric decay is explained by quantum fluctuations of the vacuum field and their beating with the incident x-ray photon field. The emission of signal and idler fields are maximized, when all unit cells within the sample crystal radiate in phase, that is when momentum is conserved, namely by $\vec{k}_p = \vec{k}_s + \vec{k}_i + \vec{G}$. This was originally derived for a one electron atom and is extended to a many electron atom by using (tabulated) structure factors by means of time-dependent perturbation theory.
Referencing an earlier work by Kleinman [11], the authors present a generalized ansatz for the construction of a so-called *phase-matching surface* being of ellipsoidal shape (Figure 3.1) and describing possible combinations of the energy distribution among the down-converted photon pair. An enhancement of converted intensity is predicted when $\vec{k}_s$ and $\vec{k}_i$ are nearly parallel. The same was previously found within the framework of Kleinman [11] for the optical regime, for which he introduced the terminology of *edge enhancement*.
Since the effect is intrinsically very weak, - while no specific conversion rates are mentioned[1] - competing background processes are discussed. Background contributions are expected in the form of fluorescence, Compton scattering[2] and thermal diffuse scattering [13]. As discrimination technique against these competing effects a combination of energy discrimination and coincidence detection is proposed. Especially for the degenerate regime, in which the signal and idler are of equal energy and half the incident's energy, discrimination by energy is experimentally easily achievable. In addition, both photons (signal and idler) are proposed to be detected in coincidence.
In a consecutive study [9], Freund and Levine apply their approach to calculate the

[1] except for a prediction of expected count rates - approximately one per second - under consideration of available x-ray laboratory sources and sufficient background suppression.

[2] The Compton effect [12] describes an inelastic scattering process, in which a photon is scattered on an electric charge. During the interaction energy from the photon is transferred to the charge.

expected signal-to-noise ratios of the XPDC detection rates, which they find to be proportional to the squared value of the macroscopic nonlinear susceptibility[3].
Another extension is performed by including thermal effects on the predicted detection rate, via the Debye-Waller factor[4].
In addition, several different sample materials are theoretically investigated for the down-conversion process in the x-ray regime. Simple elemental crystals with few atoms per unit cell are discussed as possible sample materials, covering diamond, Si, Mo, Sb and Cu, Ge, Nb, Au, Pb. Within their established theoretical framework, a single criterion for an optimal sample material is not found. The authors suggest - with regard to their calculations - that parametric conversion can be observed throughout the periodic table for crystalline materials.

3.1.2 First experimental investigations in the degenerate regime

Eisenberger and McCall [16] follow the original proposal by Freund and Levine towards first observation of degenerate parametric conversion in the x-ray regime in 1971 and present first experimental evidence. The experiment is performed with a 2 kW x-ray tube, using molybdenum K_α-radiation at 17 keV, yielding a flux of 10^7 ph/s and a divergence of ~ 1.7 mdeg and 8.7 mdeg (horizontal and vertical). The nonlinear material is a beryllium crystal in $11\bar{2}0$ orientation. The incident photon energy is converted into a pair of photons at 8.5 keV each, which is detected in coincidence (Figure 3.2).

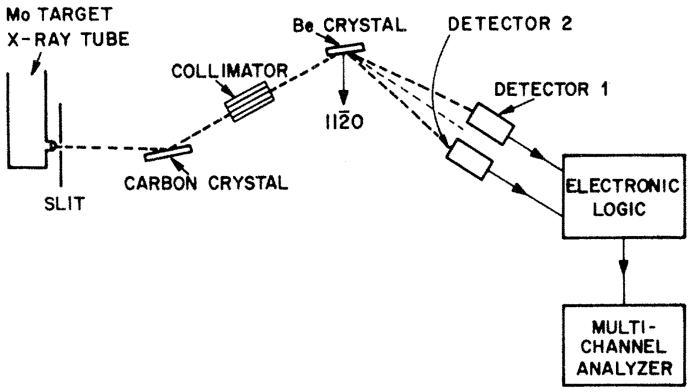

Figure 3.2: Schematics of the experimental setup to observe parametric down-conversion of x-rays in the degenerate regime driven by an x-ray tube [16]. The collimated beam impinges on the beryllium sample crystal and the down-converted photon pair is detected by detector 1 and 2 in coincidence (electronic logic).

Conceptually, the authors describe the nonlinear process as an absorption of a pump

[3] In general a susceptibility is defined as the quantification of a property's modification being introduced by the presence of external fields. The nonlinear susceptibility thereby describes a nonlinear behavior of the imposed property change.

[4] The Debye-Waller factor [14, 15] describes the influence of microscopic thermal motion, i.e., lattice vibrations, on x-ray or neutron scattering. It is also referred to as B-factor or temperature factor.

photon $\hbar\omega_p$ and a consecutive emission of two photons at $\hbar\omega_s$ and $\hbar\omega_i$, fulfilling energy conservation. Scattering directions and intensities for the parametric down-conversion process are calculated by considering sum frequency generation (SFG). Within this process two incident photons ω_s and ω_i are mixed inside a nonlinear medium, yielding an outgoing photon ω_p, which is considered the equivalent - yet time-reversed - process. This approach is justified by the authors, since the processes of frequency mixing and splitting would be determined by the same transition matrix element.
Their theoretical description, is based on a classical model of free electrons, and in contrast to optical phenomena, the nonlinearity is found not to be dependent on broken inversion symmetry and resonances[5].
Beryllium is chosen as a nonlinear material, because of its low x-ray absorption properties and good crystalline quality. The background Compton rate of $2.5 \cdot 10^3$ s^{-1} was effectively suppressed by energy discrimination of the detector (98% suppression of 17 keV) and by coincidence detection to less than $3 \cdot 10^{-4}$ s^{-1}, within the coincidence time window of 52 ns. The detected signal rate yielded $2.7 \cdot 10^{-4}$ s^{-1}. The sample angle was scanned within 50 runs with 8 h acquisition time each, yielding a final signal coincidence rate of 1 h^{-1}. Even with a reported systematic experimental error of 40 %, quantitative agreement with theoretically predicted rates is observed. Considering the given initial flux and measured signal counts, a conversion efficiency (within experimental uncertainties) of $\sim 10^{-11}$ is experimentally determined.

3.1.3 Experimental continuation at synchrotron sources

A subsequent experimental study on parametric down-conversion in the degenerate regime is presented 27 years later by Yoda et al. [18], which is performed at a synchrotron light source. The experiments are conducted at the Photon Factory (KEK) at a wiggler beamline with 10^9 incident pump photons per second at an energy of 19 keV (0.65 Å). The beamline offers an essential improvement in terms of flux, monochromatization (via a Si 111 double-crystal monochromator) and divergence (0.2×0.1 mrad (vertical and horzizontal), compared to experiments on x-ray tubes. On the detection side, avalanche photodiodes are used for detection of the signal photons, instead of the slower scintillation detectors in earlier studies.
The measurements were performed on a diamond crystal as the nonlinear medium in 111 and 400 orientation. The better crystal quality in the case of diamond is an improvement over previous experiments, in which beryllium crystals were used, and was already proposed by Levine and Freund [8]. Apart from that the experimental setup is similar to the one presented by Eisenberger and McCall [16] (Figure 3.2) and experimental proof is achieved via energy discrimination in combination with coincidence detection. The coincidence time window is set to 1.5 ns, yielding count rates of 120 cnts/h for the 400 reflection and 44 cnts/h for the 111 orientation. Normalizing by the incident flux, this study yields an approximate conversion efficiency of $\sim 10^{-11}$, which is in line with predictions from previous works by Freund [9] and Eisenberger and Mc-

[5]The statement of the independence from broken inversion symmetry remains valid, also under consideration of new theoretical descriptions introduced in Section 3.3. The requirement for inversion asymmetry originates from the applied dipole approximation in the all-optical case. This approximation is not valid in the x-ray regime anymore.

Call [16].

In 2000, Adams et al. [19, 20] present two studies for degenerate conversion processes in diamond conducted at synchrotron sources. The studies make use of higher initial flux and technical improvements and can thereby report higher detection rates. Time-correlation measurements and energy discrimination are used in combination with silicon drift chambers as detectors to measure the effect. These detectors offer an energy resolution of ~ 300 eV and a temporal resolution of ~ 100 ns.
Even though an experimental work is presented, the authors also include a theoretical approach analogous to [16] to estimate the expected signal count rate. The study presents experimental data which agrees well with the predicted emission angles.
Finally, the obtained results are compared to previous studies by Yoda et al. [18]. The experiments by Adams et al. yield 2.5 times as many events, while an increased flux by a factor of 6 is available. Despite this deviation, the conversion rate is found within the same order of magnitude as reported by Eisenberger [16] and Yoda [18].

Within the scope of parametric down-conversion in the degenerate regime, the effect of second harmonic generation (SHG) should be briefly discussed, since it presents the temporally reverse phenomenon. For SHG, two photons of equal energy are mixed, producing a third photon of summed energy (Figure 3.3). Experimental evidence on

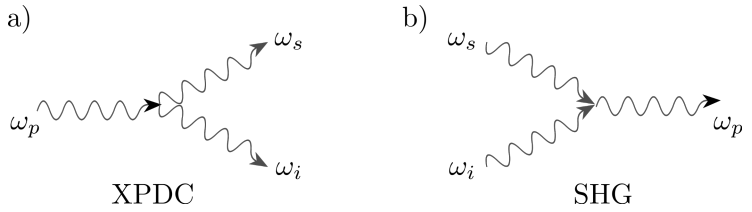

Figure 3.3: Schematic depiction of the frequency conversion processes: second harmonic generation (SGH) and parametric down-conversion (PDC). In the SHG process two photons of the same energy are combined into a final photon, whereas in PDC, one photon is converted into a photon pair. In the degenerate regime of PDC the converted photons likewise have the same energy.

the fundamental process of x-ray second harmonic generation was presented by in 2014 [21] and was again investigated at free electron lasers [22]. In the experiment the expected quadratic scaling of the SHG signal with pump intensity was observed. Despite being similar to the XPDC process by being spontaneous in nature, SHG benefits from high peak intensities. This is due to the fact that two photons of the same mode and wavelengths need to be present in the interaction volume, whereas for XPDC one photons is sufficient.
The theoretical descriptions of x-ray SHG [21, 23] are based on the model of free electrons, which is reasonable for incident photon energies far exceeding the binding energies of the material.
The experiment is performed on single crystal diamond with a focused, monochromatic pump beam of $E_p = 7.3$ keV and average incident intensity of $I_0 \cong 10^{16}$ W/cm^2.

The beam is monochromatized by a Si 111 double crystal with approximately 1 eV bandwidth, which suppresses the second harmonic of the undulator by four orders of magnitude. The second harmonic wavelength is observed in a small angular range of 0.2 mdeg (sample rotation), where the emission angle is determined by the phase matching condition ($2\vec{k}_\omega + \vec{G} = \vec{k}_{2\omega}$).
Phase matching for the 220 reflection of diamond is chosen, since the condition is fulfilled for the photons at second harmonic, but scattering at the fundamental energy that would result in the same scattering angle (110 reflection) is forbidden (highly suppressed). An aluminum filter in front of the detector further reduces background contributions from scattering of the remaining fundamental radiation. A YAP:Ce scintillator is used for energy sensitive detection.
The interpretation of the signal as SHG is supported by a measurement of the signal intensity in dependence of the incident intensity, which is found to be quadratic, as predicted for the SHG process. In addition, the dependence of the sample angle is measured, which yields a maximum signal when phase-matching is fulfilled.
The efficiency for x-ray SFG is determined to $(5.8 \pm 1.1) \cdot 10^{-11}$ and agrees well with the predicted value of $5 \cdot 10^{-11}$ within the frame of the presented model. This efficiency is in the same order of magnitude as results obtained for the parametric down-conversion in the degenerate regime.

3.2 Parametric x-ray conversion in the non-degenerate regime

In consecutive studies, the effect of parametric conversion in the x-ray regime was investigated with respect to an asymmetric distribution of energy among the down-converted photon pair. This regime is referred to as non-degenerate XPDC and requires alterations of the established theoretical models and experimental investigations.

3.2.1 Extensions and modifications of theoretical understanding

Already in 1971, Eisenberger and McCall proceed their first experimental investigations with theoretical considerations towards non-degenerate XPDC [17]. They use a semi-classical approach, referencing works of Armstrong [10] and Franken [24], who discussed frequency mixing processes in the all optical case and for intense photon fields.
Conceptually, they extend a formalism for sum and difference frequency generation (SFG and DFG) to describe the temporally reverse process of PDC, similar to earlier descriptions from Freund [25]. In this picture, the low energetic idler photon interacts with the material and introduces a modulation of the electronic charge density within the crystal. When the higher energetic signal photon is scattered on the modulated electronic charge, it is subject to a Doppler shift [26]. Depending on the direction of the charge modulation the resulting photon obtains a positive (negative) frequency shift, which results in sum (difference) frequency conversion. The scattering direction is still determined by energy and momentum conservation.

The formalism uses a semi-classical approach, under consideration of a limited number of transition matrix elements. However, more elements need to be considered for a full investigation. In addition, for high x-ray energies, relativistic effects need to be included in the framework.

At the same time, in 1972, Freund extends the earlier presented approaches [8,9] for degenerate PDC towards non-degeneracy [27]. Similar to Eisenberger and McCall [17], the extension is based on considerations for the optical regime by Armstrong [10], which Freund extended towards the x-ray regime.
Moreover, first applications of non-degenerate XPDC are proposed, which aim to measure the charge distribution of valence electrons in covalently bound crystals[6] and by that gain a deeper understanding of chemical bonds. Such measurements are enabled by the ability to tune the energy distribution among the down-converted photon pair. By variation of this energy splitting ratio, different physical properties, which are sensitive to different frequency regimes could be probed by a corresponding choice of the idler frequency. The optical susceptibility of a selected idler frequency is determined to be directly proportional to the measured intensity for a selected down-converted photon pair.
The theoretical model for explaining the non-degenerate regime of XPDC again invokes the notion of partially free electrons, which stands in contrast to the real conditions of bound electrons in crystalline materials. The presented considerations are limited by Freund to insulators and semi-conductors, which exhibit the separation of valence and conduction bands. Here, he partially implements the behavior of electronic charges, namely electronic transitions of valence electrons are allowed, yet solely at the band gap energy. The electronic structure apart from these transitions is neglected, even though the whole electronic structure is supposed to be probed by the effect, posing a contradiction within itself. Under these considerations, an expression for the structure factor of valence electrons is derived, which allows - in principle - a direct determination of the valence charge distribution. The down-converted intensity therefore needs to be measured at different crystal orientations and the valence charge distribution is reconstructed by Fourier synthesis [28].

3.2.2 Experimental investigations of non-degenerate XPDC

A decade later (1981), experimental studies continued with a focus on the non-degenerate regime of parametric conversion processes. Danino et al. [29] present the first experimental study within this context, specifically for XPDC into extreme ultra-violet[7] photons.
An x-ray tube generating 8 keV (Cu-K_α) radiation is used for the conversion into a pair of 7.7 keV signal and 0.3 keV idler photons[8] (Figure 3.4 b) in a lithium fluoride (LiF) single crystal. By entering the regime of non-degeneracy, the experimental ap-

[6] Covalent crystals, also referred to as *covalent networks*, consist of a lattice, in which the bonds are established by shared valence charges. These crystals are composed by atoms and are insulators or semiconductors.

[7] Extreme ultra-violet or EUV radiation is defined as the wavelength range of $(10 - 120)$ nm [30].

[8] with an attenuation length [31] of 0.5 µm)

proach is altered. Since the low energetic idler photons are directly absorbed after their generation, a coincidence detection is no longer possible. Therefore, experimental approaches rely solely on measuring the emitted signal photon and energy discrimination from the fundamental radiation becomes crucial. For the energy discrimination implemented for studies in the degenerate regime, the incident and signal photon energies differed by a factor of two. Now, signal energies deviate only by a fraction from the incident fundamental energy, thereby demanding a more accurate energy identification and discrimination from the fundamental pump energy.
For the experiment a germanium 111 3-bounce channel-cut monochromator is used in front of the sample to select a narrow bandwidth of the pump energy from the tube's emitted spectrum (Figure 3.4 b). Since the conversion efficiency of XPDC in the non-degenerate regime is estimated to approximately 10^{-10}, concurrent scattering processes yielding similar signal energies need to be suppressed to below these rates.
The phase-matching condition is tuned to the previously proposed edge enhancement, i.e., when signal and idler wave vector are anti-parallel (Figure 3.4 a) and generate down-converted signal photons within a relatively small energetic width (being most suitable for the chosen experiential setup). For the 200 orientation, the LiF sample

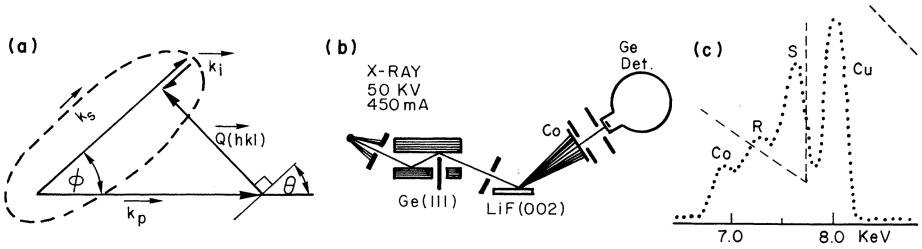

Figure 3.4: Schematics of phase-matching geometry (a) and the experimental setup to observe parametric down-conversion of x-rays in the non-degenerate regime (b). Measured spectrum (c) include various features. Figure taken from [29].

is detuned by $\Delta\theta_B = 6.7$ deg from Bragg condition ($\theta_B^{LiF} = 22.489$ deg [32]) and the detector is set to an angle of $\phi = 46.8$ deg. For the measurements, two of the three parameters ϕ, $\Delta\theta_B$ and $\hbar\omega_s$ are fixed in turn, whereas the third one is scanned (Figure 3.4 a).
An energy resolving detector with 150 eV resolution is used to distinguish scattering contributions of nonlinear scattered photons (S) from background within the acquired spectrum (Figure 3.4 c). As background, the authors identify Compton (C) and thermal scattering (Cu), the 690 eV fluorine Raman line (R) and the fluorescence of a Cobalt filter (Co) in front of the detector. The filter is used to suppress Compton and thermally scattered photons. The study is focused on the determination of the correct scattering angles as evidence for the phase-matching process, which is achieved and agrees well with predicted scattering angles. Flux considerations, however, are neglected and therefore no comparison to previous efficiencies is possible.

The experimental investigations in the non-degenerate regime are continued by Tamasaku

et al. in a series of studies [33–35] starting in 2007. They consequently lead towards the first application of non-degenerate XPDC [36] a few years later.
Investigations were resumed for idler wavelengths in the ultra-violet regime and conducted exclusively on synchrotron radiation sources. The experiments were performed at the SPring-8 synchrotron, providing $9.3 \cdot 10^{11}$ photons/s at an incident photon energy of $E_p = 11$ keV. The undulator's full beam with its 3% energetic bandwidth was used without collimation or focusing optics.
For down-conversion into UV-photons, the experimental difficulties are emphasized. The nonlinear susceptibility for parametric conversion in the x-ray regime is stated to be ten orders of magnitude smaller than for optical wavelengths. In addition, the low idler energy imposes higher requirements on energy differentiation of the signal photon and higher angular resolution of the scattering angles, since the difference between scattering angles of linear and nonlinear scattered photons is small.
These demands were met by using the high intensity available at synchrotrons and a bent Ge 220 analyzer with a resolution of 2.2 eV to energetically analyze the scattered radiation. A NaI scintillation-counter is used for detection, which covered a solid angle of $\Delta\Omega_s = 1.4 \cdot 10^{-5}$ sr.
Down-conversion is performed in a single crystal diamond (synthetic, type II, 111 surface, with a thickness of 2.56 mm) and the measured Rocking curve, i.e., rotation of the sample at fixed analyzer and detector position, agrees well with predictions [37] for the chosen 111 orientation. Phase-matching is again achieved for a configuration, in which signal and idler are aligned anti-parallel. In this geometry (edge-enhancement), the signal wave is emitted into a relatively large solid angle, while having a narrow spectrum. These conditions originate from the phase-matching condition under bandwidth and divergence considerations. This geometry is an advantageous choice, since the the Ge analyzer selects a narrow bandwidth and the detector enables covering a large solid angle.
In contrast to earlier reports [29], an extraordinary behavior for the signal peak was observed. For a selected idler energy of $E_i = 100$ eV, the Rocking curve scan yields a pronounced feature on top of the Compton background (Figure 3.5). Instead of the expected Lorentz-shaped intensity distribution (red dashed line) for a scan of the sample angle, a peak with a successive dip was reported. The peak was interpreted as the down-converted signal photons, whereas the dip is explained by a Fano interference[9] of nonlinear scattered and Compton scattered photons. Notably, the signal feature extends over a broad angular range of 0.6 deg for sample angle $\Delta\theta$, while theoretical predictions with 8.59 µdeg (0.15 µrad) are by orders of magnitude smaller. This discrepancy is explained by the strong absorption of the idler photon at $E_i = 100$ eV, which relaxes the phase-matching condition to a theoretical value of 0.017 deg, still resulting in a remaining deviation by a factor of 30 from predicted values.
The measured signal intensity was reported to 61 photons/s, being a factor of 3 smaller than theoretical predictions, which are based on a classical description governed by the influence of the nonlinear susceptibility.

[9] The Fano effect [38] describes the interference of a quantum mechanical discrete emission with continuum radiation. The characteristic Fano line shape describes an asymmetric spectrum.

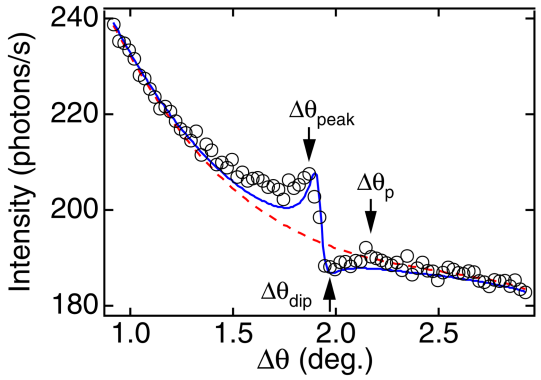

Figure 3.5: Rocking curve scan for phase-matching at $\Delta E = 100$ eV. Compton scattering is dominating background contribution (red dashed line). Figure taken from [33].

Due to the not fully understood behavior of the obtained signal, experimental investigations were continued and extended. In a consecutive study [34] the idler energy dependence in the EUV-regime was examined. Sample angle scans, as in the foregoing report, were performed for idler energies from 130 down to 50 eV. The experimental approach and setup remained the same. The phase-matching condition was measured via Rocking curve scans of the sample, for which the angular range extended over ± 1 deg around the respective Bragg angle. The signal line shape of the Rocking curves (Figure 3.6) is found to change from Lorentzian shaped, for high idler energies, to a Fano line shape for lower idler energies. The observed fpeak decreased in pronunciation with decreasing idler energy and the dip became more pronounced for lower idler energies. The total signal decreased continuously for lower idler energies and no nonlinear signal was identified below $E_i = 50$ eV.
A interference of inelastically Compton scattered and nonlinearly converted photons (Figure 3.7) is again proposed as the origin of the observed line shape. As a caveat at this point it should be mentioned, that a Fano interference can only occur, when both final states of the concurrent processes are equal. In the case of Compton scattering and XPDC this might not be the case as the authors point out, since in the first case energy is absorbed by the system and in the latter the final state resembles the initial state. The authors, however, neglect this fact and postulate an interference nevertheless.
In a subsequent experimental study [35] the Fano effect is presented as a quantum mechanical mechanism to describe the interference of competing interaction pathways towards a final state (Figure 3.7 c).

Within this study, the non-degenerate conversion of x-rays is investigated in the vicinity of the K-absorption edge of diamond, which is used as a sample system and for which a resonant enhancement of XPDC is reported at the respective absorption edge.
In contrast to previous reports [34], for which mainly Compton scattering was consid-

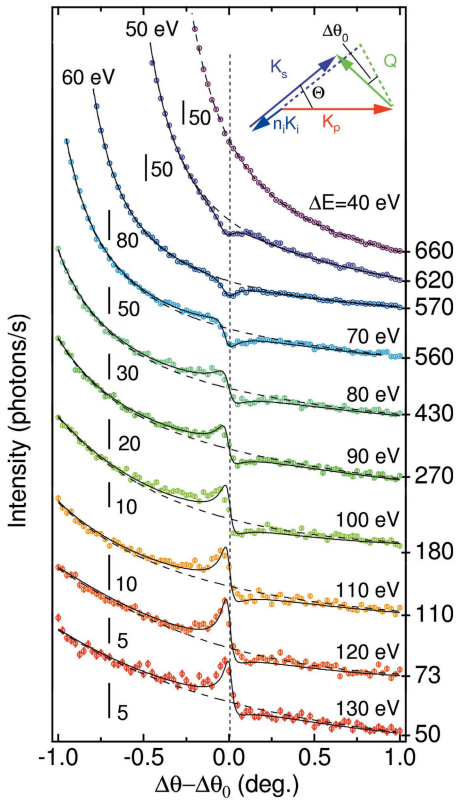

Figure 3.6: Rocking curves for various phase-matching conditions ranging from $E_p - E_s = \Delta E = 130$ eV to 50 eV. Solid lines present a fit by the model presented in [34]. Dashed lines refer to the estimated background, mainly Compton scattering. Vertical bars indicate the scale. Values on the right axis indicate the total signal intensity. Figure taken from Ref. [34].

ered, here x-ray Raman scattering[10] is taken into account as the dominant background contribution.

Experimentally, the approach remains unchanged with respect to previous experiments, except for a Zn foil, which is used for background suppression of (fundamental) Bragg scattered photons.

Sample angle scans for different idler energies are measured, ranging from 278 eV towards 343 eV (Figure 3.8). For the lowest investigated energy difference $\Delta E = E - p - E_s = E_i = 278$ eV, well below the absorption edge of carbon ($E_c = 289$ eV), the line shape corresponds to a Lorentzian. The asymmetry of the signal intensity grows while the idler energy $E_i = \Delta E$ approaches E_c. Above E_c, the line shape is character-

[10] In the case of x-ray Raman scattering, the pump photon scatters inelastically on a core electron and yields a photon with a reduced signal energy. As a consequence a core electron is excited into a state in the conduction band, taking up the energy difference.

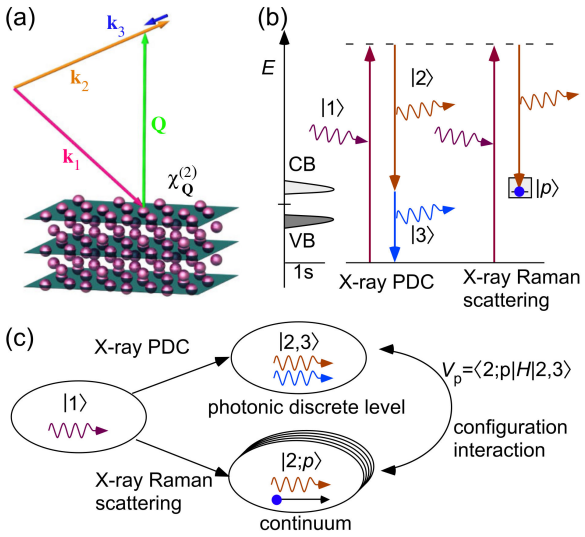

Figure 3.7: Schematics of phase-matching at lattice vector **Q** (a). Level diagram (b) includes the photon $|2\rangle$, generated by both x-ray Raman (inelastic x-ray scattering) and XPDC process. Conduction (CB) and valence (VB) band are indicated, respectively. The scheme for the quantum mechanical interference (c) includes the two competing processes. Figure taken from Ref. [35].

ized by a dip, explained as destructive interference.
An estimation of the second order nonlinear susceptibility (for a selected conversion ratio) is achieved via two steps: First, the power of the signal photon is extracted on the basis of the Fano formula. In a second step, the signal intensity is connected with the nonlinear susceptibility via solving a system of nonlinear wave equations [33]. Notably, these theoretical considerations presented, do not take the electronic structure of the material into account. It is found that the susceptibility at the absorption edge is an order of magnitude larger than the non-resonant part, both theoretically and experimentally.
This study contradicts the predictions of Freund and Levine [39], which states, that PDC should be suppressed at the absorption edge, yet this study reports an enhancement at the edge. A treatment for this enhancement at the absorption edges is presented by Barbiellini et al. [40] in 2015 on the basis of a renormalization approach.
Notably, the enhancement at absorption edges could not be confirmed experimentally for the L_1-absorption edge of silicon, even though silicon exhibits the same crystal structure as diamond.

3.2.3 Towards applications of non-degenerate XPDC

One of the first applications of x-ray parametric down-conversion is presented by Tamasaku et al. in 2011 [36]. The effect is used to image the three-dimensional

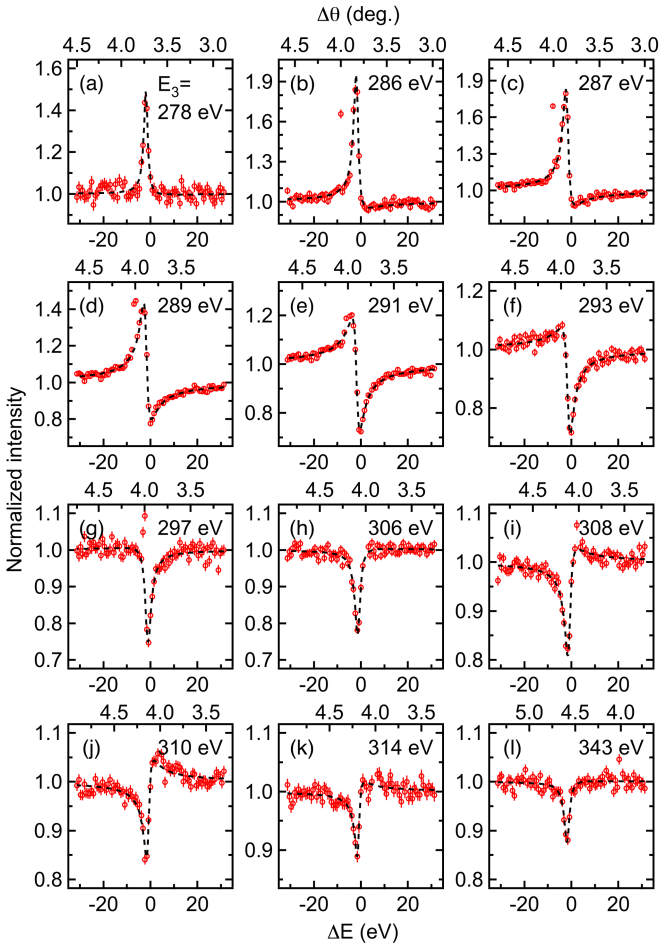

Figure 3.8: Rocking curve ($\Delta\theta$) scans referred to as Fano spectra (ΔE) by Tamasaku et al. [35] for a diamond sample covering idler energies (here E_3) from 278 eV to 343 eV (a-l). An enhancement of the signal is observed, when the idler energy is of similar value than the edge absorption energy ($E_c = 289$ eV) of diamond (d). Figure taken from Ref. [35].

wavelength-dependent optical response of a diamond crystal with atomic scale resolution of about 0.54 Å.

The local optical response is obtained from the second-order nonlinear susceptibility, which is determined experimentally via measuring the down-converted intensity for idler energies of $\hbar\omega_i = 60,\ 80,\ 100$ and 120 eV. In contrast to earlier works, the contributions from core and valence charges are not distinguished within the theoretical model. Yet, the authors make separate estimations for the linear structure factors of valence and core electrons, which are based on powder measurements and a topological

analysis tool (XD2006 [41]) to determine the charge densities for each electron type, respectively.
The local susceptibility changes are determined for different idler fields and are given relative to an overall average susceptibility. The latter being determined by tabulated refractive indices for diamond [42].
The reconstruction of the 3-dimensional optical response is achieved via Fourier synthesis, for which five different orientations (i.e., 111, 220, 311, the forbidden reflex at 222 and 400) are measured. The presented reconstruction method suffers from the phase-retrieval problem, since only the scattering intensities are measured experimentally while the phases of the fields are lost. Among all possible phases, those that yield a physically compatible result are taken into account. Beyond that reasoning no established procedure to determine the phase is presented.
On the basis of the experimental results, it is found that the linear response is extended, rather than local and therefore a bond-charge model is not reliable to explain XPDC in a diamond crystal.
The reconstructed microscopic linear susceptibility for the four idler energies (Figure 3.9) exhibit small spherical regions around the cores and respond in phase to the optical idler field. The disc-shaped regions respond out-of phase and have a stronger contribution to the optical response. A discrepancy between the local susceptibility and the valence electron distribution is reported. The authors suggest that this results from the higher density of the 1s core electrons compared to the out-of phase outer valence charges.
The study shows how - in principle - the effect of parametric down-conversion in the non-degenerate regime could be used for applications, namely by exploiting both the high resolution properties of hard x-rays in combination with the spectroscopic sensitivity by the idler field. As an outlook, the investigation of charge dynamics of strongly correlated systems is suggested, which could unveil a deeper understanding of physical properties of solid state materials.

3.2.4 Investigations of additional x-ray optical wave mixing processes

Within the context of non-degenerate XPDC the temporally reverse process of sum frequency generation and its experimental investigation shall be mentioned. The mixing of x-ray and optical frequencies, was studied experimentally by Glover et al. [43] in 2012 at the free electron laser LCLS.
Again, the process is understood as optically modulated diffraction of x-rays (see Section 3.2). The x-ray photons scatter inelastically on optically induced charge oscillations, by that probing this polarized charge. Different charge components can be probed by selecting a specific 'optical' idler wavelength. The authors also comment on difference frequency generation (DFG), later theoretically studied by Shwartz et al. [44], which follows a similar approach, except for a detection of a signal photon of difference energy[11].

[11] The theoretically proposed DFG process by Shwartz et al. [44] in 2015, discusses the mixing of two hard x-ray beams, yielding a difference frequency, i.e. the idler, which is in that specific case optical radiation,

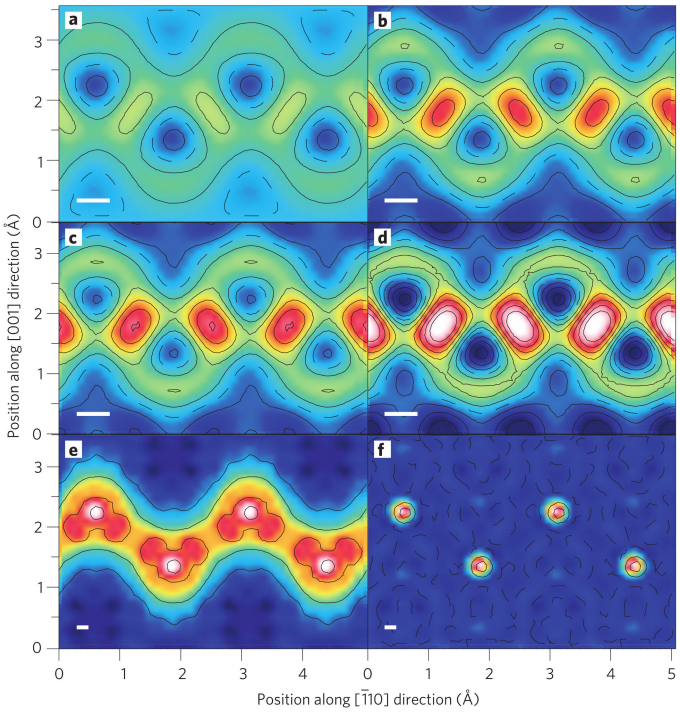

Figure 3.9: Reconstruction of the optical linear susceptibility on the basis of XPDC measurements for the 110-plane of diamond. The normalized linear susceptibility is presented for idler energies of $E_i = 60$ eV (a), 80 eV (b), 100 eV (c) and 120 eV (d). The reconstructed densities of valence (e) and core (f) electrons are presented. The spatial resolution is indicated by the white horizontal bars, yielding 0.54 Å. Figure taken from [36].

Experimentally, the process of sum-frequency generation is studied in single crystal diamond in 111 orientation. with x-ray pulses of 80 fs pulse duration, with $5 \cdot 10^{10}$ photons/pulse at 60 Hz repetition rate and a photon energy of 8 keV. The source for the optical photons is a pulsed optical laser at 1.55 eV (800 nm), 2 ps pulse duration and $1.5 \cdot 10^{10}$ W/cm^2. The mixed radiation at 8 keV + 1.55 eV is analyzed by a Si 220 channel cut crystal. Several scans are supporting the interpretation of the signal as SFG[12]: The signal vanished when the sample or detector was detuned from optimum phase-matching angles, or temporal overlap of x-ray and optical beams is removed. In the case of altering the polarization angle of the optical beam, the signal is reduced according to the magnitude of the polarization factor. At optimum conditions a count rate

yet other differences are possible.

[12]They supporting interpretation of the signal to stem from a nonlinear process are not transferable to XPDC experiments. These additional scans mainly rely on the modification of the parameters of the optical idler beam (e.g., polarization, intensity, etc.). Since XPDC requires only one incident beam, the above mentioned dependencies are not applicable.

of $4 \cdot 10^3$ cnt/s is measured, yielding a conversion efficiency of $3 \cdot 10^{-7}$. In addition, the bi-linearity is shown via the linear dependence of the detected SFG signal from optical laser power.
The theoretical model presented to describe the mixing of optical and x-ray frequencies is based on time- and space-dependent wave equations. Furthermore, the approximation of free electrons is used. The model predicts efficiencies of up to 10^{-3} under strongly idealized conditions, i.e., perfect beam collimation, monochromaticity, correct sample angles and optimal laser parameters[13]. The relatively high efficiency of SFG compared to XPDC is reasoned to stem from favorable mixing of x-rays with modes that are already occupied by the optical (idler) field.
Glover et al. suggest to follow the path of the previous studies by Tamasaku et al. [36], in which the optical response of the medium is imaged and suggest a similar approach for the SFG process. By detecting the intensity of the converted signal, the optically induced charge should be reconstructed in future studies. Beyond that, possible applications as a time-resolved probe are suggested, e.g., to study the electronic behavior of optically driven processes in solids and to investigate the subsequent bond dynamics.

3.2.5 Continuative studies on XPDC

In the context of studies concerning the parametric conversion of x-rays, a few additional reports are mentionable. These investigations focus on very specific details of the effect or use it for applications. The previously presented theoretical approaches are taken as a basis and are extended. In the case of experimental studies, established setups were reused and the effect exploited for applications.
One of these continuative studies was presented by Freund and Levine in 1970 on the polarization properties of the converted photon pair in the case of degeneracy [45].
In a similar manner as for optical PDC [46] the correlation between signal and idler photons became of interest. In that context the polarization entanglement of photons at x-ray energies generated by XPDC is discussed by Shwartz et al. [47].
Parametrically converted x-rays (in the degenerate regime) are used for experiments, which exploit the correlation of the converted photon pair. As an example, two-photon[14] x-ray diffraction can be used to improve the resolution beyond the diffraction limit [48].
In a similar manner, a method referred to as *Ghost imaging* was transferred from the optical [49] to the x-ray regime in recent years (2016-2018) aiming to improve the resolution of x-ray imaging experiments [50–52].

[13] These specific parameters are given in a very narrow range, namely by an x-ray energy and angle widths of 0.1 meV and 1 mrad and optical energy and angle widths of 10 meV and 1 mrad, respectively. A 500 µm long crystal is used and loss due to absorption is neglected. Mainly the x-ray beam parameters of monochromaticity and divergence are experimentally not feasible and are responsible for the four orders of magnitude between simulated and measured efficiency.

[14] for which the two photons originate from the XPDC process

3.3 Novel approach towards parametric x-ray conversion

The higher the asymmetry among the energy of the down-converted photon pair, i.e., the higher the non-degeneracy, the less applicable are previously presented theoretical models. XPDC in the non-degenerate regime needs to be considered within a fully quantized framework, avoiding classical concepts as used in earlier considerations. Such a framework is provided by a non-relativistic QED approach [53], for which the overall Hamiltonian is written as

$$\hat{H} = \hat{H}_{mat} + \hat{H}_{em} + \hat{H}_{int}.$$

The expression is divided into the description of the material by $\hat{H}_{mat}$, the light fields by $\hat{H}_{em}$, including the photonic fields of x-ray (signal) and optical (idler) radiation and the interaction part $\hat{H}_{int}$, describing the coupling between light and matter.
The interaction Hamiltonian includes two components commonly known as A^2 and $p \cdot A$ -term. The A^2 -term describes the coupling of electro-magnetic fields to charge densities ($\rho(\vec{x})$), whereas the $p \cdot A$ -term describes the coupling of a field to a current density ($\vec{j}(\vec{x})$). These couplings are conceptually shown by the respective Feynman diagrams in Figure 3.10.

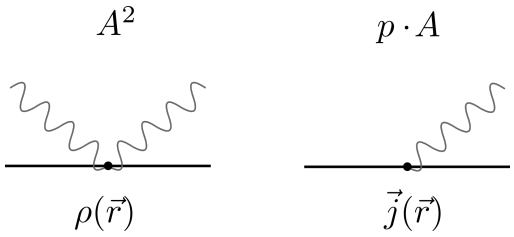

Figure 3.10: Feynman diagrams for the A^2 and $p \cdot A$ -terms of the interaction Hamiltonian non-relativistic QED.

In the all-optical regime of parametric down-conversion, it is sufficient to describe the light-matter interaction by the $p \cdot A$ -term, as a direct consequence of the dipole-approximation. In that regime photon energies are low enough to neglect the influence of the A^2 -term. In the x-ray regime, however, the A^2 -term needs to be considered to fully describe the interaction. For XPDC in the non-degenerate regime, the following relevant combinations (Figure 3.11) of interaction diagrams need to be taken into account.
This implies that the fundamental electronic quantity, which is being probed, is a density-current-density correlation function. The interpretation and application, e.g., in the context of imaging techniques, are currently investigated.
The full description of this theoretical approach is elaborated in Ref. [53], in which conversion efficiencies[15] of 10^{-15} are predicted. Integrating over the spectral ranges

[15] i.e., converting 10^{15} incident pump photons into one pair of down-converted photons.

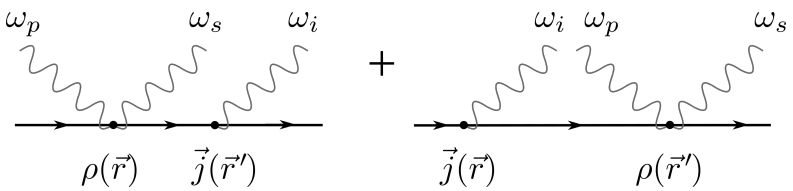

Figure 3.11: Relevant combinations of interaction terms for describing XPDC in the non-degenerate regime. The interactions are represented by Feynman diagrams and ω_p, ω_s and ω_i refer to the frequencies of the pump, signal and idler photon, respectively.

of the incident monochromator and the analyzer bandwidth, together with a realistic (experimentally achievable) solid angle, the conversion efficiency can yield 10^{-13} to 10^{-12}.
Due to its recent development, the implications of this theory are not fully considered within this experimental work[16].

[16]e.g., the predicted scattering cone in horizontal and vertical dimension for a fixed sample angle is not investigated by the experimental study. Only the horizontal scattering for sample angle scans is investigated.

Chapter 4

Experimental Setup

The requirements and prerequisites to experimentally measure the parametric conversion of x-rays into pairs of x-ray and optical photons is presented in the following chapter.
The first section provides a brief overview of x-ray sources with an emphasis on synchrotron radiation sources and x-ray free-electron lasers, following Ref. [54]. It is continued by an introduction of basic principles of x-ray monochromatization and a subsequent presentation of the fundamentals of a diffraction experiment, focusing specifically on high resolution diffractometry. Finally, the experimental setup used to investigate the parameter space of x-ray parametric down-conversion is presented.

4.1 X-ray Sources

Parametric down-conversion of x-rays can - in principle - be investigated by conventional sources, such as x-ray tubes, as it was reported by Eisenberger and McCall [16]. However, due to the low conversion efficiencies in combination with the low monochromatic flux of tube sources, event rates of ~ 1 down-converted photon pair per hour could be observed. 3rd-generation synchrotron sources, transform limited storage rings and x-ray free electron lasers (XFEL) enable the systematic study of these low conversion rate effects, providing sufficient flux and possibly a pathway to enable the effect's applications. As such, quantum x-ray experiments, like the parametric conversion of x-rays, demand for high brightness sources, which will be introduced in the following section.

4.1.1 Synchrotron Sources

The high potential of x-rays to study the nature of matter became apparent immediately with the (first) systematic investigation of this radiation by W. C. Röntgen in 1895 [55]. Since then, progress was not only achieved in the theoretical understanding of the interaction of x-rays with matter, but an equal emphasis was put on the development of sources. Synchrotron radiation was experimentally discovered in 1940 at an electron

accelerator [56] and theoretically explained by Schwinger [57] a few years later. In general, synchrotron radiation is emitted by relativistic[1] charged particles, which are accelerated by an electromagnetic field.
From its discovery in the 1940s when photon production was still parasitically used, accelerator based sources advanced with an optimization of performance with regard to the *brilliance* of the photon source. The brilliance is used as a numerical parameter to quantify, characterize and compare the quality of light sources (Figure 4.1). It is

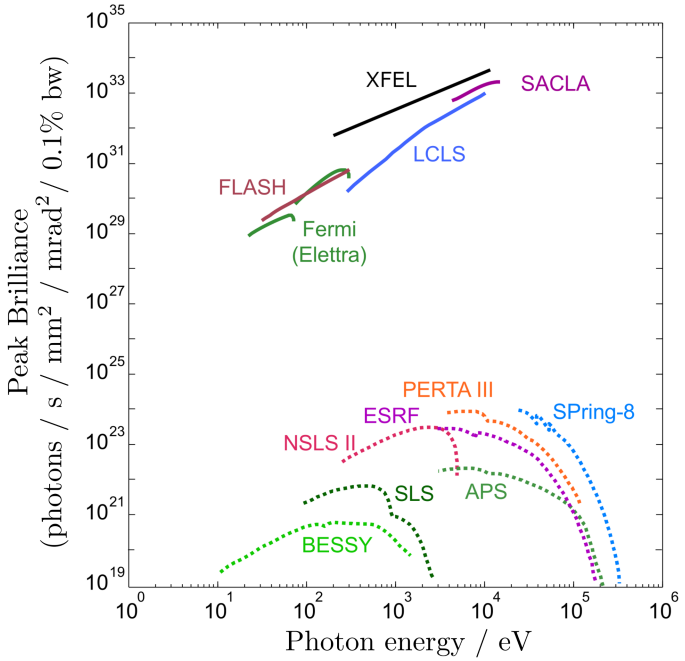

Figure 4.1: The peak brilliance of various x-ray sources. The synchrotron sources BESSY, NSLS, SLS, ESRF, PETRA, APS and SPring-8 range orders of magnitudes lower than the free electron lasers FLASH, Fermi, LCLS, XFEL and SACLA [58]. Conventional x-ray tube sources are found far below the scale ($\sim 10^{12}$).

defined as

$$\text{Brilliance} = \frac{\text{Photons/second}}{(\text{mm}^2)\ (\text{mrad})^2\ (0.1\%\ \text{BW})}$$

and describes the number of photons within 0.1% bandwidth that pass per second, normalized to the beam divergence and cross-sectioned area.
The brilliance of x-ray light sources has improved by more than twelve orders of magnitude over the last 65 years [54]. This was achieved by dedicated facilities, i.e., electron storage rings, serving solely as x-ray light sources.

[1] i.e., velocities comparable to the speed of light

A main feature of synchrotron radiation is the strong *collimation*, i.e., its strongly pronounced forward emission characteristic with small divergence. A property directly relating to the brilliance of the source and originating from a relativistic effect, which is depicted in Figure 4.2.

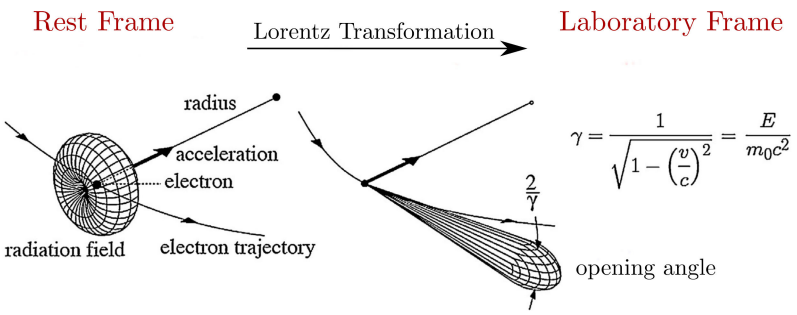

Figure 4.2: The emission pattern of a charged and accelerated particle (dipole) in the particle's rest frame (left) and in the laboratory frame (right), to which is moves at the velocity v. The transformation between rest and laboratory frame is performed by Lorentz transformation. Graphic adapted from Ref. [54].

An electron on a circular trajectory emits characteristic (dipole) radiation, which is shaped like a torus in the electron's rest frame. Yet, the electron moves with relativistic velocity, i.e., close to the speed of light. The coordinates describing the trajectory of the charge can be transformed by a Lorentz transformation into the laboratory frame, where the same emission appears strongly peaked in forward direction. Since the electron moves on a circular arc, radiation is emitted in tangential direction with an opening angle proportional to $1/\gamma$.
The emission characteristics of the here presented arc radiation can be improved further by introducing dedicated insertion devices, the so-called wigglers and undulators.

Insertion Devices

Wigglers and undulators are periodic arrangements of magnets with alternating magnetic fields. These structures deflect the trajectory of the electrons periodically; causing repeated acceleration in segments of arcs. As these structures are inserted in the straight sections of the storage rings, they are referred to as *insertion devices*. The difference between wigglers and undulators is only of quantitative nature. For magnetic field strengths causing a deflection of the electrons larger than the natural opening angle $1/\gamma$ (Figure 4.2) the device is called wiggler (with magnetic field strengths of $B_{wiggler} \approx 7$ T), whereas for smaller deflections the device is referred to as undulator ($B_{undulator} \approx 1$ T). The dimensionless deflection parameter K is typically used to distinguish between these devices; it is defined as [54]

$$K = \alpha \cdot \gamma,$$

where α defines the maximum deflection angle and γ the reduced energy E/m_0c^2. With the period of the magnetic structure λ_u and the magnetic field strength B_0 the K-parameter can also be formulated as

$$K = 0.943\ \lambda_u(\mathrm{cm})\ B_0(\mathrm{T}). \tag{4.1}$$

The emission characteristics of an undulator (wiggler) is determined by coherent superposition of radiation, which is achieved in the following manner: Within the insertion device an electron and its emitted radiation effectively propagate with the speed of light. Yet, the electron's trajectory is bent and thereby longer. If this difference in pathlengths of the electron and the radiation for each undulator period λ_u is equivalent to the wavelength of the emitted radiation, a constructive interference of the emission is observed. The resulting emission spectrum of an undulator is therefore characterized by harmonic peaks at wavelengths λ_n with

$$\lambda_n = \frac{\lambda_u}{2n\gamma^2}\left(1+\frac{K^2}{2}+\gamma^2\theta^2\right) \quad \text{for} \quad n = 1,2,3,\ldots$$

where n indicates the harmonic and θ the angle of the observation point relative to the undulator axis. Using standard relations [54] the wavelength can be converted to the photon energy E_n of the harmonics

$$E_n(\mathrm{keV}) = \frac{0.95\ n\ E^2(\mathrm{GeV})}{\lambda_u(\mathrm{cm})}\frac{1+K^2}{2+\gamma^2\theta^2}.$$

By changing the effective magnetic field B_0 via mechanically altering the undulator gap, the K-parameter (equation 4.1) and thereby the emitted energy can be tuned. A comparison of the spectral outputs of bending magnets, wigglers and undulators is presented in Figure 4.3. The brilliance of a wiggler exceeds the emission of bending magnets and increases proportional to the number of periods N. The undulator's spectrum peaks at the harmonics and its brilliance scales with N^2 [54]. The spectral ranges of the undulator harmonics are again adjusted by tuning the gap; their range being indicated in Figure 4.3.

Today, 3rd-generation machines are state-of the art synchrotron sources with planned and partly performed upgrades to diffraction limited storage rings (DLSR). These facilities will profit from improved beam dimensions, namely a minimized emittance[2]. The application of multi-bend achromat magnets [59, 60] will improve the brilliance by another two or three orders of magnitude [54] and will enable total control of the photon beam polarization. Furthermore, due to the lower emittance and resulting circular electron beam footprint, the emitted radiation is fully coherent in both transverse directions.
Currently the facility Max IV [60] is already operational and the EBS [61], as an upgrade of the ESRF, is getting available for user experiments in the upcoming months.

[2]The emittance is a property of charged particle beams. It describes the average spread of the particles in phase-space, i.e., the position and momentum space.

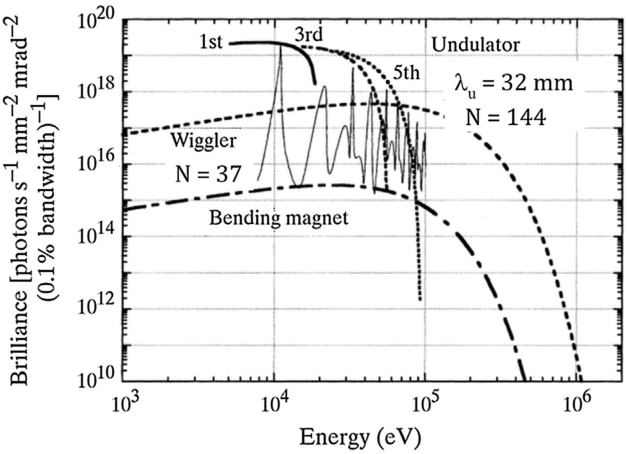

Figure 4.3: The energy dependent brilliance characteristics of different sources: bending magnet, wiggler and undulator at the SPring-8 facility [54].

4.1.2 X-ray Free Electron Lasers

In parallel to the developments for diffraction limited storage rings, other technologies are pursued to further increase the brilliance of x-ray sources.
One of these approaches are x-ray free electron lasers (XFELs), which are based on linear accelerators[3], delivering ultrashort pulses in the regime of femtoseconds (10^{-15} s) [65] and high peak brilliance (10^{33} photons s^{-1}mm^{-1}mrad^{-1}0.1%bw) [66].
These very special set of parameters might enable the application of XPDC as a new material probe. The high intensities should enable reasonable signal rates, while the short pulses could provide the temporal resolution of valence electron properties (see Chapter 8).
The functionality of XFELs are based on long (up to 200 m) undulator sections, which enable electron bunches to emit coherent radiation [67], resulting in an increase of brightness by another ten orders of magnitude (Figure 4.1). This characteristic is achieved by a process referred to as *Self Amplification by Stimulated Emission* (SASE), in which the interaction of the emitted photon field with the co-propagating electron bunch causes a spatial modulation of the electron bunch. The field stimulates the emission of subsequent photons from the same electron bunch, thus causing the whole bunch to emit radiation with the same frequency and phase. The emission is amplified along the undulator length until saturation is reached (Figure 4.4). In saturation, the resulting micro-bunches will have a periodicity equal to the emitted photon wavelength. The radiation is transversely fully coherent and the pulse lengths are on the order of a few to 100 fs.
The coherently amplified radiation of a SASE XFEL exhibits a spectral spread in the order of $30-50$ eV. To obtain amplification within a more narrow energy range a FEL

[3] superconducting accelerator cavities [62–64] in the case of the European XFEL

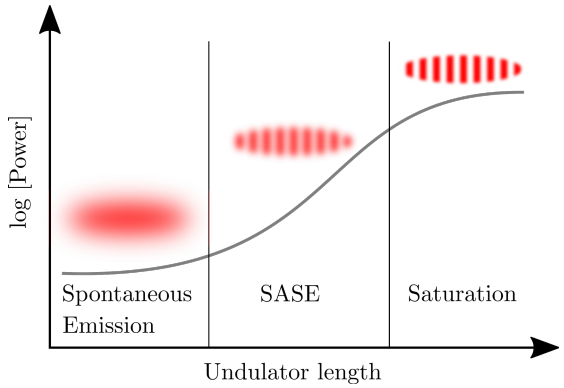

Figure 4.4: Relation of undulator length and emitted power by the electron bunch. The behavior can be divided into three segments: For small undulator lengths, the emission is comparably weak and purely spontaneous. For increasing undulator lengths the emission grows exponentially as the SASE effect sets in. For even larger undulator lengths the emission reaches saturation. The electron bunch is structured microscopically on the length scales of the emitted radiation as shown in the upper schematic images of the electron bunch.

can be operated in *seeded mode*.

Self-Seeding A self-seeded free electron laser selects a narrow wavelength band from its initial emission spectrum and uses it as the seed for stimulated emission.
The original concept was introduced by Feldhaus et al. [68] and Saldin et al. [69], who suggest a conventional x-ray monochromator as an energetic filter.
In practice, a slightly different approach was ultimately established at different XFELs [70, 71]. After few undulator segments, the spectrally broad spontaneous emission is separated from the co-propagating electron bunch. By kicking the electrons through a chicane. A narrow spectral filter[4] is applied to the photon bunch, e.g. by using a single crystal diamond in forward Bragg diffraction [70]. The crystal filters the selected wavelength, such that it is not present in the transmitted spectrum (Figure 4.5 b). Since the generated photon pulse is short in time, it is expanded in the frequency domain. Removing a specific narrow band spectral component (Figure 4.5 a) causes a ringing effect of this frequency component in time (Figure 4.5 c), the so-called wake-pulse [72]. The wake decay time is inversely proportional to the width of wavelength band selected by the filter. Since the wake is expanded in time it stimulates the emission along the longitudinal dimension of the electron bunch, once the electron and photon bunch are jointly propagating again. As such, the selected bandwidth is predominantly

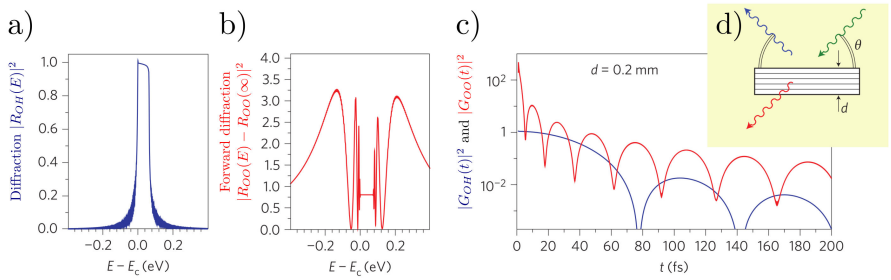

Figure 4.5: Spectral and temporal behavior of the reflected and transmitted intensity for regular (a) and forward (b) Bragg diffraction [70]. Results are obtained on the basis of dynamical diffraction theory for a diamond in 400 orientation at $E_c = 8.333$ keV. The spectral distribution of Bragg reflected intensity (a) is missing in the frequency domain of the transmitted spectrum (b). The selected bandwidth is, however, extended in the time domain and is used as a 'seed' for the successive amplification process.

amplified in the successive undulator sections.
At the LCLS and SACLA free electron laser facilities, this concept has been successfully demonstrated [70, 71] for the hard x-ray regime and at European XFEL it is currently being implemented [73].
Self-seeding effectively reduces the broad SASE spectrum ($\sim$ 30 eV, FWHM) to a reduced bandwidth of 1.3 eV (FWHM) as exemplary shown for time averaged measurements at LCLS (Figure 4.6). Self-seeded pulses are considered as almost Fourier-transform limited, i.e., being a pulse of minimal possible duration for a given band-

[4] A bandstop filter passes most frequencies unaltered and only stops or attenuated frequencies in a specific band.

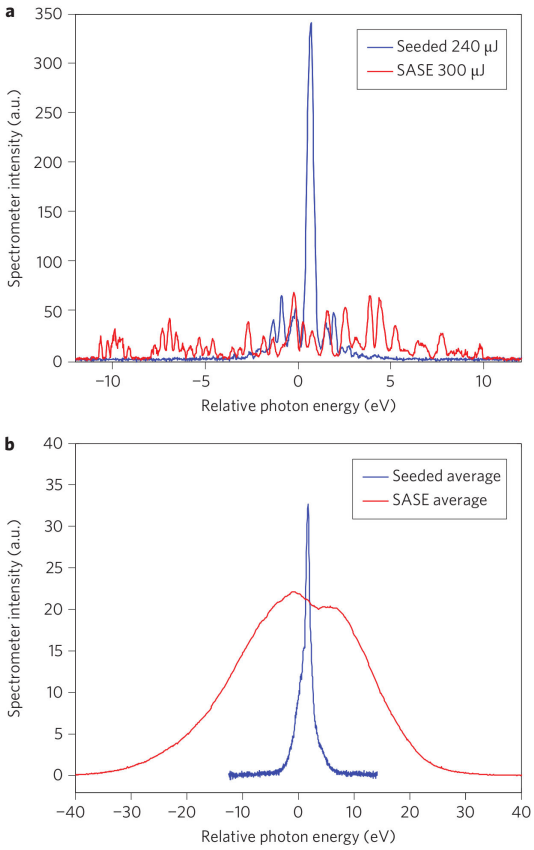

Figure 4.6: Measured spectra resulting from SASE (red) and seeded mode (blue) at LCLS: single shot measurements (a) and time-averaged data (b). Graphic from [70].

width. In the case of the SACLA seeded mode, the pulse duration is estimated by Inoue et al. [65] to be as short as ~ 6 fs.

Finally, it should be notated that, despite the relatively narrow spectral emission characteristics of the SASE process, concurrent spontaneous emission of synchrotron radiation occurs along the full undulator length. This emission results in a broad background spectrum, which can only be suppressed by additional monochromatization of the photon beam.

4.2 Principles of X-ray Monochromatization

A monochromator is a component, which enables the spectral filtering of radiation. As such, it can be used to select a narrower bandwidth from the undulator radiation in front of the sample or to energetically filter the radiation after interaction with the sample; in

the latter case it is commonly referred to as an *analyzer*.
In the experimental setup (presented in section 4.4) used to observe parametrically down-converted x-ray photons, monochromators are integral components and determine the setup's spectral resolution. Only by their integration, a differentiation of the weak nonlinear signal from the linear background scattering (e.g. thermal diffuse scattering or Bragg scattering) becomes possible.

In general, the characteristic properties of monochromatization are given by the relative spectral resolution $\Delta E/E$ (or its energetic bandwidth ΔE), the angular acceptance $\Delta\theta$ and the peak transmitivity T, or reflectivity R [4].
Most x-ray monochromators consist of crystalline material and their functionality is based on the diffraction characteristics of the crystal lattice.
Multiple-crystal configurations and their applications for spectral filtering have been discussed to great extent by Compton and Allison [74], Zachariasen [75], Pinsker [13] and Authier [76]. A detailed discussion of x-ray monochromator configurations for various applications is presented by Shvyd'ko [4].

To select x-rays within a small spectral spread, different methods can be applied. Here four possible approaches shall be mentioned:

(i) The Bragg reflection from a perfect crystal itself is a spectral filter and results in a narrow spectral width $\Delta E/E$, which is (almost) constant with respect to changes of E for a given Bragg reflection [4]. The resolution ranges from 10^{-4} to 10^{-5} for low index[5] reflections, and reaches up to $\Delta E/E \backsimeq 10^{-9}$ to 10^{-10} for high index reflections.

(ii) Asymmetric Bragg diffraction can be used to obtain a narrower spectral spread. In contrast to a symmetric reflection the lattice planes are not orientated parallel to the surface. For an asymmetric reflection geometry the crystal's surface is cut under an angle α with respect to the lattice planes (Figure 4.7). Even though the intrinsic spectral and angular spread of a reflection can be modified by applying an asymmetric geometry, real sources, having a finite divergence, prevent the direct improvement of spectral and angular spread. As such, a combination of asymmetric crystal geometries needs to be applied [4]. As an example, the simplest combination includes two reflections. The first reflection reduces thereby the incident angular spread of the source and the second reflection yields the small spectral spread.

(iii) Another method to achieve monochromatization is by angular dispersion. In contrast to the previous approaches, this method relies less on the specific angular and spectral widths of a reflection. However, it requires a more complex configuration, which includes three components, namely the *collimator* (C), a *dispersive element* (DE) and a *wavelength selector* (W) (Figure 4.8). With such a configuration spectral spreads of $\Delta E/E \backsimeq 10^{-7} - 10^{-8}$ are possible. A detailed description of this concept is found in Ref. [4].

[5] Here, index refers to the Miller indices (*hkl*), describing the lattice planes, on which the reflection takes place.

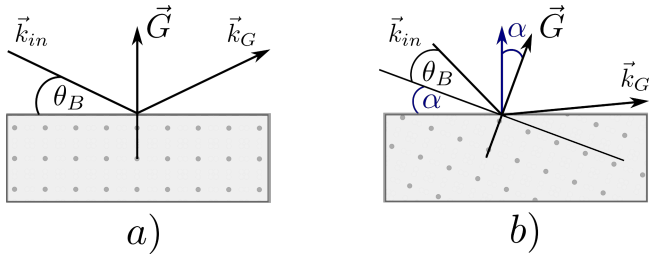

Figure 4.7: Symmetric (a) and asymmetric (b) Bragg reflection at perfect crystals. In the symmetric case, the scattering lattice planes are parallel to the surface. For asymmetric Bragg scattering, the lattice planes are tilted by an angle α with respect to the surface. The incident radiation $\vec{k}_{in}$ is scattered at an angle θ_B or $\theta_B + \alpha$, where θ_B indicates the Bragg angle and $\vec{k}_G$ the scattered wave vector.

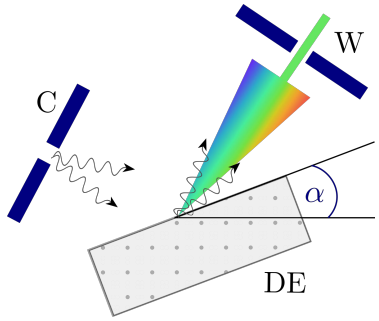

Figure 4.8: Schematics of a dispersive configuration to obtain monochromatization of x-rays: the collimator (C) is followed by the dispersive element (DE) - here a crystal in asymmetric geometry - and a wavelength selector (W).

(iv) Apart from the spectral and angular characteristics of crystal reflections, the reflectivity itself can be used for monochromatization. This can be achieved by an interferometer (Fabry-Perot), in which the crystals are used as mirrors for the resonator [4, Chapter 5.6]. The higher the reflectivity, the higher the finesse of such a resonator and the sharper the resulting resonance, which results in a narrow spectral acceptance. By this method $\Delta E/E$ in the order of µeV are feasible.

The investigation of x-ray parametric down-conversion requires a moderate energy resolution (see Chapters 5.1 and 5.2). Photon energy differences (between fundamental and down-converted photons), which need to be differentiated, range from 10 eV down to 0.5 eV. Lower index reflexes as Si 111 and Si 311 are chosen for the incident monochromator and Si 440 is chosen for the analyzer, since they provide energy resolutions of 1.3 eV for the first crystal and 0.3 eV for the other.
Studying a low cross section effect, as presented here, requires a high incident photon flux, which can only be retained at a moderate energy resolution. This is the reason for choosing low index reflections in this case. Monochromatization for the here presented

experimental study relies on the principle presented under (i), the symmetric Bragg reflection. The other methods are presented for completeness.
Subsequently, the determining characteristics of monochromatization, i.e., the spectral bandwidth, reflectivity and suppression of the spectral tails are discussed in detail in the following section.

Spectral Bandwidth

The spectral bandpass of a monochromator is given by its *intrinsic* and *geometrical* widths, are each determined for the central wavelength λ_c of an incident spectrum [4]

$$\frac{\Delta\lambda}{\lambda_c} = \left(\frac{\Delta\lambda}{\lambda_c}\right)_{intrinsic} + \left(\frac{\Delta\lambda}{\lambda_c}\right)_{geometrical}. \tag{4.2}$$

A multiple reflection monochromator can be realized by crystals, for which a propagation channel is cut through the crystalline material. These configurations offer the advantage, that the lattice planes are already aligned with respect to each other, since being cut from the same single crystal. For a multiple-bounce monochromator the obtained spectral width deviates only slightly from a single crystal reflection. But the second reflection restores the photon beams direction and increases the suppression of the spectral tails, yet causing a geometrical beam offset (Figure 4.9 top, inset).
The intrinsic spectral width $\varepsilon_H^{(s)}$ of the Bragg reflections of Si 111, Si 311 and Si 440 (which are used in the experiment for monochormators and analyzers) are given by [4, Appendix 3]

$$\varepsilon_H^{(s)} = \left(\frac{\Delta\lambda}{\lambda_c}\right)_{intrinsic} = \begin{cases} 11.025\cdot 10^{-11} & ;\text{for Si 111} \\ 2.799\cdot 10^{-11} & ;\text{for Si 311} \\ 0.947\cdot 10^{-11} & ;\text{for Si 440} \end{cases} \tag{4.3}$$

The overall width is broadened by the angular divergence of the incident beam $\underline{\Delta}\theta$, yielding an additional contribution: the geometrical spectral width for a 2-bounce configuration is given by [4, Chapter 5.3.1] as

$$\left(\frac{\Delta\lambda}{\lambda_c}\right)_{geometrical} = \begin{cases} \frac{\underline{\Delta}\theta}{\tan\theta_c} & ;\text{for } \ 0<\theta_c<\frac{\pi}{2} \\ \underline{\Delta}\theta(\frac{\pi}{2}-\theta_c) & ;\text{for } \ \theta_c\leq\frac{\pi}{2} \\ \frac{(\underline{\Delta}\theta_c)^2}{2} & ;\text{for } \ \theta_c=\frac{\pi}{2} \end{cases}$$

Reflectivity

For the here presented experimental setups, silicon crystals are used as incident monochromator and analyzer in three different orientations, namely in 111, 311 and 440. The reflection properties of these orientations vary with respect to angular acceptance width (Darwin width [77]) and peak reflectivity (Figure 4.9, for 10 keV). The overall reflectance of silicon crystals is high, regardless of the chosen reflex. The theoretically

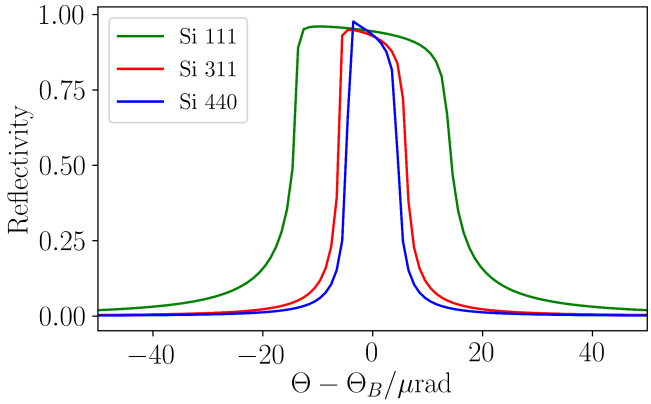

Figure 4.9: Simulated reflectivity curves (s-polarization) of Si 111, Si 311 and Si 440, respectively, for 10 keV. The theoretical peak reflectivity values are determined to 0.96, 0.95 and 0.97. The angular width, i.e., the Darwin width, varies for the respective reflections. Calculations performed on the basis of dynamical diffraction via OASYS [78].

obtained peak values are determined to 0.96, 0.95 and 0.97 for the different orientations, respectively. The reflectivities are high enough to not cause a substantial decrease of intensity. The unreflected fraction of the energy is either transmitted or absorbed by the material.
The width of the reflectivity curves is determined by the angular acceptance of the respective reflex, i.e., the Darwin width. For the here presented reflections (at 10 keV) they yield 28.14, 11.06 , 9.05 µrad, respectively. The above considerations were made for a collimated beam.
The reflectivity of a Bragg reflection is highest in the case of backscattering. For silicon this property exceeds values of 90% in the range from 3 to 8 keV at room temperature. The reflectivity decreases proportional with the incident photon energy, since the influence of thermal vibrations impact the Bragg condition for small wavelengths in a more pronounced manner. For high photon energies (i.e. $\sim$ 100 keV) materials with higher Debye-temperature[6]can be chosen, e.g. Al_2O_3[7]. Active cooling increases therefore the reflectivity of x-ray optics.

Suppression of spectral tails

Beyond the bandwidth and the reflectivity, the suppression of the spectral tails is an important characteristic of crystal monochromators and a crucial factor for the successful

[6]The Debye-temperature is a material dependent parameter, which described the behavior of phonon frequencies, in this context the ability to convert heat to lattice vibrations [79].
[7]having a Debye-temperature of $\Theta_D \cong 900 - 1000$ K.

detection of XPDC.
In contrast to optical beams, obtaining a *monochromatic* beam of x-rays is more involved. This issue can largely be traced back to the radiation sources themselves. In the case of optical radiation, narrow bandwidth lasers are available, which intrinsically emit with small spectral spreads. Furthermore, the low photon energies are easily absorbed by materials.
In the case of x-rays a broad spectral range is emitted by wiggler and undulator sources and the transmission of these high energy photons is high. Using crystal reflections to monochromatize this radiation works only within the limits of their spectral and angular characteristics (see Section 4.2). Thus, the elimination of the spectral tails cannot be achieved entirely and is merely approached via successively stronger suppression.
In the case of parametric conversion of x-rays into visible photons, the difference between the central pump E_c and down-converted energy E_s is small, i.e., a few electron Volts. The bandwidth (FWHM) of a Si 111 crystal, used for a typical high heat load monochromator, is approximately 1 eV. The magnitude of suppression of other wavelengths depends on the chosen reflex, as well as the number of reflections (Figure 4.10).
The effects of the monochromator and analyzer configurations with respect to expected reflectivity and spectral tail suppression are simulated with the ray tracing program Oasys [78] which is based on SHADOW3 [80] and ShadowOui [81]. On the basis of these simulations, an order of magnitude estimation is presented for the different multi-reflection configurations.
Notably, the simulated result does not contain thermal effects, which affect the reflectivity and may ultimately enhance the tails [82]. However, within an order of magnitude argumentation the simulated data for perfect crystals is sufficient.
In the specific case of the Si 111 crystal in the single-bounce configuration, energies at 2, 4 and 6 eV off the fundamental wavelength are suppressed by factors of 25, 100 and 300, respectively. In the double-bounce configuration in comparison, the same energies are suppressed by factors of 500, $1.6 \cdot 10^4$ and $7.4 \cdot 10^4$, respectively. A further improvement is obtained with higher index reflections, e.g., Si 311 (Figure 4.10, bottom).
The combination of Si 111 and Si 311, both in double-bounce configuration (channel-cut crystals) are used for a high resolution configuration. The resulting bandwidth is 0.3 eV (FWHM) and the suppression of the spectral tails is strong.

In addition to the monochromator, which determines the spectral purity of the incident beam, multiple-bounce crystal configurations are used for the analyzer.
For the here presented experimental setups, two different configurations are used. A 3-bounce Si 111 analyzer is used for experiments at the Diamond Light Source (I16) and a Si 440 two-bounce crystal is used at the ESRF (ID20). The higher order reflex (Si 440) yields a bandwidth of 0.3 eV (FWHM) in comparison to the Si 111, with 0.6 eV in the 3-bounce configuration. The difference in the suppression of the spectral tails between this two configurations is pronounced (Figure 4.11).

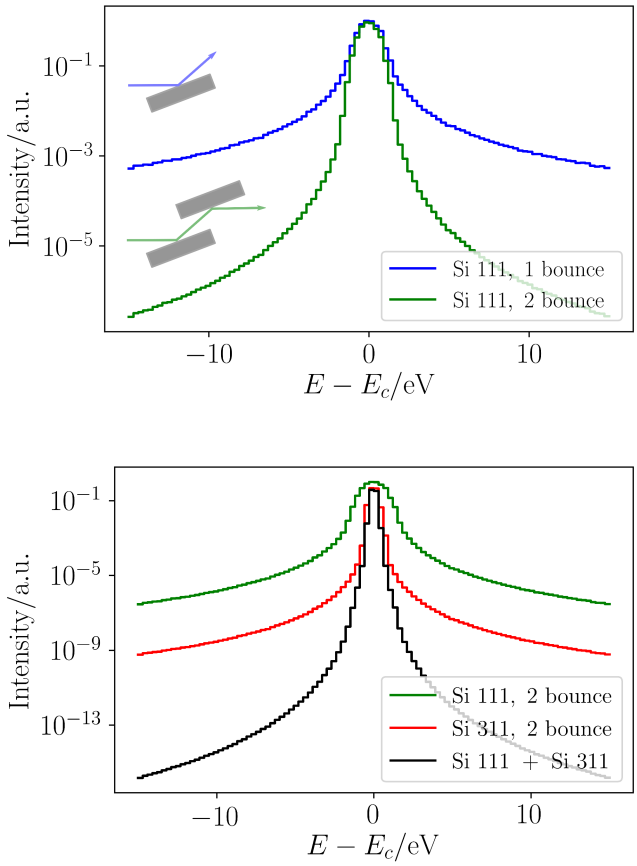

Figure 4.10: Spectral transmissivity curves of monochromators. The difference between a 1-bounce and 2-bounce configuration of a Si 111 crystal at the central energy $E_c = 10$ keV is observed in the suppression of the spectral tails (top), the bandwidth of ~ 1 eV (FWHM) is almost unchanged. The behavior of different orientations, i.e. Si 111 and Si 311, is compared (bottom). The Si 311 orientation yields a narrower bandwidth of 0.3 eV (FWHM). A combination of Si 111 and Si 311 (both 2-bounce) is used for a high resolution configuration. Calculations performed on the basis of dynamical diffraction via OASYS [78]

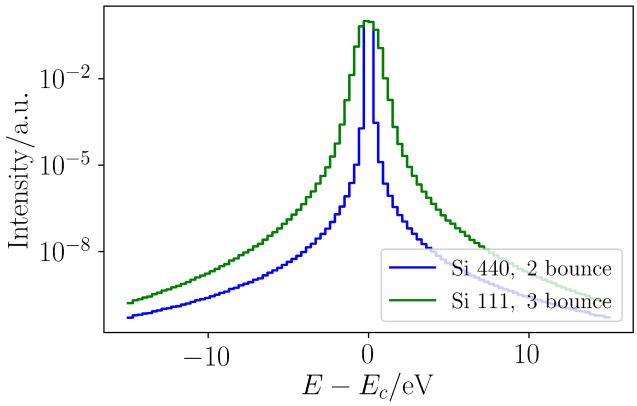

Figure 4.11: Spectral transmissivity of analyzers: Si 440 in double-bounce and Si 111 in triple-bounce configuration. The double-bounce Si 440 has the smaller bandwidth (0.3 eV (FWHM)) and - despite one reflection less than the Si 111 - the stronger suppression of spectral tails.

4.3 High Resolution Diffractometry

The experimental setup for investigating x-ray scattering processes consists of five integral parts (Figure 4.12): The x-ray source, beam diagnostic and manipulation via x-ray optics, the sample, the analyzing element - again via x-ray optics - and finally the detector. The incident beam parameters on the sample are described by the bandwidth

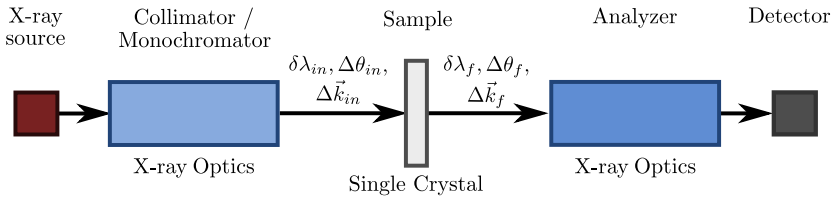

Figure 4.12: Implementation of a fundamental scattering experiment including integral elements: the x-ray source, the monochromator stage (including additional x-ray optics), the sample, the analyzer stage and the detector. The incident beam is characterized by the bandwidth $\delta\lambda_i$ and divergence $\Delta\theta_i$. The outgoing beam has a divergence of $\Delta\theta_f$ due to the interaction with the sample.

$\delta\lambda_{in}$ and the divergence $\Delta\theta_{in}$ (or incident angles $\Delta\vec{k}_{in}$). After the interaction with the sample system, the outgoing beam including its divergence $\Delta\theta_f$ is analyzed by additional x-ray optics and the scattered signal is recorded by the detector.
Experimentally, a scattering experiment is enabled by the usage of the above mentioned components in combination with a diffractometer, on which sample, analyzer stage and detector are typically integrated (Figure 4.13). The sample is positioned in the center of the diffractometer, where a rotation (Ω) around its axis is enabled. The incident optics steer the beam onto the sample, where it diffracts. The detector circle can be rotated around the sample, moving on the so-called 2θ-circle. Many high-end diffractometers allow for an additional movement of the detector arm out of the scattering plane. The scattering plane of a diffraction experiment is defined by the incident and scattered beam[8].
The specific term *high resolution diffraction* typically refers to the angular resolution with respect to sample rotation and resolution of the scattered radiation on the 2θ-circle. A high resolution diffraction setup is capable of resolving the Darwin width (e.g., $w = 5.6176$ µrad for diamond in 220 orientation for $E = 10$ keV, π-polarized).
In the case of the experimental setup for XPDC measurements, a special emphasis on resolving the scattered signal spatially *and* energetically is made.

[8]Typically for XPDC experiments this plane is parallel to the synchrotron ring and therefore referred to as horizontal scattering plane.

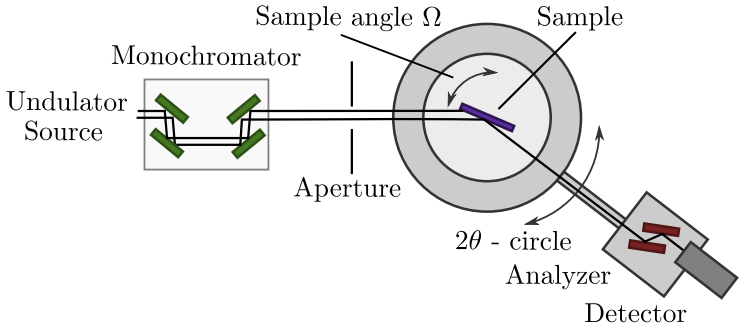

Figure 4.13: Schematic setup of a high resolution x-ray diffractometer: The monochromatized beam impinges on the sample, which is positioned in the center of the diffractometer. For any sample rotation (Ω) the scattered intensity can be recorded around the 2θ-circle. To this end, the analyzer stage and detector are jointly assembled on a movable arm. Image adapted from [83].

4.4 Experimental Setup

Unequivocal proof for the effect of XPDC is acquired by detecting the generated photon pair in coincidence, as it was done in the early experiments of Eisenberger and McCall [16]. In that study, the effect was investigated in the degenerate regime, i.e., signal and idler photons having the same photon energy ($E_s = E_i = 8.5$ keV). The sample angle for XPDC for that specific case differed from the Bragg condition by $\Delta\Omega = 0.25$ deg and the two x-ray detectors were positioned symmetrically around the scattering angle for Bragg reflection ($2\theta_B$). The separation of these two detectors amounted to 15 deg (compare to Figure 4.13 but with two detectors).
Increasing the asymmetry of energy distribution among signal and idler photon, i.e., going towards higher non-degeneracy ($E_s \gg E_i$), experimental difficulties arise for implementing a coincidence detection. An idler photon in the UV-regime[9] will be (re-)absorbed by the sample and cannot be detected for coincidence. Even lower energy photons in the optical regime (380 - 760 nm), however, are not absorbed by (optically) transparent media, such as diamond. Therefore, a coincidence detection of optical idler and x-ray signal photons seems - in principle - possible. An experimental implementation of such a coincidence detection is presented in the Appendix 8.2.4. It is found that concurrent processes, such as x-ray induced fluorescence, yield count rates, which are by orders of magnitude stronger than expected for the actual idler photon count rates. With (currently) no means to suppress or distinguish fluorescence photons from XPDC-generated idler photons, a coincidence detection of x-ray signal and optical idler, is not achieved.
In order to identify XPDC - irrespective of the idler photon - and thus enable its application for general samples[10], another robust evidence for the nonlinear conversion

[9] Ultra-violet (UV) radiation is distinguished into categories [30], ranging over the following wavelengths: 400 - 315 nm (UV-A), 315 - 280 nm (UV-B) and 280 - 100 nm (UV-C).

[10] which are not transparent for the selected idler energy

needs to be established. As such, the characteristic angular dependence of the (x-ray) signal scattering pattern as a signature for XPDC is employed.

This section presents the experimental implementation of an energy-resolved diffraction setup to obtain the XPDC characteristic scattering pattern.

4.4.1 Setup Geometry

An experimental setup suited to measure the energy-resolved characteristic diffraction pattern of XPDC, needs to address two main objectives. First, the setup needs to provide suitable angular resolution for both the sample angle Ω and the scattering angle 2θ. From the fundamental considerations presented in Section 2.3, an x-ray signal is expected for sample angles of $\Delta\Omega \simeq -20$ mdeg to $\Delta\Omega \simeq +40$ mdeg around the Bragg condition for the fundamental pump energy (Figure 2.6) at an idler energy $E_i = 2$ eV. This requires a sample rotation with sufficient resolution and an accurate positioning of the sample in the diffractometer's center of rotation. The scattering angles are expected in a similar range, from $\Delta 2\theta \simeq -20$ mdeg to $\Delta 2\theta \simeq +40$ mdeg around the Bragg diffracted beam ($2\theta_B$), which set the resolution requirements for the x-ray detection.
The scattering plane is orientated along the horizontal plane, i.e. parallel to the plane of the storage ring.
The second objective is the energetic differentiation between the elastically scattered and the down-converted beam. In the highly non-degenerate case, the energy difference between incident pump field E_p and down-converted photon E_s, is the idler energy E_i, which is on the order of a few electron Volts. Figure 4.14 shows these two main objec-

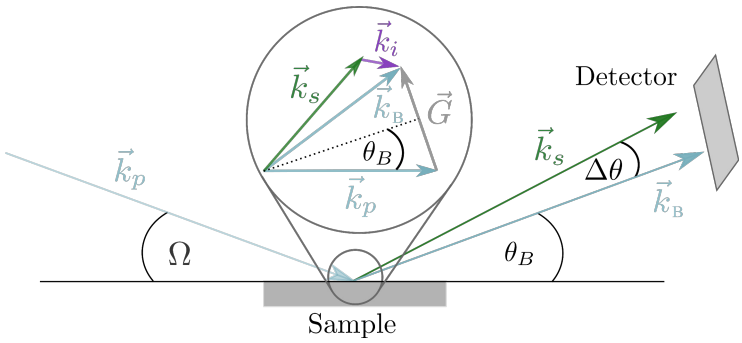

Figure 4.14: The two main experimental objectives for detecting x-ray parametric down-conversion: the small angular deviation $\Delta 2\theta$ from Bragg condition in the scattering plane and the small energy difference of the signal photons from the (elastically scattered) pump $E_s = E_p - E_i$. The figure illustrates these geometrical and energetic constraints for the phase-matching condition, that is shown in the central inset.

tives schematically, emphasizing the very similar photon energies (ω_p, ω_s) with similar scattering wave vectors $\vec{k}_B, \vec{k}_s$.
Experimentally these objectives are met by using a sample rotation with an angular

resolution of 1 mdeg. This is sufficient to precisely scan the sample angle Ω across the phase-matching condition. To enable the angular resolution of the scattered photons, either an APD with an aperture (Section 5.1) or a two dimensional pixel detector (5.2) are used. The achieved resolution in 2θ is 10 mdeg or 2.5 mdeg (per pixel), respectively. To energetically discriminate the elastically scattered radiation at E_p from the down-converted energy E_s, a crystal analyzer is used. A silicon channel-cut crystal (2-bounces) reflects the scattered photons under Bragg condition for a selected energy and within a characteristic bandwidth, here 1.3 eV or 0.3 eV at 10 keV for Si 111 and Si 440, respectively. For the experiment an incident (pump) photon energy of 10 keV or 11 keV was chosen, respectively, at the two different beamlines (ESRF: ID20 and DLS: I16). At these energies the transmission of each beamline is optimized and the flux is maximized. The incident beam is collimated by the beamline's optics to a remaining finite divergence on the order of tens of microrad ($\sim$ 20 µrad) [84]. To control the spatial dimensions of the beam at the sample position an aperture (S_{I_0}) is used (Figure 4.14). It is positioned upstream of the sample and confines the beam size to 0.2×0.2 mm^2 in horizontal and vertical dimension. The undulator's broad emission is monochromatized by a (actively cooled) high heat load Si 111 monochtomator (see Chapter 4.2). The final bandwidth of the incident beam on the sample is $\sim$ 1 eV (FWHM). The spectral width can be reduced further to 0.3 eV (ESRF setup) by applying a second, high resolution monochromator. The respective spectral shapes for these cases are presented in Figure 4.10. Even lower bandwidths are technically achievable, but go in hand with a reduction in flux. Due to the low conversion rate of the XPDC process, a high flux is desirable to acquire reasonable signal strengths.

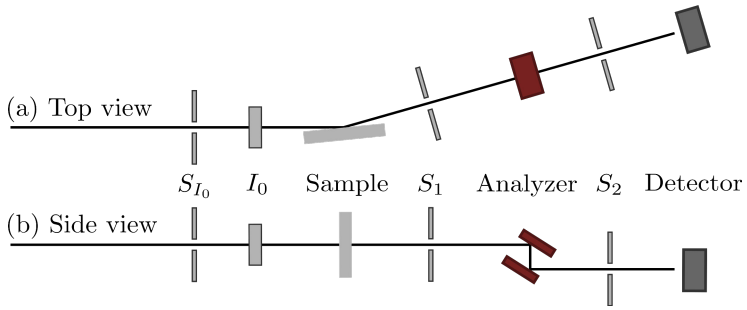

Figure 4.15: Schematic experimental setup used for detecting x-ray parametric down-conversion. Top view (a) on the horizontal scattering plane. Side view (b) emphasizing the vertical offset due to the arrangement of the double-bounce crystal analyzer.

Despite the horizontal polarization of the incident beam [11], the pump photons are scattered in the horizontal plane, due to the geometrical constraints of the diffractometer, which only allows for horizontal scattering.
After interacting with the diamond sample, the elastically and nonlinearly scattered radiation passes through air over the analyzer to the detector (Figure 4.15). On their

[11] ideally demanding for a vertical scattering plane to avoid the reduction of scattered intensity by influence of the polarization factor

path a fraction of the photons interacts with and scatters on air. This diffuse scattering contributes to the detected background (see chapter 5.3). To reduce the amount of detected diffuse air scattering, two additional pairs of apertures are implemented in the setup (S1 and S2). They are positioned in between sample and analyzer and in between analyzer and detector (Figure 4.15).
The single photon counting detector (MAXIPIX: Multichip Area X-ray detector based on a photon-counting PIXel array [85]) has a maximum pixel counter of 11810 counts, corresponding to a dynamic range of 13.5 bits. The detector provides a sensitive area of 14.1×14.1 mm^2, consisting of 256×256 pixels, with 55×55 µm^2 pixel size.The absorption (or quantum) efficiency yields 100% at 8 keV, 68% at 15 keV and 37% at 20 keV.
Experiments are conducted at the experimental stations I16 at Diamond Light Source (DLS) and ID20 at European Synchrotron Radiation Facility (ESRF). Monochromatization was done via a Si double crystal monochromator, yielding an energy resolution of $\Delta E/E = 10^{-4}$ (Si 111). The flux ranged from $1 \cdot 10^{13}$ at I16 [86] to $7 \cdot 10^{13}$ photons/s at ID20 [87]. Beamline optics achieved similar collimation at both experimental end stations with residual divergence of 20 µrad. The beamline configurations vary slightly and differences are emphasized, where they have an impact on the experiment.
A summary of the beamline parameters for end stations at DLS, ESRF and Petra III is given in Table 2 in the Appendix 8.2.4.

4.4.2 Sample Characterization

Diamond is chosen as a sample due to its transparency throughout the visible regime [88, Chapter 2], which makes it a perfect candidate to study x-ray conversion into visible wavelengths and aiming for coincidence detection. The bandgap of diamond is indirect and with 5.45 eV [89] comparably large. Furthermore, diamond exhibits a good crystallographic quality and high radiation damage threshold for optical [90] and x-radiation [91].
The diamond used in the experiments is classified as type IIa. Historically, natural diamonds were classified with respect to their optical properties into types I and II, according to their absorption features at 330 nm and 220 nm, respectively. Synthetic crystals fall into the category of type II, yielding low nitrogen concentration (below 5 ppm). Within these categories further differentiation is done by the amount of nitrogen and boron impurities. Types IIa and IIb are differentiated according their electrical resistivity of -5×10^{14} Ω m for insulators or 100 Ω m or less, for p-type semiconductors, respectively [92].
The diamond sample is a type IIa synthetic crystal, grown by chemical vapor deposition (CVD), of 500 µm thickness (including ± 50 µm tolerance) and 3×3 mm^2 lateral dimension. The crystal is cut along the $\{100\}$ direction, with (110) orientation at the edged (Figure 4.16b). The production via CVD has the advantage that concentrations of impurities and the number of dislocations are very low(< 1 ppb for boron concentration and < 5 ppb for nitrogen) [93]. Both properties influence the measurements: Impurities have a strong impact on the fluorescence properties, especially the concentration of Nitrogen and vacancies within the material. The properties of x-ray induced optical fluorescence are investigated in the context of coincidence detection for de-

termining the optical background contribution. A detailed description is found in the Appendix 8.2.4. Experimentally a miscut between sample surface and crystal lattice

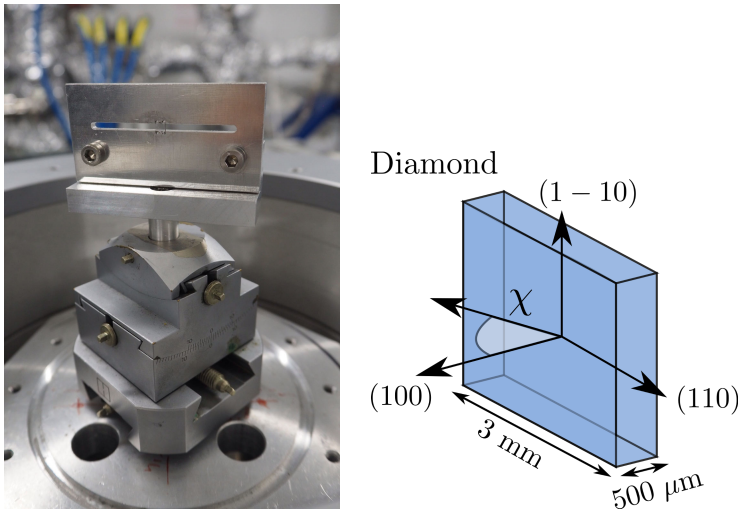

(a) Sample mounting. (b) Orientation of surfaces.

Figure 4.16: Diamond sample used as nonlinear medium to generate x-ray parametric down-conversion. The sample setup at synchrotron beamline: The crystal is positioned on a goniometer head for fine adjustment and rotation (a). The orientation of surfaces of the diamond crystal is shown in (b). The miscut angle (χ) is measured out of diffraction plane (spanned by (100) and (110)) and is determined to $+1$ deg.

plane of $+1$ deg is experimentally determined. This miscut angle χ (Figure 4.16 b) is measured orthogonally to the horizontal scattering plane, being defined parallel to the synchrotron.

The Rocking curve width in 400 orientation is measured to 1.37 mdeg at 11 keV (Figure 4 in Appendix 8.2.4).

Chapter 5

Experimental measurements and data analysis

This chapter describes a series of experimental measurements, covering two different acquisition methods. In a first approach, measurements at selected fixed sample angles, fulfilling the phase-matching condition, are performed. In a second investigation a systematic screening, covering the angular acceptance, is presented. The investigation comprises various energy conversion ratios ω_i/ω_s of idler and signal photons and the influence of the incident and analyzer bandwidths. This was done for different sample orientations in transmission and reflection geometry.

5.1 Measuring Selected Phase-matching Conditions

As presented in Section 3 the down-conversion processes in the x-ray regime was studied experimentally by Eisenberger [16, 17] for the degenerate case and later continued by Danino [29], Yoda [18] and Tamasaku [33, 35] in the non-degenerate case, i.e. for $\omega_i/\omega_s \ll 1$. For the latter, down-converted signal energies of down to $\Delta E = 50$ eV off the incident energy were reported. At the beginning of this thesis no idler energies below 50 eV were reported for the parametric conversion processes in the x-ray regime.
In the presented study, the effect of frequency conversion in the x-ray regime at higher degeneracy is investigated, i.e., for idler fields at visible and infrared wavelengths.
A study to observe the conversion of hard x-rays into visible photons was performed at Diamond Light Source (DLS) at beamline I16[1]. The results of this experimental campaign were summarized in the following report

[1]The experimental approach and conceptual design of this investigation was directed by Prof. Shwartz and his group; the author of this thesis contributed in data acquisition and analysis.

Parametric Down-Conversion of X-Rays into the Optical Regime, *Schori et al.* [94], PRL, 2017

For the experiment, the beamline emission was tuned to 10 keV, close to the undulator's efficiency maximum. The primary monochromator (Si 111) yielded an energy resolution of $\Delta E/E \approx 10^{-4}$, or ~ 1.3 eV (FWHM) and the incident beam was collimated to a reported degree of $<$10 mdeg. The integrated slit system defined the spatial dimensions of the beam to approximately 1×0.5 mm^2 (horizontal x vertical) at the sample position. More specific information on the beamline layout is found elsewhere [86], respectively. To discriminate the idler from background scattering at I16, a three-bounce Si 111 analyzer was used, providing ~ 1.3 eV (FWHM) energy resolution. An avalanche photodiode (APD) from FMB Oxford (Model: APD0001) [95] was used for the detection of the scattered x-ray photons, offering an active area of 5×5 mm^2. The quantum efficiency at 10 keV is 50% and it has a rise time ($10\% - 90\%$) of 2 ns. The diamond sample, which is described in detail in section 4.4.2, is positioned in the center of the goniometer. Sample and detector angles are aligned for the Bragg condition at the 220 orientation (in transmission, i.e., Laue geometry), with $\theta_{Bragg} = 29.4$ deg and $2\theta_{detector} = 58.853$ deg. For both, the sample and the analyzer crystal, two angular scans are performed (Appendix Figure 4), with which the alignment of these crystals is conducted. The peaks of these resulting Rocking curves indicate the Bragg angle for the fundamental pump energy and thereby calibrate the sample and analyzer angle, respectively. For both scans an aluminum filter attenuated the beam intensity by a factor 100 to avoid saturation of the detector. In the Bragg condition $4 \cdot 10^8$ ph/s are detected on the APD with the analyzer optimized for transmission of the fundamental energy. The width of the diamond Rocking curve is measured to 3.9 mdeg (FWHM). This is much larger, than the theoretically calculated Darwin width of $w_h^\theta = 10.87$ µrad (0.62 mdeg). This can be caused by several effects: First, by the crystal quality of the sample. A low quality diamond might include a large fraction of slightly differently orientated crystallites, which would result in a broader Rocking curve. The other reason stems from the influence of the instrument function. This function describes the effect of beamline optics on the recorded scattering pattern and includes broadening effects. The broadening can therefore be caused by both beam divergence (~ 20 µrad) and the bandwidth (1.3 eV). Finite divergence and relatively broad incident spectrum, combined with a non-perfect crystal result in an increased Rocking curve width.
The analyzer is calibrated by a Rocking curve scan. The analyzer is rotated to a reflection of the fundamental energy (10 keV), which is maximal at an angle of 11.4426 deg whereas the nominal Bragg angle for Si 111 at 10 keV is $\theta_{Bragg} = 11.403$ deg. This angular offset (in motor position) of 39.6 mdeg is taken into account for determining the central energy of the analyzer, i.e., the later offset from the central energy ΔE. The central energy E' for which the analyzer is sensitive, is selected by setting the analyzer to the corresponding Bragg angle $\theta_B(E')$. The sample is rotated to phase-matching condition, at a detuning angle $\Delta\Omega$ = 20 mdeg from the Bragg angle position, for diamond in 220 orientation in transmission (Laue) geometry. The phase-matching scans are now conducted in the following manner: The analyzer (Si 111, 3-bounce) is adjusted to select an energy offset equal to the idler energy $\Delta E = E_i = E_p - E_s$, i.e., to $E_i = 2.2$ eV. The detector arm, including analyzer and APD, is scanned along the

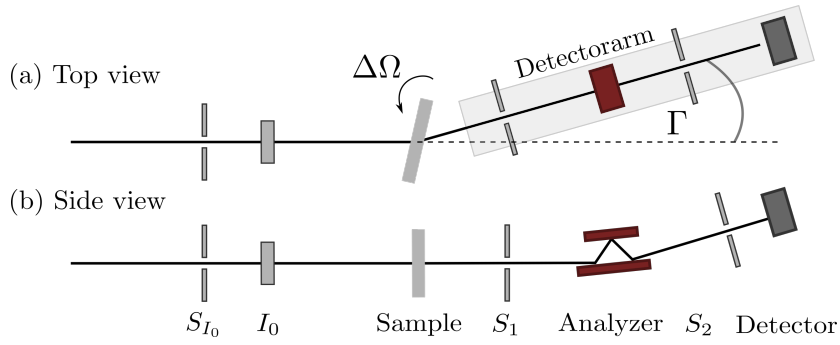

Figure 5.1: Geometry of experimental setup used at Diamond Light Source. The incident beam impinges the diamond crystal in 220 orientation. Two pairs of apertures (S_1 and S_2), the 3-bounce analyzer crystal and the detector are assembled on the detector arm, which can be rotated (Γ) around the sample.

horizontal scattering plane (Γ). The APD, positioned behind the analyzer records the intensity profile, while the detector arm is scanned (Figure 5.1). The slit configuration (Table 5.1), constituted by a pair of horizontal and vertical apertures, up- and downstream of the analyzer, is opened to cover a horizontal angle of 10 mdeg. Detector

	horz. gap / mm	vert. gap / mm	distance d / mm
S_1	0.1	0.5	615
S_2	1.25	2.0	990

Table 5.1: Settings of apertures S_1 and S_2 and distances d from the sample for measurements at the Diamond Light Source, I16 beamline.

angle scans (Γ) are performed for three selected conversion ratios, given by the three energy detunings 2.2 eV, 3.3 eV and 4.4 eV (Figure 5.2). The detector angle scan exhibits three different peaks: a dominant central peak, and two peaks at each side. This observation is made for each analyzer setting, which is indicated by the corresponding energy offset ΔE from the fundamental energy E_p. The main peak increases in intensity for higher analyzer detunings ΔE. This peak was primarily identified as the Bragg reflection of the fundamental pump energy $E_p = 10$ keV. Its intensity is expected to be stronger suppressed for higher analyzer detunings ΔE. However, this behavior is not observed - and the contrary is the case: the intensity of the central peak increases for larger idler energies.
This behavior can be explained by the setup's geometry (Figure 5.3), in which the Si 111 three-bounce analyzer is used for energy discrimination. The analyzer is orientated perpendicular to the horizontal scattering plane such, that the reflection moves out of this plane. Depending on the selected central analyzer's energy $E_s = E_p - \Delta E$, the corresponding angular position results in a different angle along the vertical dimension and

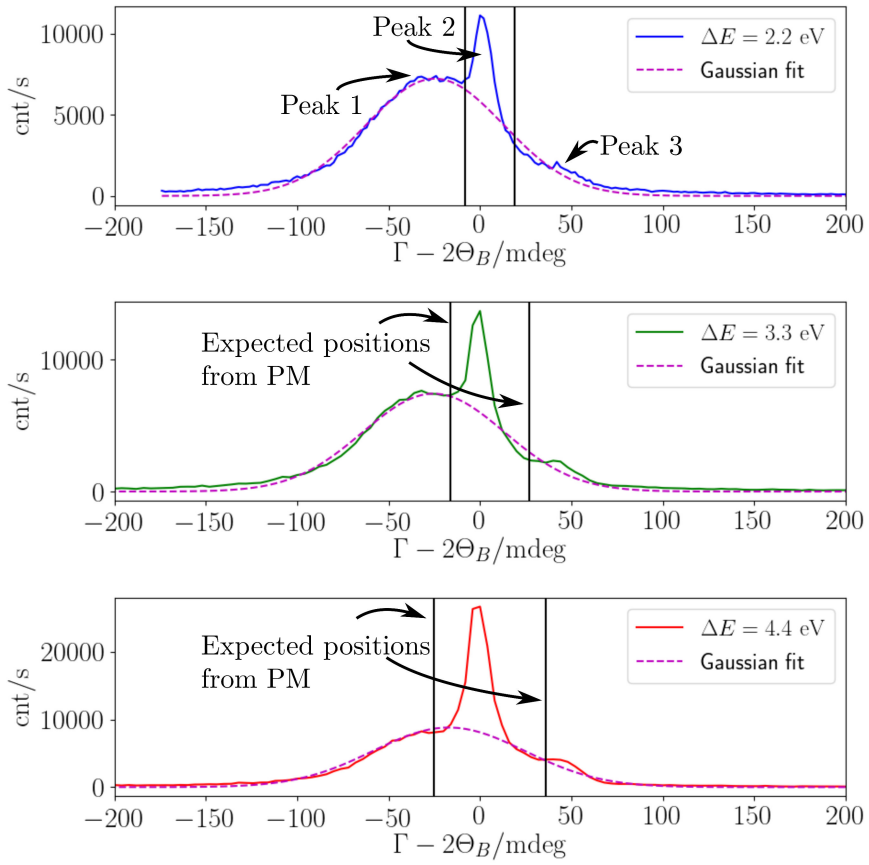

Figure 5.2: Measurements to observe parametric conversion of hard x-rays into visible radiation. The sample crystal is adjusted to fulfill phase-matching ($\Omega - \Omega_B = 21$ mdeg) for the incident 10 keV pump beam. The 3-bounce analyzer is tuned to accept the respective down-converted energy, by 2.2 eV, 3.3 eV and 4.4 eV, respectively. The detector arm is scanned along horizontal scattering plane (Γ). The detected intensity distribution includes three peaks: the narrow, dominant peak referring to the remainder from elastic scattering of the central pump wavelength and the two side peaks referring to elastic scattering from incident spectral distribution. The vertical black lines indicate the scattering angles expected for XPDC signal photons from kinematic phase-matching.

with that a different vertical offset towards the detector. Since the apertures, positioned after the analyzer and in front of the detector, are not re-adjusted for each analyzer angle setting, there is a preferred analyzer angle with highest transmission through these apertures. A deviation form this angle will eventually guide the beam towards to slits,

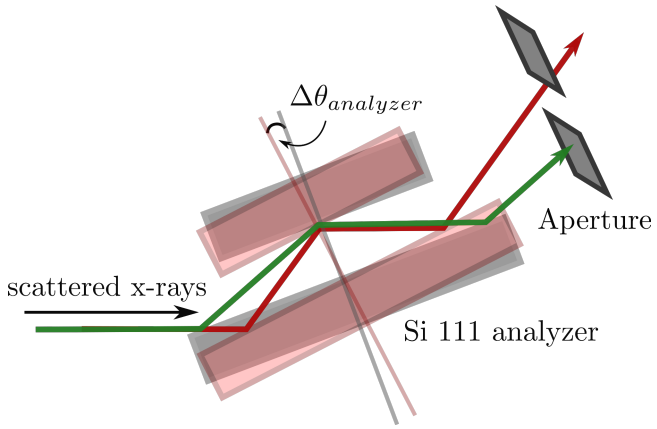

Figure 5.3: Schematics of the Si 111 3-bounce analyzer used for energy discrimination during the measurements at DLS. In the first configuration (gray) the signal beam passes the analyzer and is blocked by the aperture in front of the detector. In the second configuration (red) the signal beam passes the analyzer as well as the consecutive aperture. This behavior is used to explain the increased intensity for the central peaks in Figure 5.2 at higher analyzer detuning angles.

resulting in a cut-off of the beam path and reduced detected signal intensity.
The additional peaks at each side of the central peak appear at the very same positions for the Γ-scans, which are acquired for different phase-matching conditions, namely for $E_i = 2.2$, 3.3 and 4.4 eV, for which the analyzer crystal is tuned. The peak at lower Γ-angles is fitted with a Gaussian profile to determine the peak position more precisely. It is found that the position remains approximately the same at -27 mdeg (Table 5.2) for all three different phase-matching angles of the sample and different analyzer settings. Furthermore, the magnitude of these peaks does not change strongly; it ranges from $3.7 \cdot 10^3$ to $4.0 \cdot 10^3$. The same behavior is observed for the smaller peak at higher scattering angles, which remains at ~ 41 mdeg (without fitting, due to low signal strength).
For further classification of the obtained results two aspects of the setup need to be considered: First, even though the resolution of the motor movement yields 4 mdeg, this does not correspond to the actual resolution with which the scattered radiation is recorded. The obtained spatial resolution is determined by the opening of the slit system, covering a angle of 10 mdeg, yielding a solid angle of $6.4 \cdot 10^{-6}$ sr. Therefore, the presented intensity distribution represents a convolution of motor step width with the covered solid angle provided by the apertures. Second, the Si 111 analyzer provides a minimum resolution of 1.3 eV without further considering divergence effects increasing this value. A distinction between signal photons of ~ 1 eV difference is thereby possible, however suppression of energetically similar (± 2 eV) photons is low. Further detunings from the analyzer's central wavelength by, e.g. 1 eV are suppressed by one order of magnitude only. The broad Si 111 reflex is therefore not well suited for distinguishing between fundamental pump and signal photons of low detuning with no

other additional parameter to distinguish between linear and parametrically converted photons.
Experimentally the side peaks are determined at $\Gamma^{(1)} \simeq -27$ mdeg and $\Gamma^{(3)} \simeq 41$ mdeg. The parameters of the fitted Gaussian curves for the left signal are summarized in Table 5.2. The central peak (Peak 2) remains at $\Gamma^{(2)} = 0$ mdeg. Fitting for the peak 3 was not

ΔE / eV	$\Delta\Gamma^{(1)}_{PM}$ / mdeg	$\Delta\Gamma^{(1)}$ / mdeg	FWHM / mdeg	I_Γ / cnt/s
2.2	-8	-24.67 ± 0.37	88.53 ± 0.75	3619 ± 29
3.3	-16	-25.36 ± 0.42	91.27 ± 0.89	3720 ± 35
4.4	-25	-17.00 ± 0.79	97.87 ± 1.20	4404 ± 57

Table 5.2: Comparison of expected ($\Delta\Gamma^{(1)}_{PM}$) with measured $\Delta\Gamma^{(1)}$ scattering angles for peak 1. The position, intensity I_Γ and FWHM is determined by fitting a Gaussian curve for the three measurements at idler energies E_i of 2.2 eV, 3.3 eV and 4.4 eV.

achieved, due to the low magnitude. The detected side peaks are observed close to the expected scattering angles for XPDC at $2\theta_s^{(1)} - 2\theta_B = -25$ mdeg and $2\theta_s^{(2)} - 2\theta_B = 45$ mdeg for a corresponding idler energy of $E_i = 4.4$ eV ($E_p = 10$ keV).
However, these peaks cannot be identified clearly as originating exclusively from the nonlinear effect. Even though the observed scattering angles lie close to the predicted ones, the peaks are detected at the same angular offsets from Bragg, for all three phase-matching conditions, even though a different angular position of the nonlinear signal is expected from kinematic phase-matching.
The difference between the scattering angles ($2\theta_s$) for the three different conversion ratios with $\Delta E = 2.2,\ 3.3,$ and 4.4 eV, yields each ~ 7 mdeg at $E_p = 10$ keV (Figure 5.4). This difference should be observable with the angular resolution provided by the here presented setup. This angular separation is not observed. Furthermore, the intensity of the side peaks remains constant for the different measured signal energies E_s. For higher idler energies (ΔE) however, better signal to noise ratio is expected, due to the stronger suppression of the fundamental radiation, which is not observed with the experimental data. As a consequence no unequivocal evidence for the nonlinear conversion effect can be presented, within the the scope of the here presented method. Even though these results were successfully published (in a peer reviewed journal) as a proof-of-principle [94], a careful re-evaluation, as presented above, now suggest another interpretation of these results: The recorded signal can be interpreted to originate from elastic effects, stemming from the influence of the incident spectral distribution, the quality of the sample crystal and the bandpass and suppression efficiency of the analyzer. The setup allows thereby, that tails of the incident spectrum are (linearly) scattered at the detuned sample angels $\Delta\Omega$, fulfilling other Bragg conditions. Mosaicity of the sample allows a larger fraction of the incident radiation to be scattered towards the detector. The presumption of a low quality crystal is supported by the Rocking curve measurement, which yields a relatively broad width. Nevertheless, also the properties of the beamline, i.e., divergence and spectral bandwidth, broaden this curve, the broad

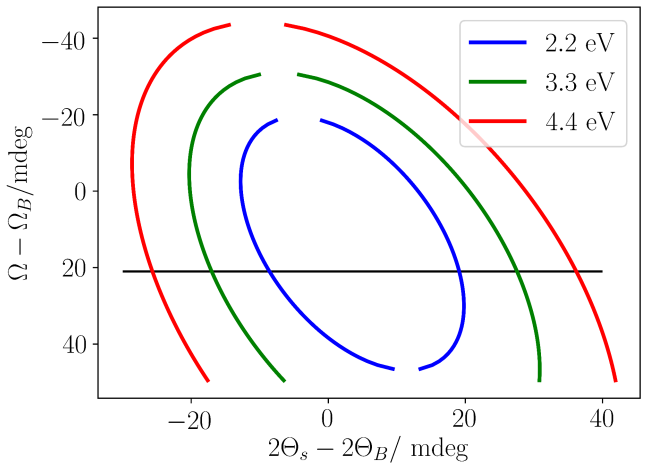

Figure 5.4: Comparison of the solutions of the kinematic phase-matching conditions for the studied orientation 220. The solutions are shown for three different idler energies $E_i = 2.2, 3.3$ and 4.4 eV for a pump energy $E_p = 10$ keV. The sample angle for the presented measurements is set to $\Delta\Omega = 21$ mdeg, indicated by the horizontal line. For a 1.1 eV difference in observed signal energy, equivalent to the idler energy, a difference of ~ 7 mdeg in scattering angle $2\theta_s$ is expected.

Rocking curve width supports the hypothesis, that this setup is not sufficient to resolve the nonlinear scattering from competing elastic background effects. These background effects together with the so called instrumental function, determine the here measured intensity distribution. A detailed discussion of these influences in given in section 5.3. Due to the broad and relatively intense elastic signal it is not possible to measure a clear signature of the x-ray conversion to optical wavelength on the basis of the presented approach.

For unequivocal evidence, either a coincidence detection of x-ray signal and optical idler needs to be achieved, or another clear signature of the XPDC effect established and observed. Competing emission from x-ray induced optical fluorescence (see Appendix 8.2.4) is by orders of magnitude stronger (i.e., several $10^3 - 10^4$ cnts/s) than expected count rates for down-converted optical idler photons. Therefore the optical photons cannot be used for a coincidence measurement, since the origin of the photons (fluorescence or XPDC) can (technically) not be distinguished. Thereby, a coincidence approach cannot be used.

The characteristic scattering signature, constituted by the kinematic phase-matching condition, can be used as evidence and is the basis of the consecutive systematic study.

5.2 Systematic investigation of the parameter space

The previously reported experiment suggests a more detailed and systematic approach including an improved spatial and energetic resolution. For the measuring of the effect the setup needs to be altered with respect to a higher angular resolution. In addition, the methodology itself needs to be altered towards scanning the complete phase-matching condition, rather than selected conditions.
The experimental setup was refined to enable a higher energy resolution, a stronger suppression and an improved angular resolution of the scattered intensity. Beyond that, a careful analysis enables the differentiation of elastic effects from the nonlinear signal. The systematic investigation is structured into the following categories:

- Angular mapping of the phase-matching condition
- Measuring the phase-matching condition for different energy conversion ratios ω_i/ω_s
- Measuring the influence of the incident bandwidth on the scattering pattern
- Investigating different sample orientations

The following data was acquired at ESRF, beamline ID20.

5.2.1 Mapping the Phase-matching condition

In contrast to the previously presented approach, this refined method aims to resolve the full scattering signature of phase-matching condition. These measurements are enabled by introducing a two-dimensional pixel detector to the setup, which mainly improved the angular resolution of the detected scattering pattern, via a pixel size of 55 µm, at a sample distance of $d = 1200$ mm and a resulting angular resolution of 2.5 mdeg per pixels. This providing a significant improvement over the previous 10 mdeg per pixel. A Si 440 analyzer crystal provides an improved energy resolution of 0.3 eV (FWHM) in combination with a stronger suppression of the spectral tails.
The nonlinear signal should be observable within the angular range shown in Figure 5.4. Concurrent elastic effects occur near these phase-matching conditions and need to be distinguished from the nonlinear scattering. These effects are discussed in detail in Section 5.3.
The sample is rotated around the nominal Bragg angle of the pump wavelength $\Omega_B(E_p = 10\ \text{keV})$. Thereby, different phase-matching conditions for various sample angles Ω are fulfilled (Figure 5.5 b: ii and iii). The resulting scattered intensity distribution is energetically filtered by the analyzer, which is tuned to accept the signal energy and detected by the spatially resolving photon counting detector with a dynamic range of 10^4. The setup is first calibrated at Bragg condition with the undetuned analyzer. The scattering angle is determined within one pixel and used as a reference angle ($2\theta_B$). Scattering angles on the detector are determined relative to this position. Apertures are used to suppress background contributions, but they do not determine the setup's resolution as in the setup for the DLS.

Open slits avoid direct scattering from the aperture blades. The influence of the apertures is immanent and their shielding effect is observed on the phase-matching scans (e.g. Figure 5.6 c), where their asymmetric shielding ranges from scattering angles of 0 to 60 mdeg. The apertures were adjusted in this asymmetric manner with the aim to shield the remaining scattering contributions from the fundamental energy, centered around the origin (Figure 5.6 c). Together with other improvements, the slit setting was changed to a symmetric configuration for later measurements.
With the pixel detector, regions of interest can be set according to needs and a range of scattering angles in horizontal and vertical dimension is enabled.
The horizontal intensity distribution is recorded in a single acquisition, instead of scanning the APD as in the previous experiment, thus without the detector movement involved. The conversion ratio ω_i/ω_s in the frequency mixing process is determined by

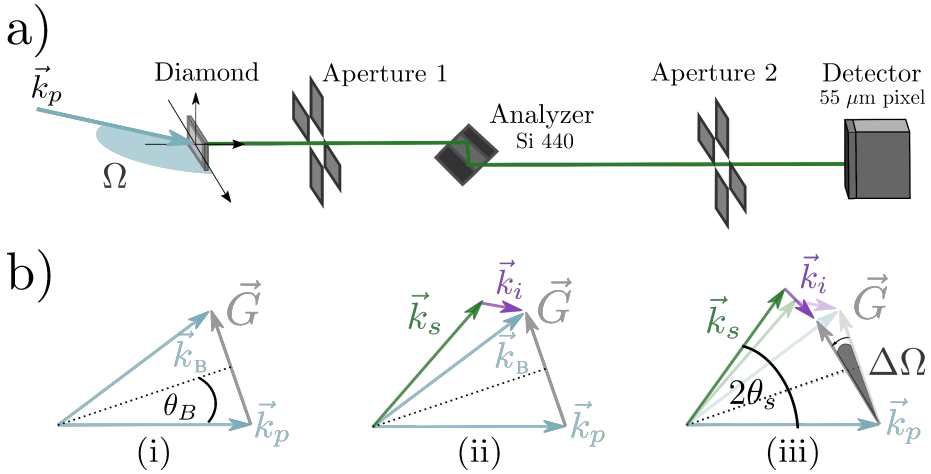

Figure 5.5: Experimental setup (a) and scanning method (b). The phase-matching scans are performed by Rocking the sample crystal and measuring the scattered radiation with a two-dimensional pixel detector. Energy discrimination for a specific signal energy $\hbar\omega_s$ is selected via the channel cut analyzer. Scanning is performed close to Bragg condition (i), where the phase-matching condition is fulfilled (ii) and altered by Rocking the crystal (iii).

the analyzer angle, i.e., the energy setting of the analyzer $E_s = \hbar\omega_s = \hbar\omega_p - \hbar\omega_i$. For the data in Figure 5.6 c the analyzer is detuned to $\Delta E = E_i = \hbar\omega_i = 2.4$ eV (equivalent to an optical idler wavelength $\lambda_{opt} = 564$ nm), and is kept fixed for one scan.
The phase-matching condition itself is scanned by rotating the sample crystal angle Ω over ± 100 mdeg around the Bragg position (Figure 5.5 b (iii)). The typical scanning resolution for $\Delta\Omega$ yields 1 mdeg and is limited by the used diffractometer.
An exemplary data set for these measurements is presented in Figure 5.6 a for the sample in 220 orientation in transmission geometry. The detector images are shown for five selected sample angles Ω_0 to Ω_4, ranging from 0 mdeg to 50 mdeg detuning from nominal Bragg angle Ω_B, respectively.

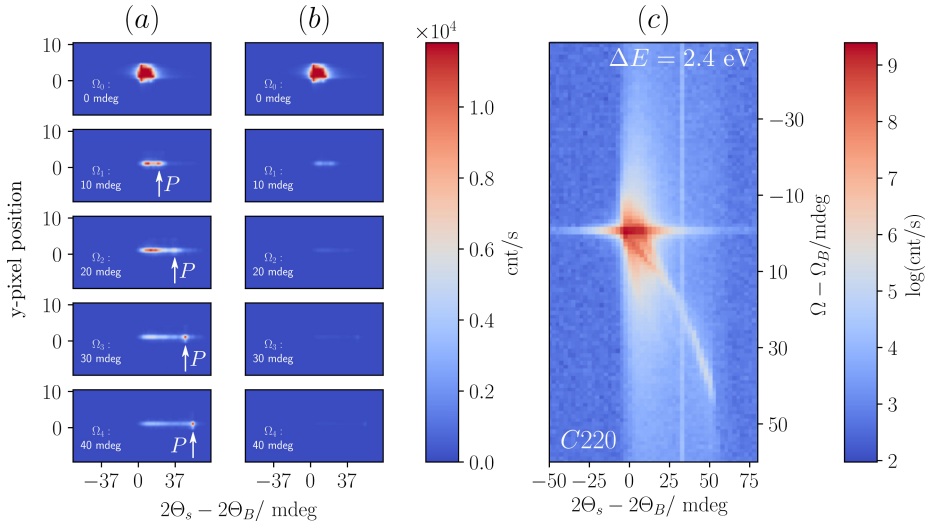

Figure 5.6: Single detector images for selected sample rotations Ω_i shown in (a) and (b) in linear and normalized intensity scaling, respectively. Horizontal intensity profiles (vertically integrated detector images) presented in relative angle from Bragg at pump energy ($E_p = 11$ keV, 1 eV bandwidth) for scan range of sample angle Ω in (c).

The analyzer is detuned from 11 keV by $\Delta E = 2.4$ eV. Still, elastic scattering from the sample shows a strong contribution. In the case of a detuning by 2.4 eV from the 11 keV pump, the fundamental energy is suppressed by four orders of magnitude by the analyzer crystal (Figure 5.11). The apparent increased beam size in Figure 5.6 a for Ω_0 compared to the original beam profile (0.2×0.2 mm^2) is due to saturation of the detector.

The scattered intensity distribution for higher rotation angles $\Delta\Omega_i = 10, 20, 30$ and 40 mdeg detuning from Bragg angle (Figure 5.6 a) shifts towards higher scattering angles. The data is displayed in two different representations: normalized to the highest value within each detector image is indicated (red, Figure 5.6 a). This allows an evaluation of scattered intensity for each individual sample angle Ω. The second representation (Figure 5.6 b) shows the same data, but with a unified logarithmic color scale, to enable a comparison of signal strength. The second representation enables to illustrate how the signal intensity reduces at higher sample angles with regard to Bragg condition ($\Delta\Omega_0 = 0$ mdeg, top image). Nevertheless, a signal is still observable for higher sample angles with constant acquisition times, within the given dynamic range of (estimated) 3.5 orders of magnitude.

Clearly distinguishable are two contributions for the measured intensity distributions (Figure 5.6 a): first, a broadly spread contribution and second, a distinct, well defined peak (labeled with P in Figure 5.6 a). For higher sample angles $\Delta\Omega = 20$, 30 and 40 mdeg off Bragg condition, the observed intensity moves along the horizontal dimension.

To quantify the behavior of the intensity distribution for a sample angle, i.e., Ω, scan,

the data is reduced: The data sets, which are spanned by the sample angle and the horizontal and vertical intensity distribution, are represented in to two dimensions. Therefore, the single detector images are integrated along their vertical axis, preserving the information on horizontal intensity distribution. Figure 5.6 c shows the merged, vertically integrated detector images for one phase-matching scan ($\Delta E = 2.4$ eV). The changing peak positions of the intensity distribution relative to the position of elastically (i.e., Bragg) scattered photons on the detector ($2\theta_{signal} - 2\theta_B$) is well observable. This composite data presents a scan of the phase-matching condition for a selected idler energy E_i. The here introduced phase-matching scans are the basis of the following detailed analysis.

To identify the origin of the detected photons, the measured intensity distribution is compared to the expected scattering angles from the kinematic phase-matching condition, which depend on the experimental parameters:

$$2\theta_{signal} = f(E_p, E_s, O, \Omega), \tag{5.1}$$

as a function of the incident energy E_p, the selected idler energy E_i, the sample crystals orientation O and the incident angle Ω as described in Section 2.3. These parameters and their influence on the phase-matching condition should be studied and analyzed individually by the presented phase-matching scans (Figure 5.6 c).
The peak positions (P in Figure 5.6 a) of the scattered intensity attained from the phase-matching scans (e.g., Figure 5.6) are compared to the solutions for phase-matching. The full width at half maximum of the intensity distribution of the incoming radiation is determined as a second measure. For the case of diamond in the 220 Laue orientation at $E_p = 11$ keV and 1 eV incident bandwidth and an idler energy $E_i = 2.4$ eV the maxima of the measured intensity distribution (blue dot) appear close to the solutions for the kinematic phase-matching (black line in Figure 5.7). The determined widths (FWHM) of the peaks are displayed as horizontal bars. The point $(\Omega - \Omega_B, 2\theta_s) = (0,0)$ corresponds to the Bragg scattering condition for $E_p = 11$ keV. At $\Omega - \Omega_B = 10$ mdeg the condition for Bragg scattering with $E_p - 4$ eV and for $\Omega - \Omega_B = 20$ mdeg with $E_p - 8$ eV is fulfilled. These elastic contributions are close to the expected nonlinear scattering values. A careful analysis of the detected signal is therefore necessary to identify the origin of these features.
In the case of the presented data set for $\Delta E = E_i = 2.4$ eV (Figure 5.7) the measured angular intensity distribution of the signal lies somewhat within the predicted angular range for phase-matching. The analysis is now extended towards other energy conversion ratios ω_i/ω_s.

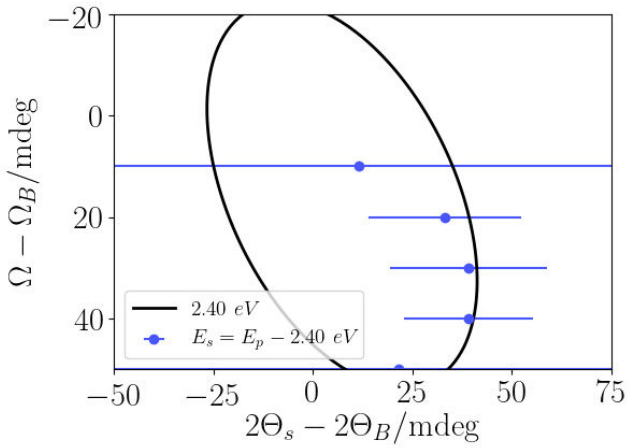

Figure 5.7: Scattering angles of measured intensity distribution for the phase-matching scan at $E_s = E_p - 2.4$ eV. The peak positions of the detected signal distributions are presented by solid dots. The expected signal given by momentum and energy conservation shown by black line.

5.2.2 Conversion ratio ω_i/ω_s

The phase-matching condition is investigated for different conversion ratios, i.e., the ratio of idler and signal energy ω_i and ω_s, respectively.
The energy setting of the analyzer selects a specific signal energy E_s (within the bandwidth of the analyzer, i.e., 0.3 eV), yet allowing different combinations of E_p and E_i, resulting in the same E_s. In general, the conversion of various energy ratios is possible within the limits of the incident pump's bandwidth (1 eV) and divergence (20 µrad).

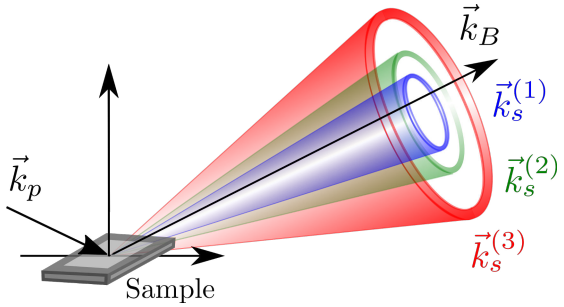

Figure 5.8: Simultaneous emission of signal photons of various energy conversion ratios. The corresponding wave vectors $\vec{k}_s^{(1)}$, $\vec{k}_s^{(2)}$ and $\vec{k}_s^{(3)}$ are emitted in cones around the Bragg scattering direction, given by $\vec{k}_B$. The cones are concentric towards each other. The respective signal photon is selected by the analyzer.

Subsequently, the analyzer is tuned to different energies, ranging from 0.5 eV to 15 eV. Figure 5.9 presents the phase-matching scans for four selected idler energies for the diamond 220 orientation. The measurements are acquired in transmission (Laue) geometry at $E_p = 11$ keV incident energy and with 1.3 eV (FWHM) bandwidth (Si 111 monochromator). The idler energy $E_i = E_p - E_s$ ranges from 2.2 eV ($\lambda = 564$ nm) to

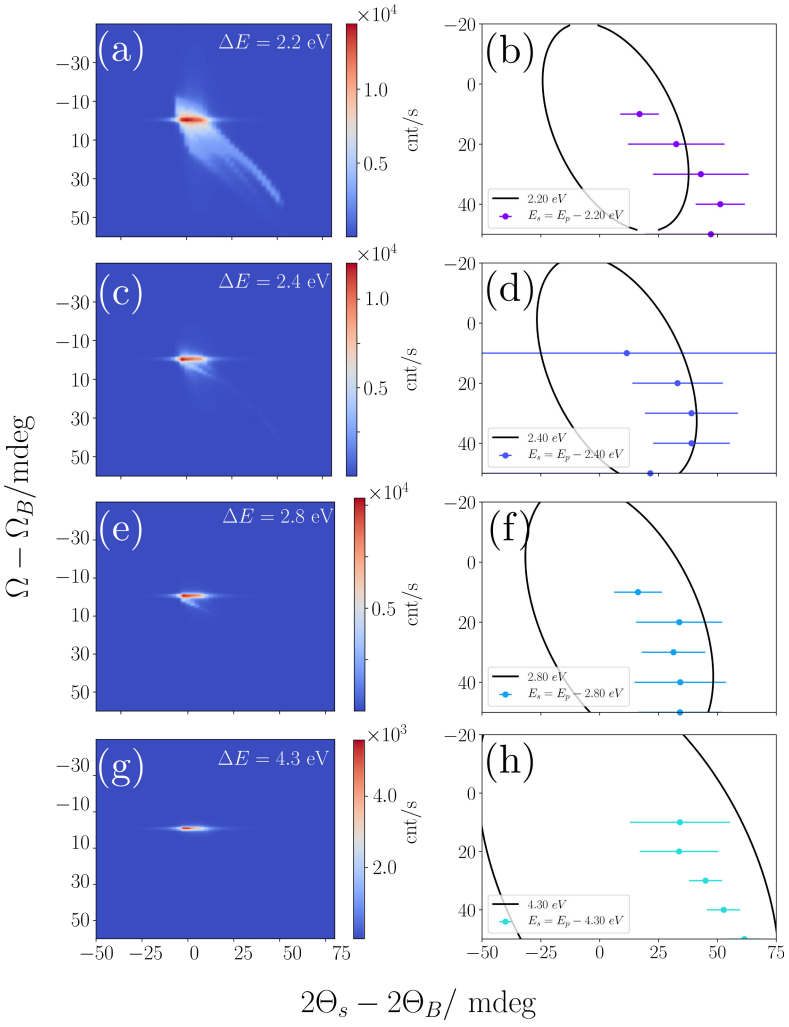

Figure 5.9: Horizontal intensity distributions for phase-matching scan in the 220 orientation (left) in linear scaling. The extracted intensity maxima are compared to the predicted scattering angles from kinematic phase-matching (black line) for XPDC.

4.8 eV (corresponding to $\lambda = 258$ nm), covering wavelengths in the visible regime.

The first data set, for $E_i = 2.2$ eV, yields the most pronounced signal which is rich

of features and which also deviates strongly from the data sets at higher idler energies, where these features are much weaker. The most pronounced feature for this set of scans is constituted by the slightly curved streak. It can also be found for the scans at $E_i = 2.4$ eV and 2.8 eV, though with decreased intensity. The position of the maximum intensity along the horizontal dimension ($2\theta_s - 2\theta_B$) is compared to the predicted scattering angles (Figure 5.9, right side). The FWHM of the measured peaks, indicated by the horizontal bars, show fairly large variations. This is due to the low count rates of only a few photons per pixel at higher rotation angles. For higher idler energies the signal intensity is only slightly larger than the background, yielding even lower statistics for the line width.
Especially for the data sets for $E_i = 2.4$ eV and $E_i = 2.8$ eV the behavior of the scattered intensity aresembles the predicted behavior of the nonlinear effect (Figure 5.9 d and f). However, this degree of agreement is not observed for the data sets of $E_i = 2.2$ eV and $E_i = 4.3$ eV (Figure 5.9 b and h). The intensity peaks are only observed for scattering angles above the Bragg angle, which is caused by the asymmetric shielding of the apertures. These limit the setup's field of view as observed in the logarithmic representation (Figure 5.10).
The most striking observation, however, is that the features themselves remain unchanged in position for different signal energies. This observation is even more clearly

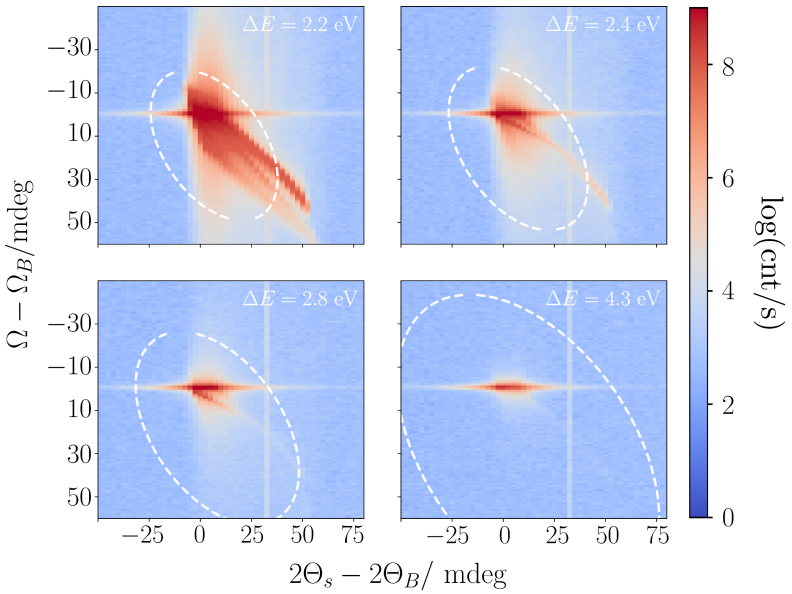

Figure 5.10: Horizontal intensity distributions for phase-matching scan in the 220 orientation (left) in logarithmic scaling. The kinematic phase-matching condition is indicated as white dashed line.

pronounced in a logarithmic representation of the data (Figure 5.10). Comparison with the predicted PDC scattering angles (white, dashed line) form the kinematic phase-matching condition reveal, that the data does not resemble expected phase-matching

angles[2].
The above considerations suggest that the measured data cannot be attributed to the nonlinear effect of x-ray parametric conversion. On the contrary, the observed behavior of the intensity distribution can be explained on the basis on elastic scattering effects (Section 5.3). Since the most dominant additional scattering contribution originate from the spectral distribution of the incident beam, monochromatization of the pump beam and the analyzer characteristics are investigated in more detail.

5.2.3 Spectral bandwidths

For the experimental setup two main contributions of energetic bandwidth can be distinguished. The incident photons have an intrinsic energetic bandwidth, which is defined by the beamline monochromator transmission. The second bandwidth is introduced by the channel-cut analyzer. The influence of both elements on the detected signal is discussed in the following paragraphs.

Monochromator bandwidth Most dominant is the influence of the wide spectral range of the incident beam. Despite initial monochromatization of the broad undulator radiation by the Si 111 double-bounce channel-cut crystal, the incident beam is still polychromatic. Yielding an energy resolution of $\Delta E/E = 10^{-4}$, or a full width by half maximum of ~ 1 eV, it is in addition defined by the tails of the spectral intensity distribution (Figure 5.11). The suppression of the tails is essentially determined by the number of reflexes used. For example, photons 2 eV off the fundamental wavelength are only suppressed by four orders of magnitude. Since x-ray parametric down-conversion is expected to have conversion rates ranging between 10^{-14} to 10^{-9}, elastic scattering effects of this magnitude are not negligible as background. Indeed, compatible features are known from high resolution diffractometry [96, 97], where their origins have been identified in the effect of specific components of the experimental setup. In addition, the efficiencies of these studied features resemble the count rates observed in the here discussed results.

In a further extension of the analysis, a higher resolution is achieved by an additional Si 311 channel-cut crystal. The convoluted (Si 111 and Si 311) resulting spectrum[3] (Figure 5.11) indicates two aspects: first, a reduced bandwidth to approximately 0.3 eV and second, a stronger and steeper suppression of the spectral tails.
Especially the tails of this incident spectrum need to be considered for the experimental setup, since energies from the incident spectrum might fulfill the Bragg condition for various phase-matching angles.
At this point, the main difference in the experimental approaches for parametric conversion processes in the all-optical and the x-ray regime shall be emphasized. In the all optical case, fully monochromatic radiation is available by optical lasers. Wavelengths with variations of only $\Delta\lambda \approx 0.0004$ nm are achievable [98], which are close to the

[2]The vertical line corresponds to a broken pixel. It is left uncorrected as guide for the eye.

[3]The respective spectral distributions were calculated with the ray tracing program OASYS [78]. An undulator spectrum of 30 eV width at a fundamental energy of $E_f = 10$ keV was simulated together with the respective monochromator configurations.

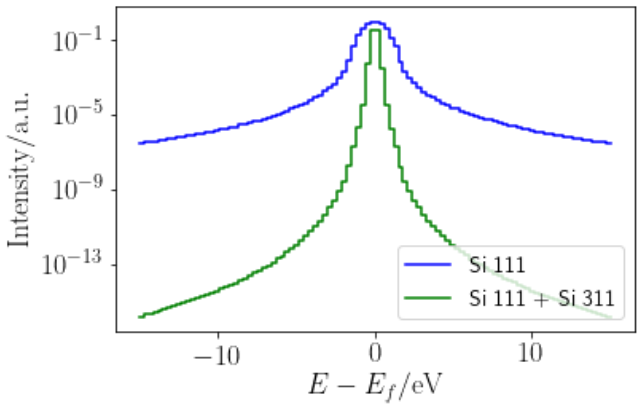

Figure 5.11: Spectral distribution of two different monochromator configurations: The blue curve shows the distribution of a undulator spectrum at fundamental energy $E_f =$ 10 keV after a Si 111 double-bounce monochromator. The green curve shows the spectral distribution for an additional Si 311 double-bounce monochromator. Details on calculation see text.

limitations predicted by the Heisenberg uncertainty principle ($\Delta E \cdot \Delta t \geq \hbar$). But even with classical HeNe-lasers, spectral purities of $\Delta\lambda = 0.002$ nm are achieved [99]. This degree of monochromacity is unprecedented in the x-ray regime. Thus, these limitations with regards to studying parametric conversion of x-ray into visible photons, need to take into account.

The influence of the incident monochromator and analyzer bandwidths on the predicted scattering angles is calculated on the basis of the kinematic phase-matching condition. The monochromator (Si 111) provides a bandwidth (FWHM) of $\sim$ 1 eV. Therefore, scattering angles are calculated for $E_p \pm 0.5$ eV (Figure 5.12, blue line). Their acceptance range for the sample angle Ω is similar in width, though slightly shifted towards lower angles for higher pump energies and vice versa.
It has to be emphasized that for these conditions the x-ray signal energy E_s was fixed, and by variation of the incident energy E_p a variation of the idler is allowed. This is a valid approach, since in the presented systematic study of the phase-matching condition, the idler photon was not taken into account, and solely the x-ray signal photon was acquired.

Analyzer bandwidth In addition to the bandwidth of the incident energy, the energy resolution of the analyzer crystal is investigated. The Si 440 channel-cut analyzer has a bandwidth of 0.3 eV. This energetic window is indicated by the red and green dashed curves in Figure 5.12 under consideration of the same incident photon energy E_p, but under variation of the x-ray signal energy E_s within a range of ± 0.15 eV, resembling

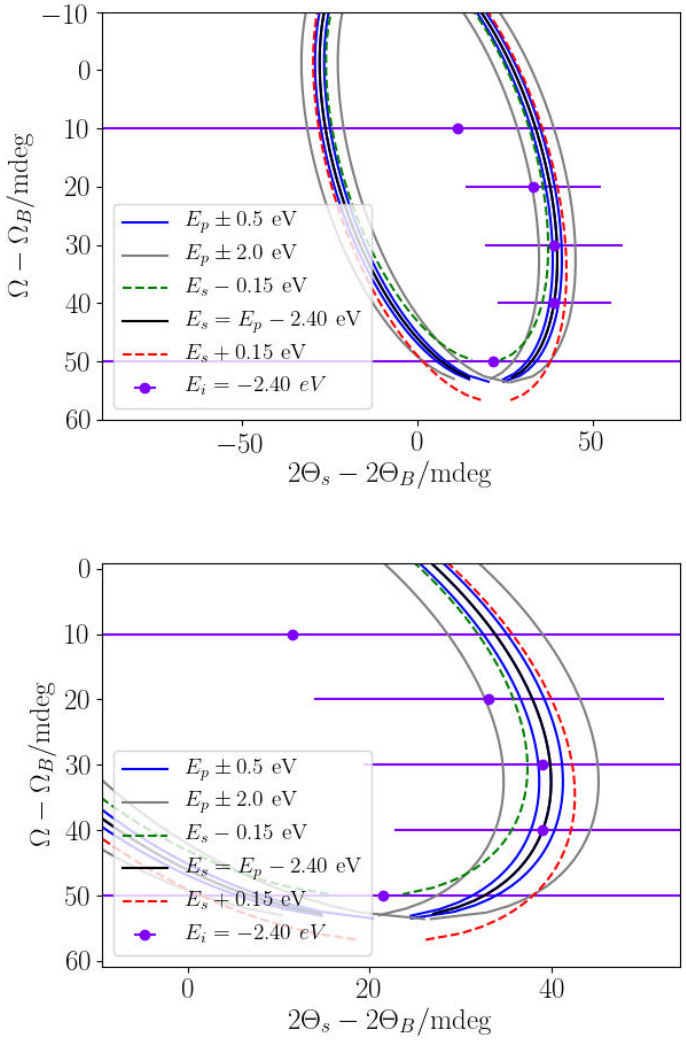

Figure 5.12: Influence of monochromator (gray) and analyzer (green, red) bandwidth on expected angles for phase-matching condition. The variations for scattering angles stemming from the variation of the incident bandwidth $E_p \pm 0.5$ eV are negligible. The lower image shows the behavior in greater detail.

the analyzer's pass width. In general this acceptance width also holds for the other incident energies but is not shown to facilitate readability.

By this comparison it becomes apparent, that the spread inside the cone of concurrently generated signal wavelengths is broader than the spread induced by the incident

bandwidth.
Due to the considerations made in the previous section, the suppression of energies a few eV detuned from the pump energy, are not entirely suppressed. Therefore, the behavior of incident photons by ± 2 eV off the fundamental energy is considered (Figure 5.12, gray line). The variation of ± 2 eV yields a spread in scattering angles of ± 5 mdeg, which is detectable with the setup's resolution.

The reduction of the incident bandwidth yields higher precision of the measurements and especially a strong suppression of the spectral tails is inevitable for a unequivocal evidence of the nonlinear effect. Otherwise, elastic contributions are of comparable scattering magnitude as the nonlinear signal.
In principle the lowest achievable spectral bandwidth for the incident beam should be aimed for. Still, the reduced bandwidth leads to a reduction of flux. Therefore a compromise between resolution and signal count rate needs to be found.
As an additional step to increase the setup's resolving power, a high resolution monochromator (Si 311) in addition to the main Si 111 monochromator is used. The comparison of the achieved resolution is presented in the following section.

5.2.4 Bandwidth Study

The influence of the incident bandwidth is investigated experimentally (ESRF, ID20). Phase-matching scans are performed with the main monochromator (Si 111) only. Beyond that, data is available for a higher resolution of the incident bandwidth, enabled by the usage of an additional high resolution monochromator (Si 311).
The calculated spectral distributions for the usage of a double-bounce Si 111, or the combination with a Si 311, respectively, are presented in Figure 5.11.
For the experimental comparison two data sets were acquired. One at $E_p = 10$ keV and ~ 1 eV bandwidth (Si 111) and another at the smaller bandwidth of 0.3 eV (Si 111 and Si 311). The data sets are measured for the diamond 400 orientation in reflection (Bragg) geometry. Again, various conversion ratios ω_i/ω_s are investigated, ranging form 1.3 eV up to 4.0 eV. Exposure times are set to 1 s and 5 s, for the high and low bandwidth case, respectively and the data is corrected for varying exposure times.
In the direct comparison, the effect of the high resolution monochromator becomes visible. In general the additional monochromator reduces the count rates by approximately two orders of magnitude. The incident total flux however, differs only by a factor of 3 for the two monochromator configurations. Due to the suppression of the spectral tails the overall count rate is reduced.
Moreover, the spatial extension of the observed streaks is not strongly changed.
Even though the same sample is used for both data sets, and measurements were performed back to back, the introduction of the additional monochromator changed the observed scattering pattern. This can be explained by a beam offset in height, which the additional monochromator (Si 311) introduces. The beam impinges the sample on another position, where other crystal defects and conditions of strain and stress are present. Thus changing the orientation of the streaks slightly. Again the scattering features are in general unchanged in position and decrease in intensity with higher energy detuning ΔE of the analyzer. The specific isolated feature for the 3.1 eV and 4.0 eV

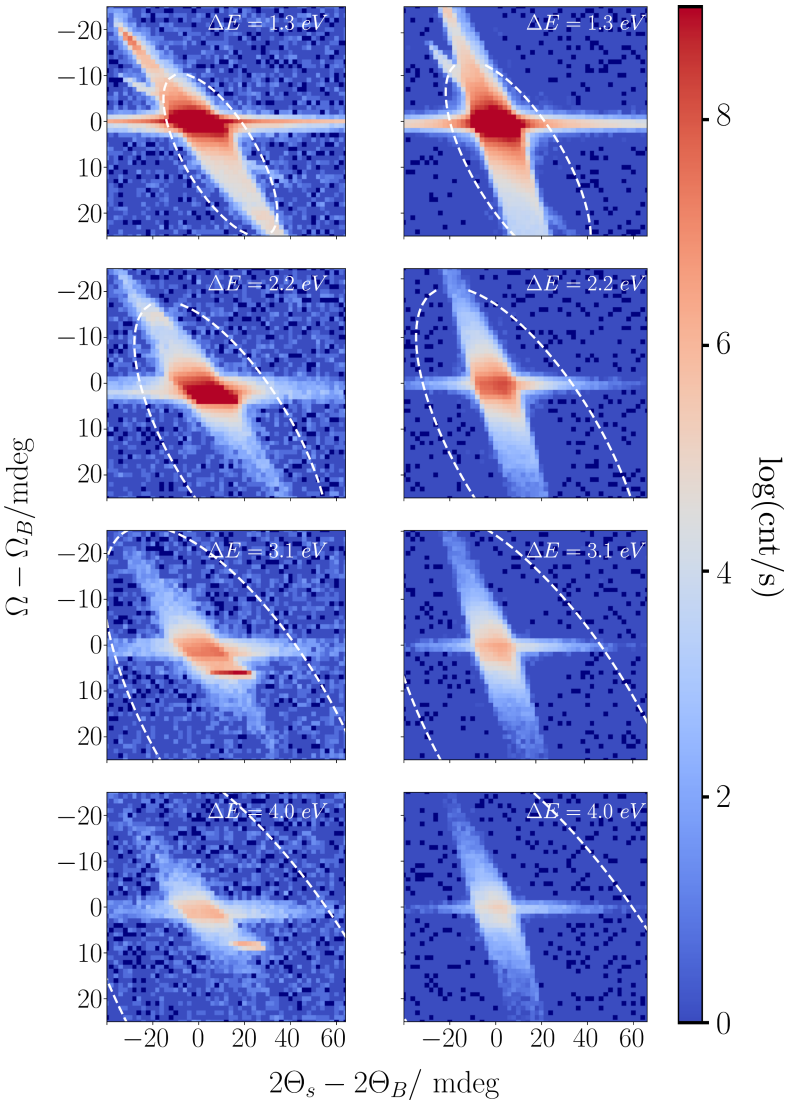

Figure 5.13: Bandwidth study: scattering signal of phase-matching scans observed with 1.3 eV incident bandwidth on the left column and 0.3 eV bandwidth on the right column. The influence of the instrumental function, i.e., horizontal and vertical streaks (details see text), are clearly visible.

energy detunings at 1 eV bandwidths, can be attributed to a grain structure within the crystal.

The phase-matching scans acquired with the reduced incident bandwidth do not exhibit the expected scattering signature for the parametric conversion process. From the

previous study on the 220 orientation with 1 eV incident bandwidth, it was concluded that a reduced bandwidth is beneficial. The reduction in bandwidth indeed yields a suppression of concurrent elastic features, however, the resolution is not sufficient to resolve the low efficiency nonlinear effect.

5.2.5 Sample Orientation

From the geometric phase-matching condition it is apparent that the reciprocal lattice vector $\vec{G}$ determines the nonlinear scattering process. In the same manner as elastic diffraction, the nonlinear scattering is observable at different lattice planes, since the physical scattering process itself is similar. The lattice planes are selected by the respective orientation of the sample crystal.
Even though it is not expected that x-ray parametric down-conversion has a preferred scattering geometry, which might affect its efficiency in a dominant manner, i.e., beyond an order of magnitude, various orientations - transmission and reflection likewise - are investigated.
For diamond as nonlinear material, the orientations 220, 400, 111 and 311 are investigated. In the transmission geometry for 220 and in reflection for the others.
The geometry of the atomic configuration and density for a specific lattice plane is depicted in Figure 5.14 for the different configurations.
The diamond sample crystal is cut along the 100 plane and the surface normal is aligned to be within the scattering plane. The additional properties of the used samples are discussed in Appendix 8.2.4.

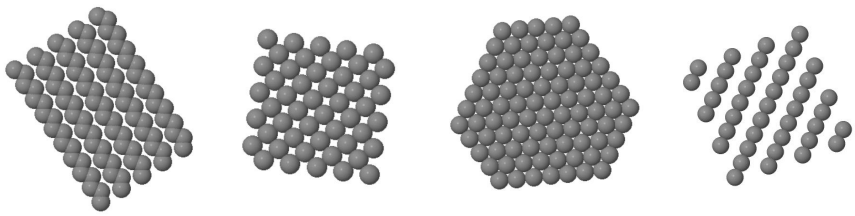

(a) 220 (b) 400 (c) 111 (d) 311

Figure 5.14: Arrangements of atoms within the lattice plane of a diamond crystal for orientations: 220 (a), 400 (b), 111 (c) and 311 (d), respectively. All orientations are used for systematic scans of the phase-matching condition. The 220 in transmission, the 400, 111 and 311 in reflection geometry. Figures taken from [100].

The previously discussed results for the 220 orientation are acquired at 11 keV and ~ 1 eV incident bandwidth. The following detailed study and analysis of the different orientations is performed at the ID20, ESRF at 10 keV incident energy. In addition to the main monochromator (Si 111) a high resolution monochromator (Si 311) is used, yielding a bandwidth of 0.3 eV.
The studied orientations are summarized in Table 5.3. In addition, the beam parameters, measured idler energies and the theoretical Darwin widths are given. The scat-

O	E_p / keV	ΔE_p /eV	E_i /eV	w_h^θ / µrad	w_h^θ /mdeg
220	11	1	2.2 - 4.3	5.7720	0.3307
220	10	1	1.3 - 4.3	5.6176	0.3218
400	10	1, 0.3	1.3 - 4.0	0.2435	0.0139
111	10	0.3	1.3 - 5.4	15.164	0.8688
311	10	0.3	1.3 - 5.0	2.0732	0.1187

Table 5.3: Summary of studied orientations O for parametric conversion of x-rays into visible photons: Incident beam energy E_p, bandwidth ΔE_p, investigated idler energies E_i, and the Darwin widths w_h^θ given in µrad and mdeg.

tering angles generated by the nonlinear effect of parametric conversion are calculated on the basis of the kinematic phase-matching condition, for all orientations. The influence of the selected orientation, i.e., the reciprocal lattice vector $\vec{G}$, is dominant (Figure 5.16). The predicted scattering pattern varies in its elliptical shape, angular acceptance and alignment along horizontal scattering dimension. Even though the scattering pattern for the different orientations does not change drastically, few variations can be observed. The highest angular acceptance, i.e., achieving phase-matching for a broad range of incident angles Ω, is provided by the 111 orientation, with approximately 150 mdeg. On the other hand, the same orientation is confined strongest in the horizontal scattering dimension $2\theta_s - 2\theta_B$ with approximately 60 mdeg. The other orientations exhibit a slightly broader extension along the horizontal dimension. In addition, the eccentricity of the ellipses varies: it is lowest for the 111 orientation and most pronounced for the 400 case.
Notably, the fundamental symmetry of the ellipses is preserved for different idler energy settings, ranging from 1.0 to 4.0 eV (Figure 5.15).
For a more rigorous comparison, the calculated scattering angles at a fixed idler energy $E_i = \Delta E$ are presented for different orientations (Figure 5.16). Even though the phase-matching scans are not directly performed for a fixed idler setting in different orientations, this representation shwos that the direct influence of the orientation on the phase-matching process becomes apparent.
In the following paragraphs a detailed overview of the performed phase-matching scans is presented. The experimental data is compared to the calculated scattering angles.

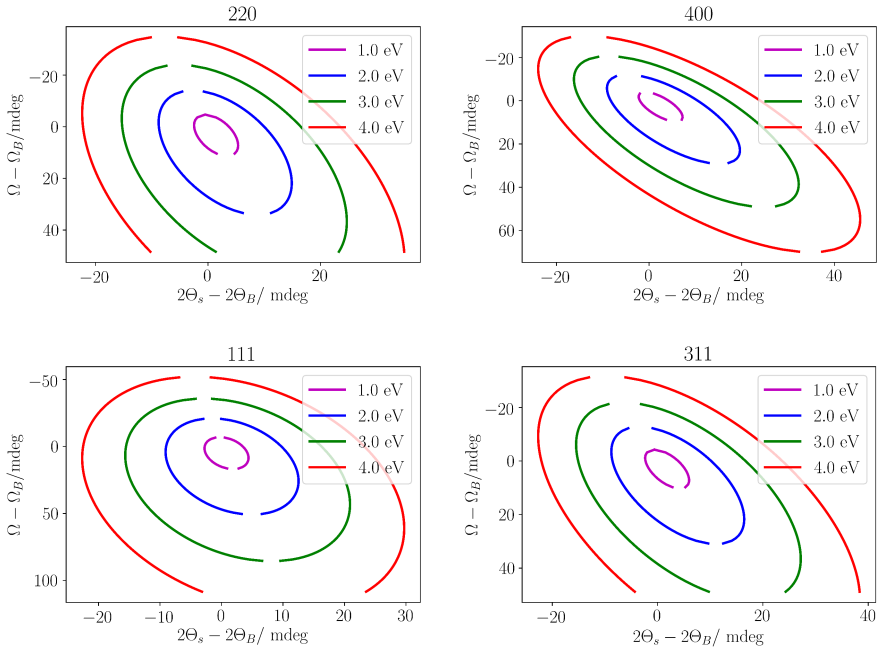

Figure 5.15: Comparison of the solutions of the kinematic phase-matching conditions for the four different idler energies, ranging from $E_i = 1.0$ eV to 4.0 eV for orientations 220, 400, 111 and 311, respectively. The calculations are preformed for an incident energy of $E_p = 10$ keV.

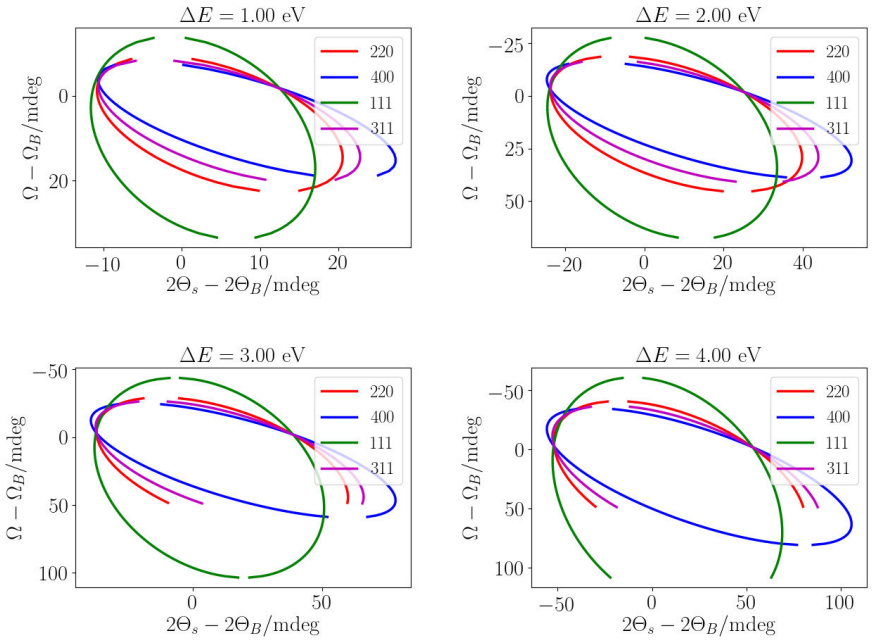

Figure 5.16: Comparison of the solutions of the kinematic phase-matching conditions for the four different studied orientations 220, 400, 111 and 311, respectively. The solutions are shown for four different idler energies $E_i = 1, 2, 3$ and 4 eV for a pump energy $E_p = 10$ keV.

Diamond 220 Orientation For the diamond 220 orientation, phase-matching scans for idler energies, ranging from $E_i = 1.0$ eV to $E_i = 8.1$ eV, are acquired (Figure 5.17). Data sets are acquired for an incident energy of $E_p = 11$ keV and a bandwidth of 1 eV and for the high resolution case with $E_p = 10$ keV and a reduced bandwidth of 0.3 eV. The scattering pattern is directly compared to the predicted angles, similar to the previous discussion, but in addition idler energies above the bandgap energy ($E_{gap} = 5.47$ eV [101] for Diamond) are shown. The horizontal scattering angle is indicated on the horizontal axis, whereas the sample angle Ω is given on the vertical axis. No clear signature for the nonlinear effect is found. Again, all observed features become less

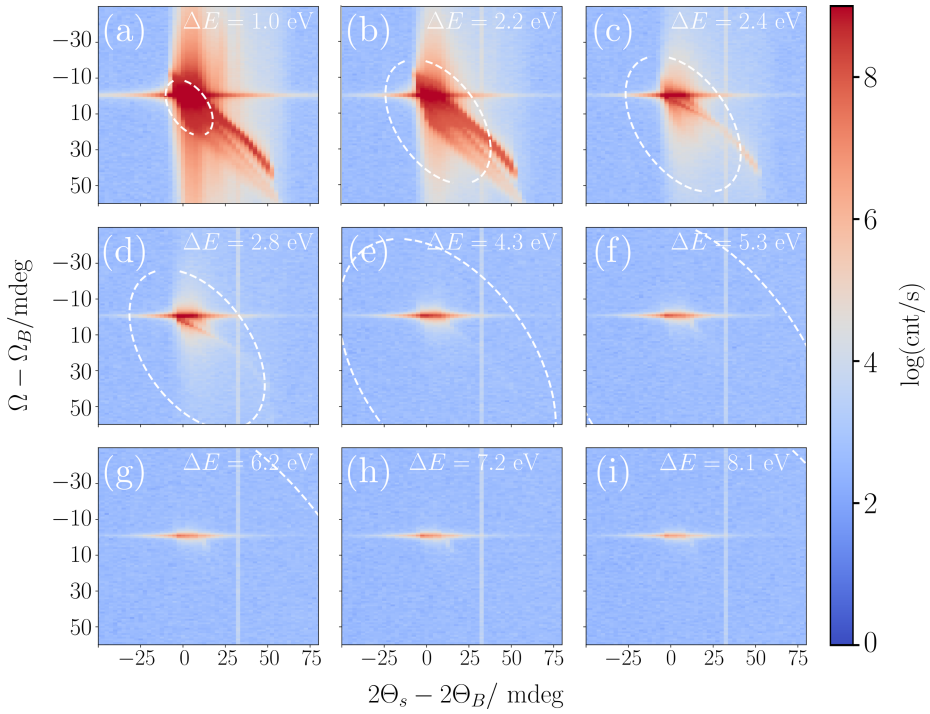

Figure 5.17: Phase-matching scans for the 220 orientation: Horizontally resolved intensity distributions of phase-matching scans. All scans presented in a logarithmic scale and acquired with $E_p = 11$ keV and a bandwidth of 1 eV.

dominant with increased idler energy setting, i.e., higher detuning of the analyzer. For analyzer settings beyond the band gap energy E_{gap} only the remainder of the Bragg scattering at fundamental energy is observed (vertical feature). This feature originates from the fundamental energy being reflected at Bragg condition ($\Omega = \Omega_B$). Despite reduced transmission of spectral tails by the analyzer, the incident spectrum is so intense, that these spectral components still leak through the analyzer.
The same systematic approach is repeated for the higher resolution configuration at $E_p = 10$ keV and reduced bandwidth of 0.3 eV (Figure 5.18). The advantage of the decreased bandwidth together with the stronger suppression of the spectral tails becomes

apparent for low idler energies specifically.
The higher the analyzer's detuning from fundamental energy, the less impact the spectral tails impose on the acquired scattering pattern (Figure 5.18 lowest row). The dif-

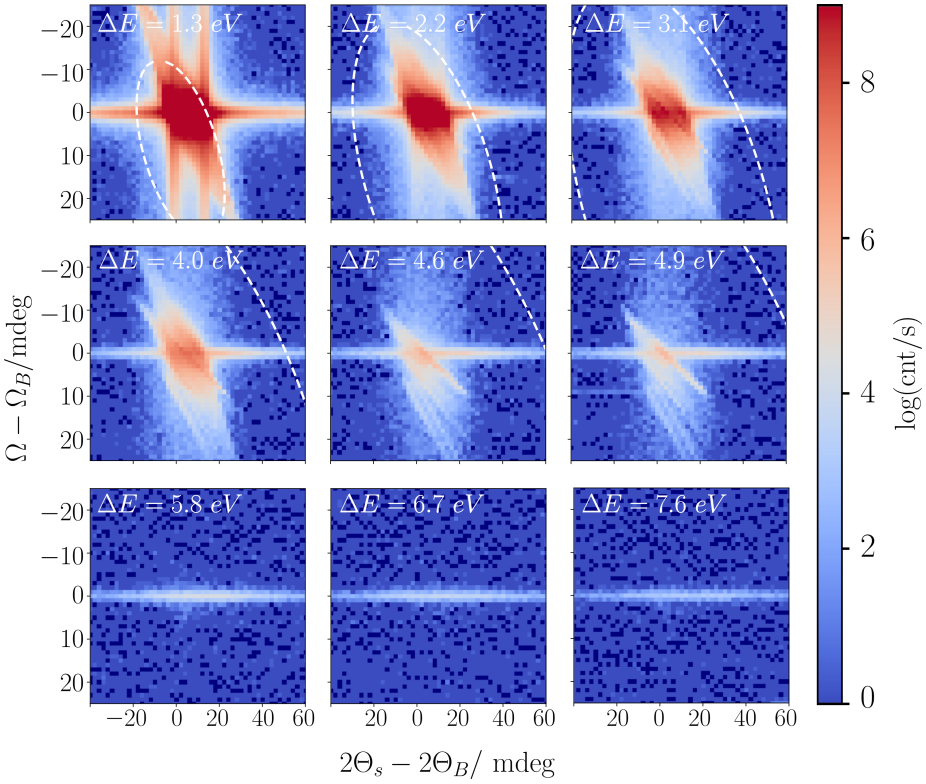

Figure 5.18: Phase-matching scans for the 220 orientation with high resolution setup: Horizontally resolved intensity distributions of phase-matching scans presented in a logarithmic scale and acquired with $E_p = 10$ keV and a bandwidth of 0.3 eV.

ference between scattering angles for down-converted photons is acquired for $E_p = 11$ keV or $E_p = 10$ keV is small (Figure 5.19). The maximum deviation in predicted angles is found for sample detunings at $\Delta\Omega = 30$ mdeg. With scattering angles of $2\Delta\theta_s(E_p = 11\text{keV}) = 21.5$ mdeg and $2\Delta\theta_s(E_p = 10\text{keV}) = 24.5$ for the respective pump energies, the deviation results in $\Delta = 3$ mdeg (15%), which is in the order of one to two pixels (1 px being equivalent to 2.5 mdeg resolution ($E_p = 11$ keV) or 1 px equivalent to 2.0 mdeg ($E_p = 10$ keV)).

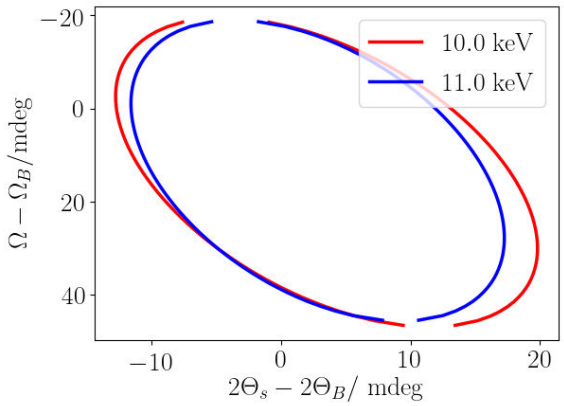

Figure 5.19: Comparison of relative scattering angles for phase-matching at the 220 orientation at 11 keV and 10 keV, respectively. The difference in expected signal angles depends on the sample angle Ω and shows a maximum difference of 15% at 30 mdeg sample detuning from Bragg.

Diamond 400 Orientation While the 220 orientation is measured in transmission the 400 reflection is measured in reflection. The 400 orientation is symmetric, since the scattering plane is parallel to the surface plane of 100. The obtained results are presented in Figure 5.20. The horizontal intensity distributions of the phase-matching scans are shown for nine selected energy splitting ratios, specified by ΔE, which corresponds to the energy of the idler photon E_i.
The count rates are given in linear scale and the dynamical range in these images is low. In contrast to the 220 orientation, where scattering angles for very specific idler energies ($E_i = 2.2$ and 2.4 eV) almost resemble the scattering angles predicted for the nonlinear effect, a similar signature is not observed for the 400 orientation. Again, scattering features are observed, which are attributed to originate from elastic effects stemming from bandwidth and divergence properties of the incident beam (see Chapter 5.3). The measured intensity distribution remains static in position, decreasing rapidly in intensity on the shape's edges for a higher analyzer detuning. A variation in horizontal angles, as expected from the phase-matching condition, is not observed. Again, for higher idler energies the overall measured intensity decreases, as it would be expected from linear effects, originating from the incident spectrum.
In addition, a similar approach as for the 220 orientation is attempted: The horizontal scattering angle for the acquired intensity at different sample angles Ω is determined and compared to the predicted angles (Figure 5.22). For the case of $E_i = 2.2$ eV the determined intensity deviates by 20 mdeg from the expected phase-matching values.
For the other idler energy settings the scattering angles do not match the predicted angles. Based on these observations the obtained signal is, again, identified as elastic scattering and not as the result of parametric down-conversion.

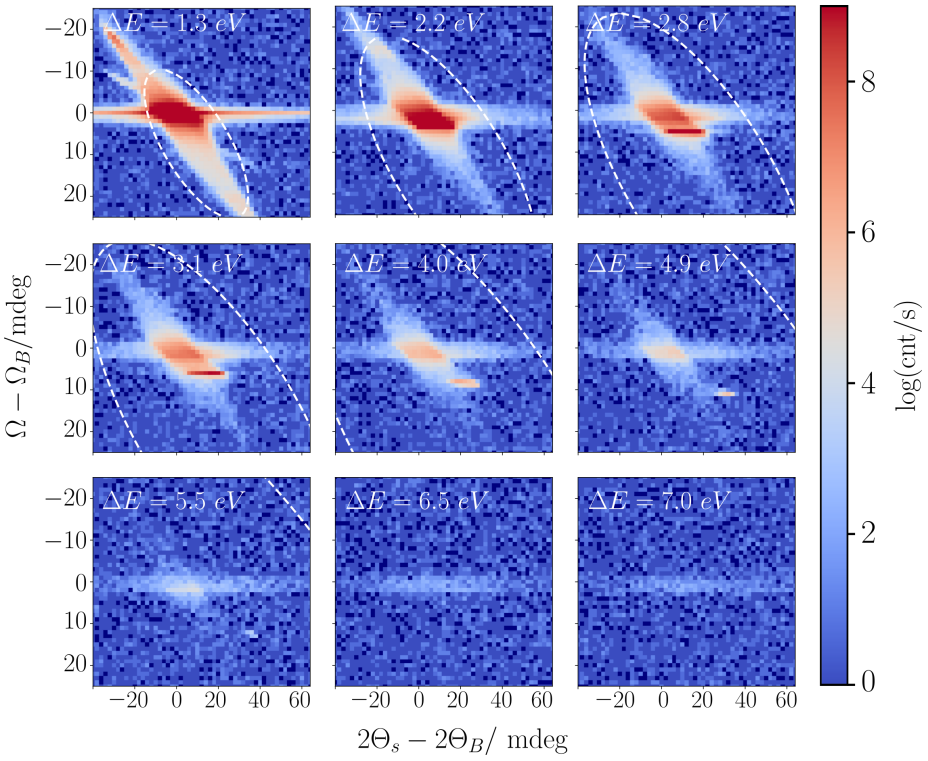

Figure 5.20: Phase-matching scans for the 400 orientation with high resolution setup: Horizontally resolved intensity distributions of phase-matching scans presented in a logarithmic scale and acquired with $E_p = 10$ keV and a bandwidth of 1.0 eV.

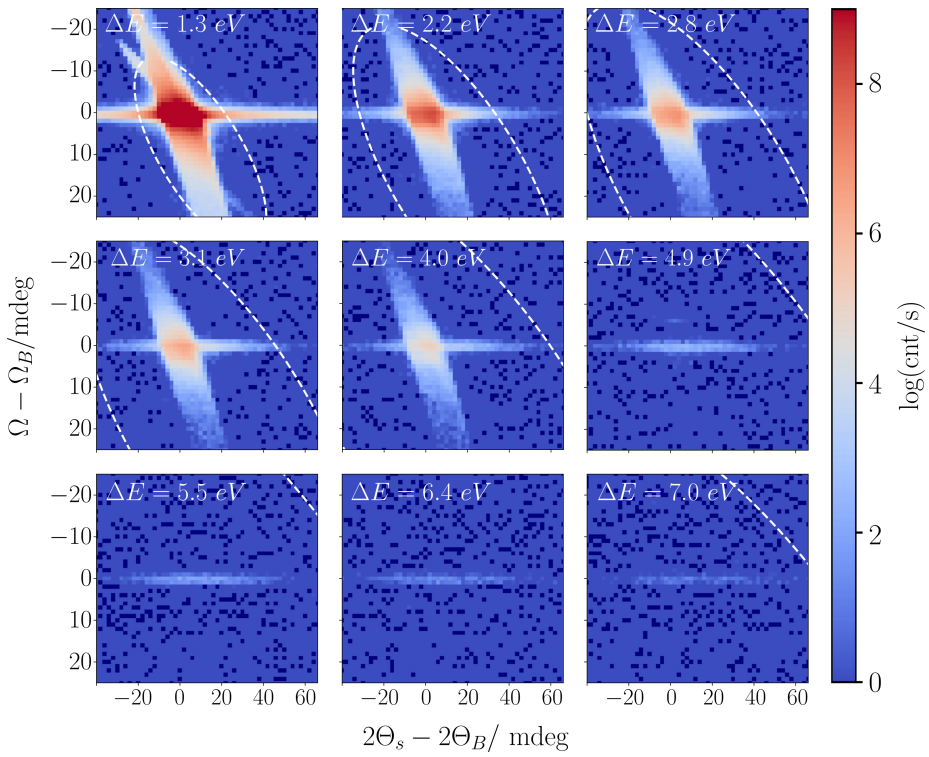

Figure 5.21: Phase-matching scans for the 400 orientation with large bandwidth: Horizontally resolved intensity distributions of phase-matching scans presented in a logarithmic scale and acquired with $E_p = 10$ keV and a bandwidth of 0.3 eV.

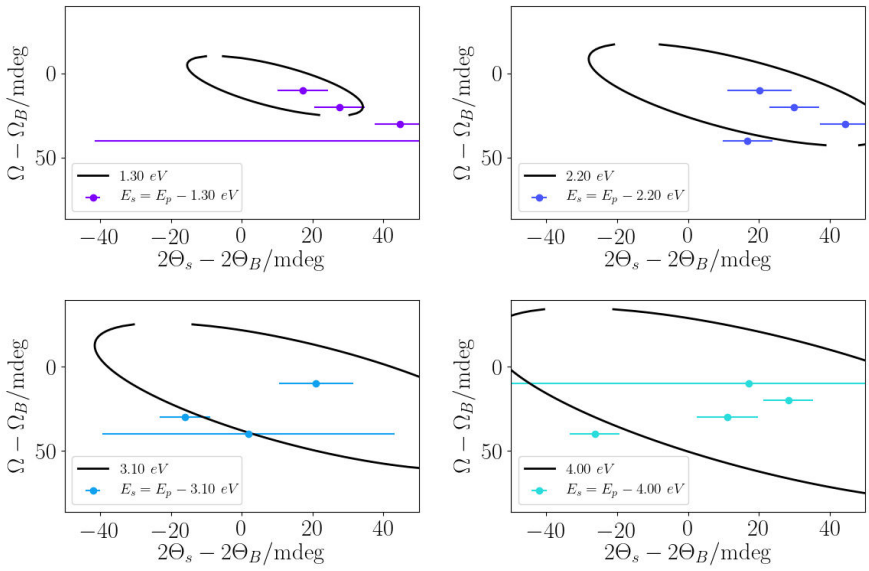

Figure 5.22: Comparison of angular peak positions $2\theta_s$ of scattered intensity distribution with geometrical phase-matching condition for the diamond 400 orientation. Data set acquired with an incident energy $E_p = 10$ keV and 1 eV bandwidth.

Diamond 111 Orientation The 111 orientation of diamond is measured in reflection (Bragg) geometry at $E_p = 10$ keV and with 0.3 eV bandwidth. The detected horizontal

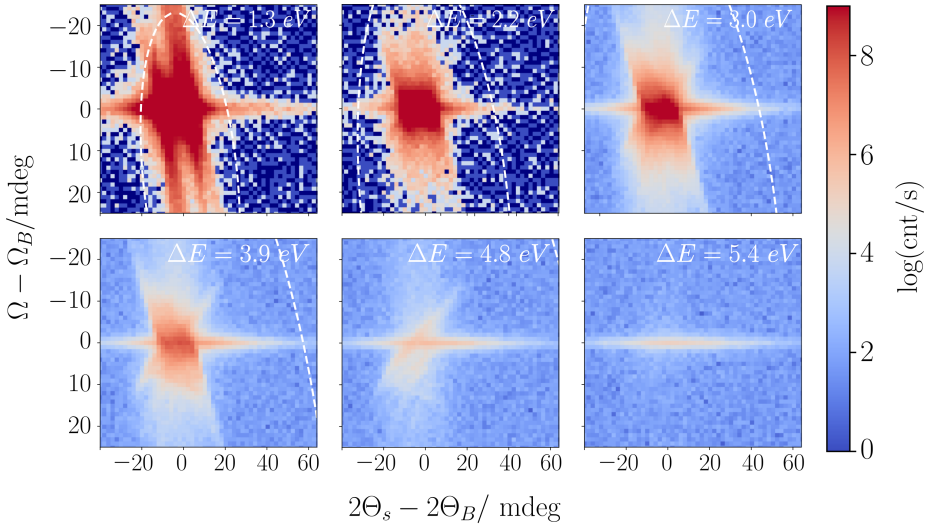

Figure 5.23: Phase-matching scans for the 111 orientation with high resolution setup: Horizontally resolved intensity distributions of phase-matching scans presented in a logarithmic scale and acquired with $E_p = 10$ keV and a bandwidth of 0.3 eV.

intensity distributions for the phase-matching scans are acquired for idler energies E_i below the band gap $E_{gap} \simeq 5.4$ eV (Figure 5.23), and are presented in logarithmic scale. For the lowest idler energy $E_i = 1.3$ eV there are dominant streaks observable along the sample angle's dimension. They remain for the successive, higher idler energies but are reduced in intensity, as it is expected from elastic effects stemming from the incident spectrum. For $\Delta E = 4.8$ eV the observed scattering feature changes its direction. Since the analyzer selects different energies for transmission, only energies with this specific energy offset (within the bandwidth of the analyzer) scatter in the other direction.

Diamond 311 Orientation For completeness, also the data sets acquired at the 311 orientation of diamond are presented (Figure 5.24). They are measured in reflection (Bragg) geometry. The incident beam energy is 10 keV and a bandwidth of 0.3 eV is used. The horizontal intensity distribution for the phase-matching scans is acquired for idler energies E_i below the band gap $E_{gap} \simeq 5.4$ eV. Similar observations as in the previously discussed cases are made. The observed features are different in shape and spread. However, they share the two aspects of not resembling the phase-matching angles and decreasing in intensity. The latter observation is not as distinct as for the other orientations, yet still observable.
Finally, the investigation of peak intensities is repeated for the 311 orientation (Figure 5.25). Measured and predicted scattering angles are clearly not in agreement.
Again, a nonlinear signal cannot be identified, since the clear scattering signature of parametric down-conversion is not observed.

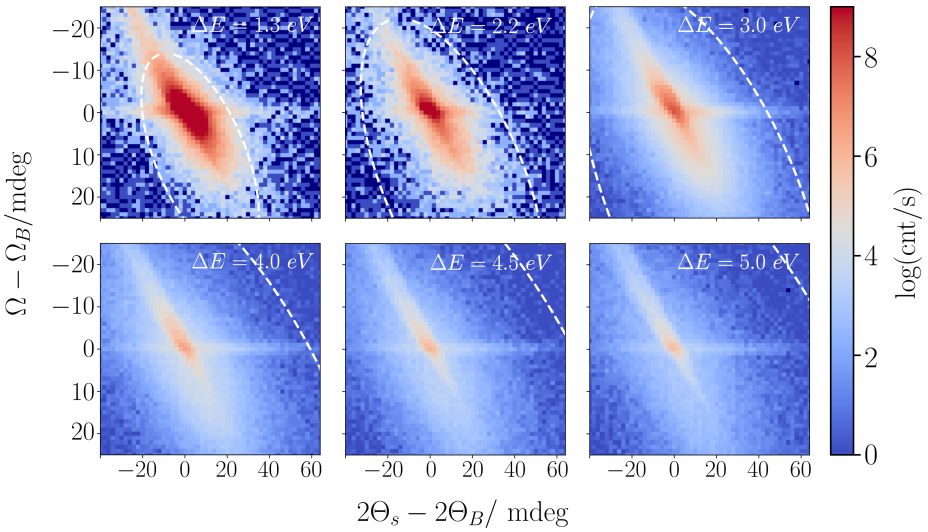

Figure 5.24: Phase-matching scans for the 311 orientation with high resolution setup: Horizontally resolved intensity distributions of phase-matching scans presented in a logarithmic scale and acquired with $E_p = 10$ keV and a bandwidth of 0.3 eV.

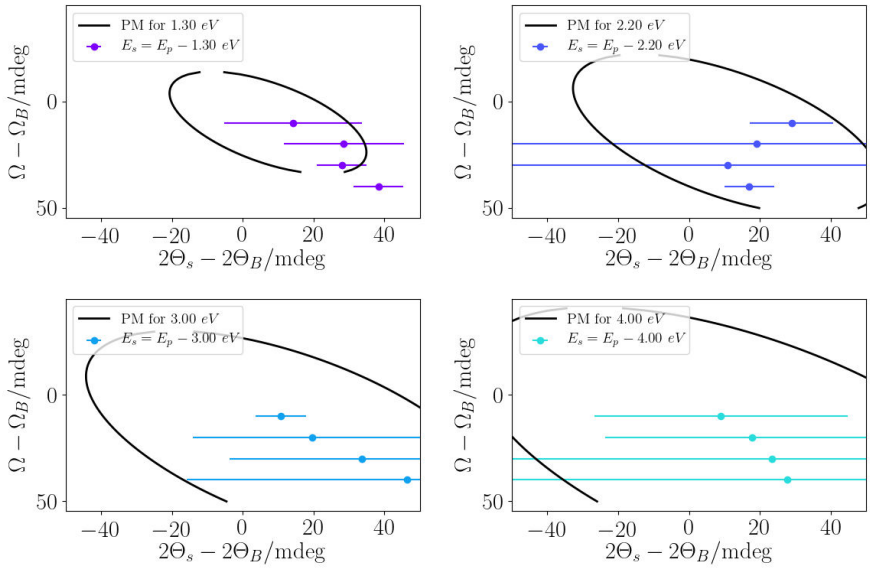

Figure 5.25: Comparison of angular peak position $2\theta_s$ of scattered intensity distribution with geometrical phase-matching condition for the diamond 311 orientation. Data set acquired with an incident energy $E_p = 10$ keV and 0.3 eV bandwidth.

5.2.6 Direct comparison of DLS and ESRF data sets

The systematic mapping of the phase-matching condition furthermore enables a direct comparison of the phase-matching scans with the previously measured data at selected sample angles from the DLS campaign.
The scattering angles of the intensity maxima from the DLS measurements (Figure 5.2) are included as reference data in the data set with the same experimental parameters obtained in the systematic study (Figure 5.17). Comparable data sets are limited to an amount of the three measurements presented in section 5.1, for one specific sample angle $\Omega - \Omega_B = 21$ mdeg at three different signal energies $E_s = E_p - \Delta E$, with $\Delta E =$ 2.2, 3.3 and 4.4 eV, respectively, which are compared to the three closest idler energies in the ESRF data set. It is worth noting, that the acquisition methods of these two data

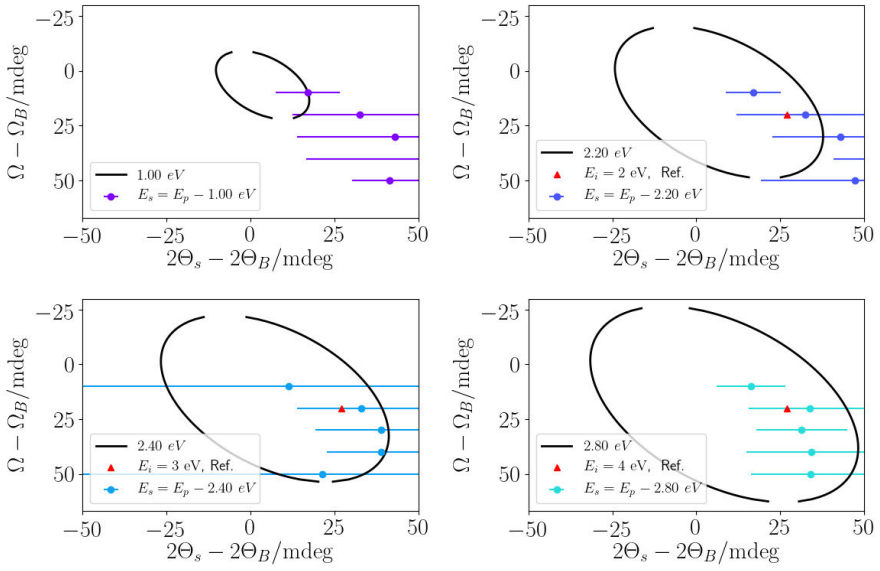

Figure 5.26: Phase-matching scans for Diamond in 220 orientation at a pump energy $E_p = 11$ keV from the systematic study (colored dots), including the FWHM of the horizontal distribution and the expected signal, given by momentum and energy conservation (black line). The four presented data sets are acquired for different settings of the analyzer: 2.2, 2.4, 2.8 and 4.3 eV energy offset. The Bragg angle Ω_B refers to the fundamental energy of 11 keV. The positions of the signal obtained in the previous DLS study are included for comparison (red triangles).

sets differ decisively: in the DLS experiment the detector arm with the APD is rotated around the sample with the slit setting and solid angle of the detector determining the setup's resolution, whereas in the latter setup the intensity distribution is acquired in a single exposure of the pixel detector, where the resolution (2.5 mdeg / pixel) is determined by pixel size and distance to the sample.

Alternatively, a lineout at the sample angle $\Omega - \Omega_B = 21$ mdeg can be taken from the systematic phase-matching scans (see Figure 5.6 c) and directly compared to the APD signal from the DLS campaign (Figure 5.27) for a selected idler energy of $E_i = 2.2$ eV. The systematic study is set in context with results from previous studies [94]. The

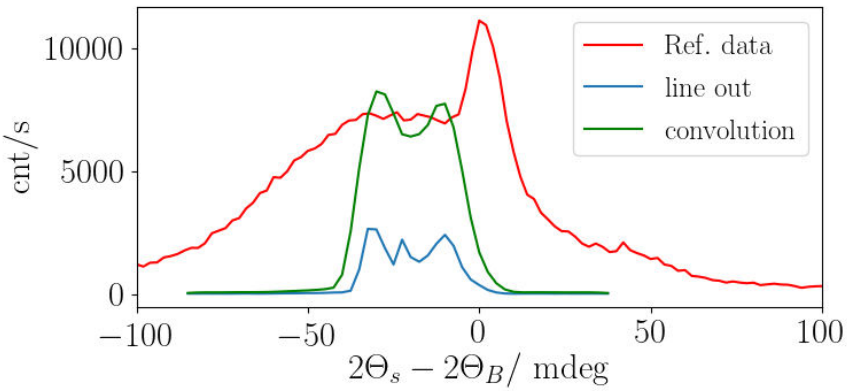

Figure 5.27: Comparison of data acquired for single selected phase-matching angles (DLS, red) with scans from the systematic study (ESRF, blue) for Diamond in 220 orientation and a corresponding idler energy of $E_i = 2.2$ eV for the same sample detuning of $\Delta\Omega = 21$ mdeg. The influence of the higher resolution analyzer is apparent by the strong reduction of the main peak, stemming from elastic scattering of the fundamental radiation. Accounting for differences in incident flux and angular resolution, an accordingly convoluted version of the ESRF data (green) is shown for clearer comparison with the previous data set.

respective line-out is shown in Figure 5.27 (blue) together with the reference data (red) of [94].
In order to allow for a better comparison of the data, a third line (green) is plotted, which compensates for the differences in the resolution of the respective setups: accounting for the lower angular resolution achieved in Ref. [94], where a spatially non-resolving detector (avalanche photo diode) was framed by limiting apertures. These apertures determines the width (10 mdeg) of the window function with which the ESRF-data is convoluted. Furthermore, a normalization for the difference in flux is included. Most notable is the difference in energy discrimination, which is the reason for the broader shape and the additional central peak: for the reference data a Si 111 (3-bounce) analyzer was used, providing a bandwidth of ~ 1.3 eV. In contrast, a Si 440 analyzer, yielding a bandwidth of 0.3 eV, is employed for the systematic study. Qualitatively this is reflected in the fact that the scattering peak of the fundamental energy (i.e., the strong central peak) is completely suppressed (Figure 5.27) by the Si 440 analyzer. With these corrections applied, the resultant signal is found to be largely consistent with the reference data both in position and count rates.

In conclusion, the results from the previous study (DLS) can be reproduced by applying similar experimental conditions. However, the refined setup allows to identify the detected intensity as elastic scattering, which in conclusion identifies the data sets of previous reports [94,102–104] as to originate from elastic scattering as well. A detailed discussions of the implications on published reports is presented in Section 6.

5.3 Background Contributions

To date, no unequivocal evidence is found for x-ray parametric conversion into visible photons. Yet, the experimental setup and scanning method was continuously improved towards higher spatial and spectral resolution, which enabled the resolution of many additional features. These can be attributed to concurrent scattering effects, a discussion of which is presented in the following paragraphs in greater detail. In addition other background effects originating from crystal imperfections and air scattering contributions are discussed.

5.3.1 Elastic Effects and the Instrumental Function

The improved sensitivity provided by the experimental setup enables the resolution of concurrent linear effects, which are predominantly determining the scattering pattern. These linear effects originate from beam parameters, which deviate from ideal conditions (e.g., divergence, bandwidth, etc.) or minor detunings of the sample and the beam optics (i.e., monochoromator and analyzer). These features are well known in high-resolution X-ray diffraction (HRXRD) and are fundamentally described by the *Instrumental Function* [96]. The instrumental function describes the scattering pattern expected by the behavior of the diffraction setup under real conditions including divergence, spectral bandwidths, finite detection resolution while rotating the sample (Ω-scan).
On the basis of instrumental function considerations, several features, which are observed for the experimental data, are identified.

Instrumental Function

As described in Chapter 2 a scattering experiment is used to extract physical information on the sample system from the scattering process itself. This can be achieved by correlating an intensity signal to a photon energy, a detector position, an angle or other observables. The detected signal incorporates information on the specimen, but beyond that it is influenced by the characteristic parameters of the incident x-ray beam: the source characteristics, constituted by flux, bandwidth, beam dimensions on the sample and divergence. In addition, all elements included in the beam path modify these parameters. These optics, such as monochromators, apertures, collimators, mirrors, etc., which are used to confine the beam, introduce deviations from ideal parameters. Their characteristics must be included in the analysis.
In some cases, it is possible to measure the effect of the instrumental function experimentally via Rocking curve scans of a well characterized reference sample. Since the

effect of x-ray parametric down-conversion is intrinsically concurrent with elastic effects, however, this calibration cannot be used to separate the two.
Therefore, additional theoretical knowledge of the instrumental function has to be used to distinguish the contribution of optical components of the experimental setup from the nonlinear signal.

For the calculation of the instrumental function, several different approaches can be taken, for which a brief overview shall be given.
The fundamental parameter approach [105–107] is based on the analytical calculation of the beam profile. However, this method strongly constrains applications to a limited set of accessible measurable parameters. A more universal, yet computationally expensive approach is achieved by ray tracing [108–110]. The applicability of this method towards three dimensional problems is, however, constrained to a limited number of special cases, which are not applicable here.
In addition, methods like empirical modeling by an analytical function [111, 112] or a convolution of Gaussian functions [113, 114] are available to calculate the instrumental function. Yet, these methods are focused on powder diffraction setups and are not entirely suited to be compared to a high-resolution diffraction setups.

A framework which is applicable to the here presented experimental setup is introduced by Mikhalychev et al. [96]. Within this systematic study on high resolution diffractometry, a semi-analytical backward ray-tracing approach is considered, which provids sufficient accuracy to characterize the spatial distribution of the scattering pattern given in reciprocal coordinates. The method is fast and adaptable to describe coplanar and non-coplanar diffraction geometries (i.e., the analyzer scattering out of plane). Furthermore, it is used for diffraction on crystalline samples - which makes it especially applicable to the here presented case.
The study [96] shows, that fundamentally, the following features (*streaks*) can be identified with a high-resolution diffraction setup:

(i) The *analyzer streak* (Figure 5.28 a) is orientated perpendicular to the direction of the diffracted beam (Figure 5.28 b). The feature is calculated in the referenced work [96] on the basis of an incident wave vector with fixed length and direction. The shape is determined by the inaccuracy of the detection system, i.e., the determination of the scattering vector (Figure 5.28 b) defined by the detector's (angular) resolution.

(ii) The *monochromator streak*, which appears perpendicular to the direction of the incident beam (Figure 5.28 c). It is caused by the interplay of the source divergence and the intrinsic width of the monochromator crystal reflections. Calculations in the reference are performed for a constant outgoing scattering vector, while the direction of the incident monochromatic beam is varied according to the divergence (Figure 5.28 d).

(iii) The *wavelength streak*, which is found along the scattering vector as a pronounced line (Figure 5.28 e). It originates from the bandwidth of the incident

beam. For its calculation the direction of the incident wave vector is fixed and the wavelength is varied (Figure 5.28 f).

(iv) The *crystal truncation rod* (CTR), which is caused by the finite dimension of the sample. The effect originates from the truncation of the lattice itself, i.e., the finite volume. The feature is orientated parallel to the q_z component (Figure 5.29).

All these features are produced concurrently for a given diffraction setup. The are compared to the obtained scattering data below in Figure 5.32. The simulation performed in the referenced study includes all of the above explained effects and generates a scattering pattern, for which the concurrent features can be identified individually (Figure 5.28) due to a comparable magnitude.
In the Ref. [96] the simulations are performed and compared to measurements for a single crystal silicon (001-cut) sample in 224 orientation. The incident beam is monochromatized by a germanium 400 crystal in four-bounce geometry and the diffracted radiation is analyzed by a germanium 220 crystal in two-bounce geometry. Simulation and experimental data is found to be in good agreement and the origins of features in the scattering pattern are clearly identified.
The experimental setups used for the determination of the instrumental function and the phase-matching scans are very similar. Even despite the differences in the experimental parameters (incident energy, monochromator and analyzer crystals), the obtained scattering patterns are comparable in shape. Furthermore, the features determining the instrumental function are identified for the phase-matching scans as well. Based on the study's findings, the origins of these features are traced back to experimental components and beam parameters.
The individual features and the complete instrumental function (Figures 5.28 and 5.29) are presented in reciprocal coordinates, thereby representing a map of the reciprocal space. For the direct comparison of the instrumental function (given in reciprocal space) with the phase-matching scans a transformation of the latter is required, which is given in the following paragraph.

Reciprocal Space Maps

It is common practice to present the instrumental function in reciprocal space, i.e., by coordinates q_x and q_z of the momentum transfer $\vec{q}$. The underlying data set, however is acquired in the same manner as the phase-matching scans, namely in angular space: The sample is rotated (Ω-scan), while the horizontally scattered (2θ) intensity distribution is recorded, generating ω - 2θ angular maps. The representation of these $\Omega - 2\theta$ scattering patterns in reciprocal coordinates are referred to as *reciprocal space maps* (RSM).
The transformation is performed under consideration of the scattering geometry (Figure 5.30).
The scattering vector $\vec{q}$ can be written as components parallel $q_{\parallel}$ and perpendicular $q_{\perp}$ to the incident beam

$$\begin{pmatrix} q_{\perp} \\ q_{\parallel} \end{pmatrix} = |\vec{k}_{in}| \cdot \begin{pmatrix} \sin(\theta_f) \\ \cos(\theta_f) - 1 \end{pmatrix}$$

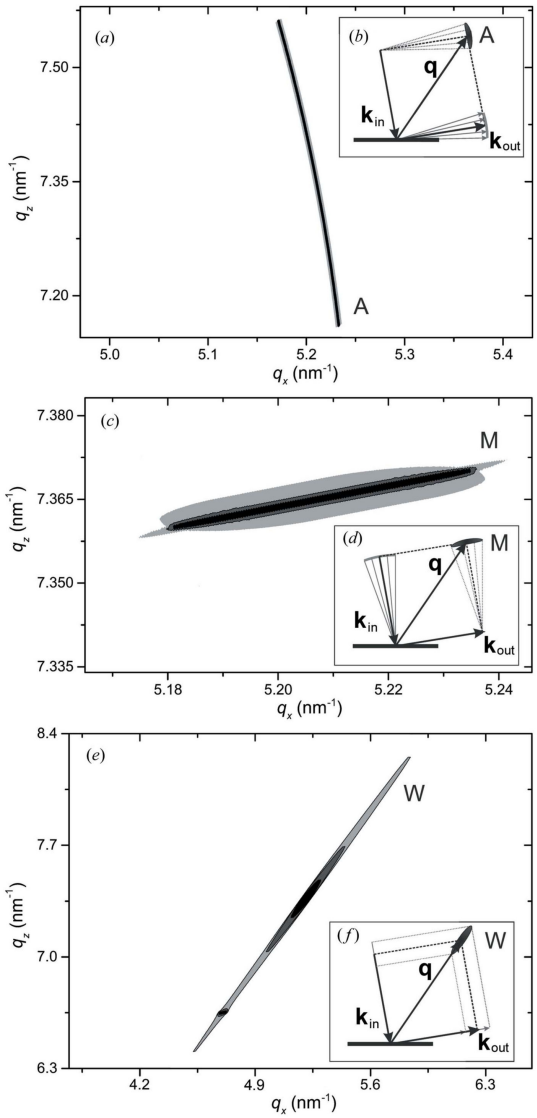

Figure 5.28: Simulated reciprocal space maps from Ref. [96] illustrate three different features in the scattering pattern: the analyzer streak (a), the monochromator streak (c) and the wavelength streak (d). The concepts of the streaks origins are shown in (b), (d) and (e), respectively. Simulation and experimental confirmation is performed on an ideal silicon sample in 224 orientation.

The reciprocal coordinates q_x and q_z are the components of the scattering vector $\vec{q}$ within the reference frame of the sample, spanned by x and z (Figure 5.30). The detailed

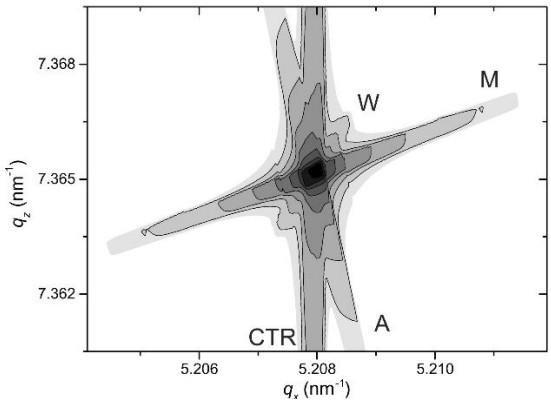

Figure 5.29: Simulated reciprocal space map from Ref. [96] for Si 224: analyzer (A) and monochromator (M) streak are dominant features. The wavelength streak (W) is weaker in comparison, yet observable. The crystal truncation rod (CTR) is orientated parallel to q_z and yields a dominant contribution to the scattering pattern.

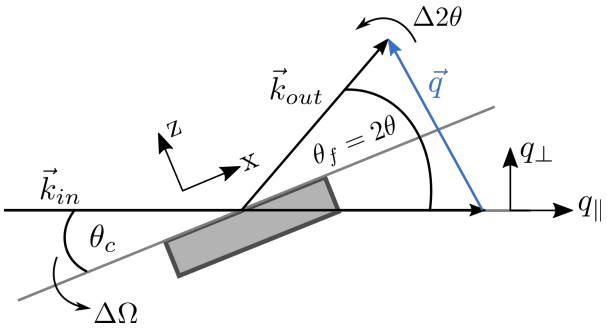

Figure 5.30: Geometrical consideration of scattering geometry for transforming real space coordinates (x and z) to reciprocal space coordinates (q_x and q_z).

transformation into q_x and q_z coordinates is performed via

$$q_x = |\vec{k}_{in}| \left[\sin(\theta_c)\cdot\sin(\theta_f) + \cos(\theta_c)\cdot(\cos(\theta_f) - 1)\right]$$
$$q_z = |\vec{k}_{in}| \left[\cos(\theta_c)\cdot\sin(\theta_f) - \sin(\theta_c)\cdot(\cos(\theta_f) - 1)\right]$$

with the definitions $\theta_c = \theta_B + \Delta\Omega$ and $\theta_f = 2\theta_B + \Delta 2\theta$.
These transformations are performed for the phase-matching scans, exemplary for the 400 orientation. This orientation is chosen, due to its symmetry, since the lattice planes are orientated parallel to the crystal's surface. The transformation for other reflexes is performed in a similar manner, under additional consideration of the angle spanned between lattice planes and sample surface. The original and transformed data sets are presented for the previously discussed low idler energy cases $E_i = 1.3$ eV, since the

influence of the instrumental function is dominant (Figure 5.31).

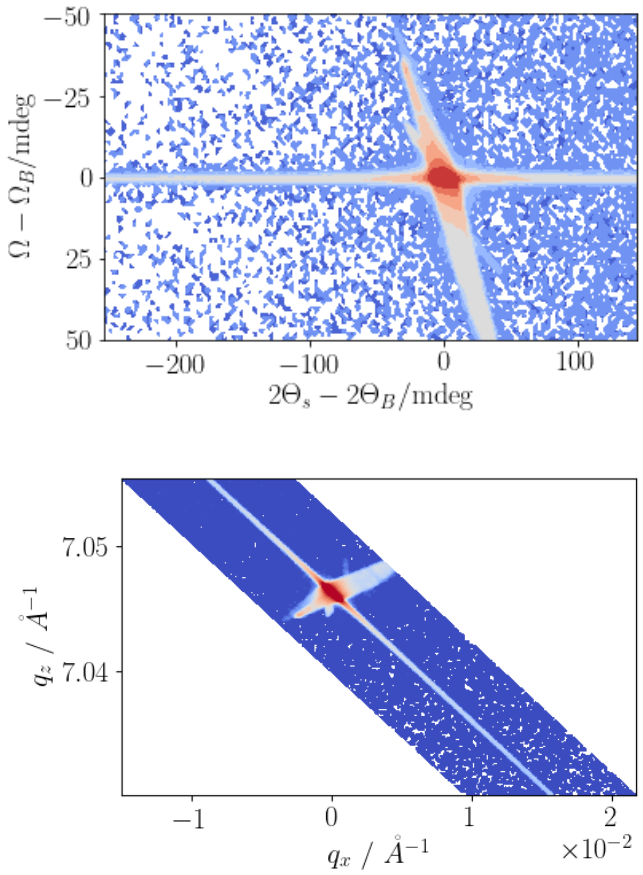

Figure 5.31: The phase-matching scans at a low idler energy of $E_i = 1.3$ eV at the 400 orientation in angular (top) and in reciprocal coordinates (bottom).

The phase-matching scans in reciprocal space representation are equivalent to the reciprocal space maps [96] and can be directly compared (Figure 5.32) - however under consideration that the analyzer for the reference data was tuned to the fundamental energy, whereas for the phase-matching scans the analyzer was slightly detuned in energy, i.e., $\Delta E = 1.3$ eV.
The deviation in the arrangement of the features within the reciprocal space is due to the different orientations which are studied, namely Si 224 for the reference and diamond 400 for the phase-matching scans.
The confined feature of the analyzer streak (Figure 5.32) is strongly pronounced. It is spanned over the complete range of $\Delta q_x = 0.01$ Å^{-1} and $\Delta q_z = 0.025$ Å^{-1} in case of the phase-matching data. This behavior is also observed in the results of the reference

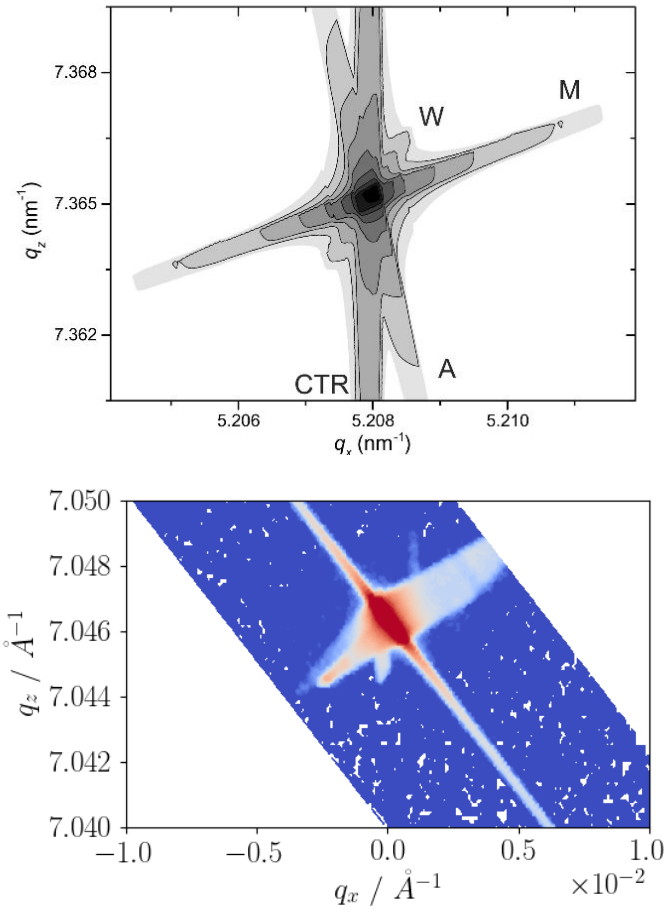

Figure 5.32: Comparison of simulated instrumental function [96] with phase-matching scan transformed to reciprocal coordinates.

study, in which values of $\Delta q_x^{(Ref)} = 0.025$ Å^{-1} and $\Delta q_z^{(Ref)} = 0.030$ Å^{-1} are reported. The analyzer streak is expected to be orientated with an angle θ_B, the Bragg angle of the sample, with respect to q_z. This can be confirmed with the data set from the phase-matching scan and supports the identification of this feature as analyzer streak.
Furthermore, the broader feature - almost perpendicularly orientated to the analyzer streak - is identified as the monochromator streak. For the phase-matching data, Δq_x of 0.08 Å^{-1} is acquired (Figure 5.32) and thereby comparable to the range reported in the reference $\Delta q_x^{(Ref)} = 0.06$ Å^{-1}.
Since the analyzer streak is directed perpendicular to the diffracted beam (see definition

above) and the monochromator streak perpendicular to the incident beam, the scattering features are perpendicular towards each other in the case of the 400 orientation, for which the Bragg angle yields $\theta_B \cong 45\,^\circ$ (at 10 keV).
The third feature explained and identified in the reference study, namely the wavelength streak, cannot be identified in the phase-matching data. It is relatively weak (Figure 5.32) in comparison with the other features and might be not detectable due to the strong overexposure.
Finally, the small features parallel to q_z might be identified as remainders from crystal truncation rods, as they are the only observed feature parallel to q_z. For a clear identification of the latter feature's origins a more detailed analysis under careful consideration of the influence of the detuned analyzer is required, which is beyond the scope of the here presented study.
For higher analyzer detunings, the magnitude of the scattering pattern decreases, as discussed earlier (Section 5.2.2). This observation corresponds well with the expected behavior within the framework of the instrumental function.
Notably, the $\Omega - 2\theta$ scans (or reciprocal space maps) and the resulting instrumental profile can be used for optimization of the setup's alignment for future studies. The beamline optics should be tuned with respect to minimizing the magnitude of features observed in the scattering pattern.

Finally, it has to be noted, that specifically for the investigation of low efficiency effects, which result in only minor changes in the scattering pattern, the influence of the setup needs to be understood in detail. Therefore, this detailed characterization of the instrumental function and concurrent low efficiency effects is indispensable.

5.3.2 Crystal imperfections

The nonlinear material, diamond, which is used in this study is not pre-characterized. Even though synthetic diamonds, generated by chemical vapor deposition (CVD), are available as single crystals, they do, however, include dislocations and a certain degree of mosaicity[4]. Crystal imperfections thereby influence the measured scattering pattern, requiring the usage of a pre-characterized sample of monochromator quality [115, 116] in the optimal case. It was found [117], that line defects influence the scattering pattern in a more severe manner than impurities (mostly nitrogen and boron). This effect already becomes apparent when studying the Rocking curve widths. Crystal imperfections thereby do not directly influence the phase-matching condition. These imperfections reduce the amount of intensity available for nonlinear scattering, since a fraction of the incident intensity is scattered on the imperfections increasing the elastic background, therefore not contributing to the nonlinear signal.

5.3.3 Absorption and scattering by air

Another contribution to the detected signal is the scattering of x-rays on air. The here presented measurements from the systematic study (ESRF) are performed neither un-

[4]Mosaicity is a crystallographic measure, which describes the spread of crystallite orientations. Experimentally the mosaicity of a crystalline specimen can be determined by Rocking curves.

der helium atmosphere nor in vacuum. The contributions from air scattering - as a concurrent effect - is therefore considered for the experimental setup.
Within the experimental setup the total beam path through air needs to be considered for absorption considerations. The beam propagates: from the beamline's beryllium window, via the sample and towards the detector through air; covering a total path lengths of approximately 2 m. Due to air absorption the beam transmission is reduced by factor of approximately 0.75. Beyond that, the air scattering broadens the beam profile, increases the divergence and causes a diffuse background.
The estimated magnitude of this contribution is performed on the basis of scattering measurements performed at ID09, ESRF, using a focused beam. At an energy of 18 keV, an incident flux of 10^{12} ph/s and a path length of 6 cm, $300-1000$ counts per pixel (with 70 µm pixel size) are measured per second, for a scattering vector of up to $|\vec{q}| = 1\ \mathring{A}^{-1}$. For a 10 keV beam the count rates might be an order of magnitude higher than for the 18 keV case.
The beam path contributing to air scattering, which is finally detected, yields solely the distance from the analyzer to the detector, which is measured to $d = 40$ cm. The air scattering generated in front of the analyzer is shielded by this component from the detector.
A scattering vector $|\vec{q}| = 1\ \mathring{A}^{-1}$ at 18 keV is equivalent to scattering angles of 6 deg and for 10 keV to scattering angles of 11 deg. Thereby the contribution of air scattering is broad in angular space.
The process of air scattering has - under the above made considerations - an approximate efficiency of 10^{-10} to 10^{-8}. It is thereby mostly pronounced at the Bragg condition, for which the scattered intensity is highest. The effect of air scattering therefore contributes to the broad angular ($2\theta_s$) scattering signal at Bragg condition, which is observed for the phase-matching scans at all analyzer configurations.

5.4 Upper Bound of Conversion Efficiency

Even though the effect of parametric conversion of x-rays into visible photons is not observed, an order of magnitude estimate for an upper bound of the conversion efficiency of XPDC can be given. The determination of this bound is achieved under detailed evaluation of the setup's resolution and detection capabilities.
Starting with roughly 10^{13} photons/s coming from the beamline's Si 111 monochromator, the high-resolution monochromator (Si 311) reduces the flux by a factor of 3. The monochromatized beam impinges on the sample, where the XPDC conversion takes place with yet unknown efficiency ε. All potentially down-converted radiation is collected within the bandwidth of the analyzer (0.3 eV) and the solid angle of each individual pixel ($2.1 \cdot 10^{-9}$ sr). The signal is further reduced by air absorption. The reduction is calculated to a factor of ~ 0.75 for a 2 m beam path in air. Furthermore, the quantum efficiency of the detector is taken into account. At 8 keV the efficiency yields 100%; at 15 keV 68% [85]. For our calculations we estimated the quantum efficiency to 90% for an incident energy of 10 keV.
Within this configuration, the count of a single photon per second per pixel would thus correspond to a conversion efficiency of 10^{-12}. In order to give a conservative esti-

mate under consideration of the noise level at the detector, we apply a threshold of 10 photons per pixel. This ultimately yields an upper bound of 10^{-11} for the conversion efficiency, which should be detectable by the presented experimental setup.
Irrespective of its coarse nature, this estimate presents an important benchmark for future studies of XPDC. We conclude that the inherent conversion efficiency must by smaller than 10^{-11}. This result is in line with previous experimental and theoretical studies (in the non-degenerate regime [18, 19, 29] as well as with new theoretical approaches [53] for parametric conversion processes in the x-ray regime.
The upper bound indicates the minimal requirements placed on future experimental resolution (see Chapter 8.1.1) and necessary suppression of concurrent elastic (i.e., linear) effects.
In addition, it also serves as a point of reference for theoretical developments. In fact, a description of x-ray optical wave-mixing is under development [53] and the preliminary results obtained in this theoretical study are fully compatible with the here presented experimental estimate of the upper bound, suggesting an efficiency orders of magnitude lower than the presented upper bound.

Chapter 6

Implications on Published Results

The results of the systematic study are put into the broader scientific context within the following paragraphs. The absence of a clearly identifiable scattering signature of the nonlinear effect has implications for other studies in the field.
The findings especially impact experimental reports on x-ray parametric down-conversion processes in the regime of low idler energies, namely within the range of ultraviolet (30 - 20 eV) to visible (4 - 2 eV) energies [102–104]. The therein reported experimental proceedings as well as methods for data analysis are critically discussed here.
Under consideration of the above presented results, these previous studies demand a re-evaluation of the (specific) identifications of XPDC signals made within. Furthermore, the interpretations towards physical effects (e.g., phase transitions) based on these identifications need to be revisited.

High energy-resolution measurements of x-ray into ultraviolet parametric down-conversion with an x-ray tube source, *Borodin et al.* [102], APL, 2017

The nonlinear effect of XPDC is spontaneous in nature. It thereby does not require high peak intensities, and could in principle - as done by Eisenberger and McCall [16] - be investigated with an x-ray tube source. However, in this special case of the degenerate regime, the generated photon pair is of half the incident energy and scattering angles are large. A differentiation of scattered photons with respect to energy and angle was easily achievable, even though count rates are low.
Observing XPDC in the UV-regime with a laboratory source is challenging due to various reasons. The available flux is lower, the source divergence larger and the emitted energetic spectrum is broader compared to synchrotron radiation sources. To achieve comparable beam parameters additional x-ray optics with a detailed characterization are required.
In the referenced study [102] the incident radiation used for the experiment is collimated and monochromatized, yet these parameters are not quantified, despite domi-

nantly influencing the scattering pattern, as shown in the previous analysis.
The diamond crystal used as sample is not further characterized. The Rocking curve width of the second sample, a lithium fluoride (LiF) crystal, yields 0.1 deg, which indicates a strong mosaicity and low crystal quality.
The intensity identified as nonlinear signal is broader in angle and stronger in magnitude than expected by the theoretical model introduced by Borodin et al. [102]. This discrepancy between model and data is explained in the report by the finite aperture of the detector, which integrates over several modes and energies. Yet, it is unclear why - if this summation over different modes is theoretically understood - this behavior is not incorporated in the theoretical model.
With the low crystallinity of the LiF-sample and the broad incident spectrum of the x-ray tube, it is likely - in the context of the analysis presented in this work - that the scattering signal, which is interpreted as the nonlinear signal, originates from linear elastic scattering.
Another indication for identifying the obtained signal as elastic scattering instead of a nonlinear signal, is based on the analyzer scans at three different phase-matching conditions (Figure 6.1), for idler energies of 30, 40 and 50 eV, respectively. The analyzer

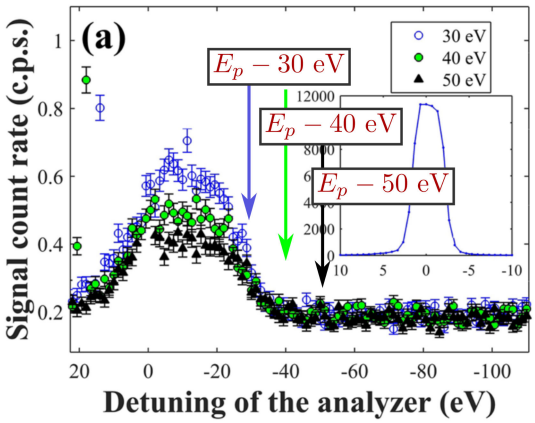

Figure 6.1: Analyzer scans at three different phase-matching conditions, $E_i = 30, 40$ and 50 eV, for diamond 220 obtained with a copper K_α laboratory source. Even though different phase-matching conditions are adjusted, the central energy obtained by an analyzer scan does not change; thereby questioning the observation of XPDC to UV. The expected peak positions are indicated by the arrows of respective color. Modified Figure taken from Ref. [102].

scans are expected to peak at the respective idler energies (indicated by the arrows in Figure 6.1). Yet, no shift of the peak is observed - it remains at the same position; only a reduction in intensity is observed.
This measurement goes well in line with the above presented findings, that only elastic scattering contributes in a predominant manner to the acquired signal. The reduction in magnitude of the peaks is explained by the lower availability of lower energy photons in the incident spectrum and is confirmed by the measurements of the systematic study.

Evidence for Collective Nonlinear Interactions in X-Ray into Ultraviolet Parametric Down-Conversion, *Borodin et al.* [103], PRL, 2019

This work investigates x-ray parametric conversion into UV idler photons and reports on a collective nonlinear interaction of the XPDC photons with plasmons.
The studies were performed on a synchrotron source with a standard Si 111 (double-bounce) monochromator and a spherically bent analyzer crystal (Si 555 in Johann geometry [118]). The analyzer provides only a single-bounce and therefore low suppression of spectral tails from the incident spectrum. The Rocking curve measurements with the detuned analyzer - sensitive to the selected signal energy - are performed on a diamond crystal in 220 orientation. The study reports on a spectral dependence of the XPDC efficiency, i.e., an idler dependent detected intensity. The reported non-monotonic spectral behavior is interpreted as interaction of the nonlinear effect with plasmons.
These interpretations are based on Rocking curve scans for individual x-ray signal energies. These Rocking curve scans vary in shape, position and magnitude, depending on the analyzer angle. It is not explicitly mentioned if a collimated or focused beam was used for the measurements, Figure 2 in Ref. [103] suggests the latter. The parameters of beam-collimation however, determine predominantly the scattering geometry, the setup's resolution and the sensitivity of the analyzer, which are crucial parameters of a XPDC experiment, yet they remain undetermined.
The authors' main evidence for observing XPDC is, that the peak of the Rocking curves appears at higher scattering angles ($2\theta_s$) for lower idler energies. This is - in principle also expected for XPDC (as shown by the kinematic phase-matching condition) - but this behavior is also expected for elastic effects. A scattering signature, which would be unique for XPDC is not shown. Measuring such a characteristic and unique signature is not possible by the choice of the experimental setup. Even though a 2D-detector is used, its spatial resolution cannot be exploited due to the bent analyzer crystal. The crystal collects and focuses the emitted light of a certain energy into a single point on the detector. A differentiation of scattering angles ($2\theta_s$) is thereby not enabled, which is however needed for differentiation between elastic and nonlinear signal.
Again, the interpretation of scattering signals obtained in this study is not based on a unequivocal signature of the nonlinear process.
Furthermore, the presumably falsely identified XPDC signal is interpreted towards collective interactions; an interpretation, which cannot be supported by theory nor experimental data.

Observation of strong nonlinear interactions in parametric down-conver-sion of X-rays into ultraviolet radiation, *Sofer et al.* [104], Nat. Com., 2019

This study reports again on XPDC into ultraviolet radiation for gallium arsenide (GaAs) and lithium niobate (LiNbO3) crystals. Strong nonlinear interactions are reported which cause increased conversion efficiencies of XPDC. The studies are performed on synchrotron sources, with a standard Si 111 monochromator (2-bounce).
Increased signal count rates by four orders of magnitude for the parametric down-conversion effect are reported and the enhancement of the nonlinearity in the x-ray

regime is explained by the authors by the broken inversion symmetry of the sample systems.
In the experimental setup, a 2D detector is used to acquire the scattered intensity, however, the angular resolution ($2\theta_s$) remains unused and the scattering pattern is not compared to the expected phase-matching angles from kinematic phase-matching. Instead, the 2-dimensional detector images are integrated along both dimensions, disregarding the recorded angular resolution. For each Rocking curve the maximum value of the acquired intensity is determined. For various idler energy settings of the channel-cut analyzer (Si 111, 3-bounce) these values are plotted and a non-monotonic behavior is observed, similar to the previously discussed report [103]. Selected peaks along these curves, for both sample materials (GaAs and LiNbO3), are interpreted by the authors as electronic or atomic transitions.
Yet again, the obtained data most likely originates from elastic scattering.
Applying the data analysis presented in the referenced work [104] to the data of the here presented systematic study (in which diamond was investigated, instead of GaAs and LiNbO3), a non-monotonic spectral behavior is observed as well and behaved in a similar manner, exhibiting several peaks. Moreover, a detailed analysis yields, that the spectral dependence is highly sensitive towards the selection of the region of interest on the detector images.
This striking similarity again supports the interpretation that the acquired intensity distributions in Ref. [104] stem from elastic effects, rather than nonlinear scattering. In conclusion the interpretation of the data towards a spectral dependence of XPDC cannot be supported by the results of the systematic study presented in this thesis.

On the basis of their aforementioned interpretation, the referenced study reports on an enhancement of the XPDC efficiency in centro-symmetric materials. To proof this hypothesis strontium barium niobate is investigated. This material is non-centrosymmetric in the ferroelectric phase, whereas it is centro-symmetric in the paramagnetic phase. Its Curie temperature T_C ranges between 340 and 350 K and is easily overcome by conventional heating methods, which are applied to achieve the phase-transition [1].
All studied sample systems are not characterized; no reference Rocking curve scan to determine the crystal quality is presented, which is strongly impacting the width of the elastically scattered signals, nor is the strontium barium niobate studied separately for both phases.
Rocking curve scans are performed for an idler energy of 20 eV below and above the phase-transition temperature. The sample angle set to fulfill the phase-matching condition remained unchanged, even though the reciprocal lattice vector is expected to change due to the heating and thereby changing the phase-matching condition itself ($\vec{k}_p + \vec{G} = \vec{k}_s + \vec{k}_i$).
The Rocking curve scans acquired while heating the sample, exhibit a strongly reduced peak intensity compared to the signal obtained without heating. The referenced study reports on an additional peak, at a shifted scattering angle ($2\theta_s$), which is interpreted as the XPDC signal of the material at the other phase.

[1] Despite heating the material beyond the Curie temperature, the phase-transition does not yield a complete reorientation of the material. To which degree this effect is apparent in the referenced study is not stated in the publication.

The observed behavior can, however, again be explained on the basis of elastic scattering: The change in the acquired signal can be attributed to heating of the sample, which causes a change in the lattice constant of the crystal and thus a shift of the Bragg position. In the referenced study, this effect is not considered and no realignment for the new lattice constant is performed.
Despite the lack of clear evidence for XPDC, the presented measurements are used as evidence for an enhancement of the XPDC efficiency at non-centrosymmetric crystals. Furthermore, the increased magnitude of the nonlinearity is explained on a dependence of the permanent dipoles within the nonlinear medium. It is stated that the nonlinear coefficient is strongest for the visible regime. A remark, which is taken from all optical considerations [119], which are not directly transferable to the x-ray regime as described earlier in Section 3.3 (the A^2-term needs to be taken into account, as the dipole-approximation is no longer valid).
Without clearly observing the characteristic scattering signature of XPDC, it cannot be claimed to have unequivocal proof of the effect, nor justify the interpretations of physical phenomena. The alleged applications, discussed in the aforementioned studies [102–104], are presented as novel techniques to probe material properties, while in fact being based on a fundamental misinterpretation

Chapter 7

Summary and Conclusion

In the beginning of the here presented work, the phenomenon of x-ray parametric down-conversion is introduced as a nonlinear scattering effect. Therefore, fundamental considerations with regard to the scattering of x-rays in general and for the nonlinear effect in particular are presented.
The conversion effect is determined by the kinematic phase-matching condition, which is constituted by energy and momentum conservation. It yields a characteristic scattering signature, being dependent from the incident energy, the sample material and selected conversion ratio.

The scope of this thesis includes a extensive review of theoretical and experimental studies; starting from first considerations of parametric conversion, towards the latest theoretical developments, which incorporate a fully quantized description of this nonlinear light-matter interaction.
Furthermore, the review summarizes experimental investigations of parametric conversion processes at various conditions. In addition, it spans across studies covering comparable processes, such as sum-frequency, difference-frequency and second harmonic generation. Thereby this thesis provides an extensive overview on the nascent field of x-ray nonlinearities.

With the aim to push x-ray wave-mixing processes towards first applications, this study aimed for the proof of principle and furthermore, for a systematic investigation of XPDC into optical photons. In this context, a reliable detection of the characteristic scattering signature requires a high spatial and spectral resolution, in combination with a detailed discrimination of concurrent background effects. Therefore, a high-resolution setup including a two-dimensional pixel detector is introduced and an analysis-strategy based on Rocking curve maps employed. Thus allowing to obtain a significantly more detailed view of the scattering than previous one-dimensional approaches. However, the anticipated characteristic signature is not observed.
The data, acquired under the improved conditions, exhibits feature-rich scattering patterns, which are identified as elastic contributions, originating from the incident spectrum in combination with setup components. The identification is performed on the

basis of instrumental function considerations, which are known from high-resolution diffractometry.
Yet, an upper limit for the effect's conversion efficiency of 10^{-11} in the highly non-degenerate regime can be determined on the basis of the experimental setup.

Putting the here presented results into the broader scientific context, contradictions arise with regard to previous studies, reporting the observation of XPDC into optical photons. The systematic study reproduces these specific signals with the same magnitude at similar scattering angles. The identification of these signals as elastic effects challenges the previous interpretations as XPDC signal and consequently demands for a reevaluation.

The essential findings of this systematic work are transferable to other studies aiming to resolve nonlinear effects in the x-ray regime, namely that the detailed understanding of the instrumental function is inevitable.
The here presented experimental setup and methodology will provide the basis for future investigations of the nonlinear conversion effect. A special emphasis will be put on the yet outstanding proof for XPDC into visible photons and the determination of its conversion efficiency.

Finally, the feasibility and importance to further pursue the investigation of the parametric conversion of x-rays is emphasized; not only due to the outstanding unequivocal proof, but in addition, due to the effect's intriguing capabilities for future applications. The envisioned future projects in combination with the experimental opportunities of the nonlinear conversion of x-rays, are presented in the following chapter.

Chapter 8

Outlook

The following section focuses in the first part on the extensions and modifications of the experimental setup itself, to enable experimental approaches towards the outstanding unequivocal proof for the nonlinear conversion of x-rays into optical photons. In addition, other possible nonlinear materials are proposed.
The second part gives an overview on experimental opportunities and future applications of x-ray frequency conversion. The experimental opportunities itself are divided into short and long term projects. The first ideas will be applied in upcoming experimental campaigns, whereas the long term strategies, aim to establish novel methodologies.

8.1 Extensions for future experiments

With the established setup, presented for the systematic study, the characteristic scattering signature of x-ray parametric down-conversion into optical photons cannot be resolved. The influence of the instrumental function, i.e., scattering contributions of the sample and x-ray optical elements, needs to be suppressed even further to achieve the detection of down-converted photons.
The results obtained from the discussion of the instrumental function (Section 5.3.1) form the basis of the considerations for further improvements of the experimental setup.

8.1.1 Increased Resolution Setup

The main requirement to finally measure the characteristic signature is that concurrent elastic processes are suppressed as far as possible. This can be achieved by different measures, which are presented in the following.

Improved Monochromatization The main contribution to these concurrent scattering processes is provided by the incident spectrum. Even though a monochromator (Si 111, double-bounce) is used, the spectral tails of the broad undulator spectrum are only suppressed and not eliminated entirely. The suppression factor itself depends on the

energy difference with respect to the fundamental energy and the monochromator type, which is used.
The standard configuration is constituted by the main monochromator, typically including Si 111 with two reflections. For a more effective monochromatization of the incident bandwidth, with improved suppression of the spectral tails, an additional four-bounce monochromator in Bartels configuration [120] is proposed. In this manner a four-bounce configuration acts as an additional slit, while preserving the divergence acceptance. The main monochromator (Si 111) of beamlines (e.g., P09 at Petra III, DESY) reflects the beam in (+, -) configuration - for nomenclature see Ref. [4].´ The additional monochromator configuration is set to (-, +, +, -); as such, the crystals of the main monochromator and the first two reflections of the additional monochromator actually constitute another Bartels configuration. The additional monochromator stage is set up by a pair of Si 111 channel-cut crystals. These do not reduce the bandwidth, i.e., $\sim$ 1.3 eV (FWHM), but increase the suppression of the spectral tails by additional orders of magnitude (Figure 8.1), resulting in a lower contribution of the elastic scattering effects.

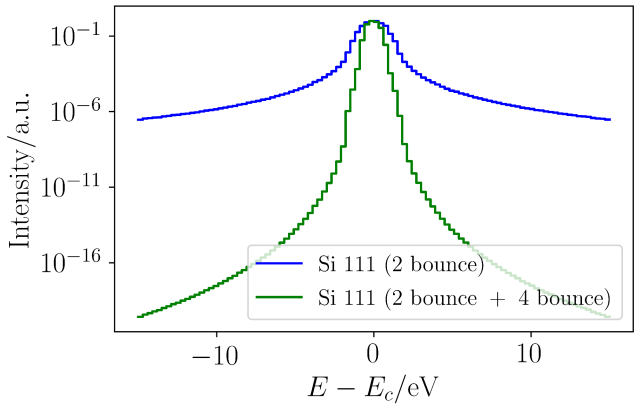

Figure 8.1: Comparison of spectral intensity distributions of the incident beam being monochromatized by the main Si 111 monochromator or together with an additional Si 111 4-bounce (-, +, +, -) configuration. The suppression of the spectral tails is improved by several orders of magnitude.

In addition, to the spectral improvement of the incident beam, the analyzer configuration can be improved as well (Figure 8.2). Instead of a two-bounce Si 440 (ID20, ESRF) or a three-bounce Si 111 (I16, DLS) configuration, another four-bounce configuration is proposed. This modified analyzer stage is composed of a set of two Si 111 channel-cut crystals. Even though the bandwidth of $\sim$ 1.3 eV at $E_p = 11$ keV is larger than the one of Si 440 (i.e., 0.3 eV), the suppression of elastic tails is increased. Due to the intrinsic limitation of divergence acceptance of the four-bounce configuration, the apertures included in the previous setup become obsolete.

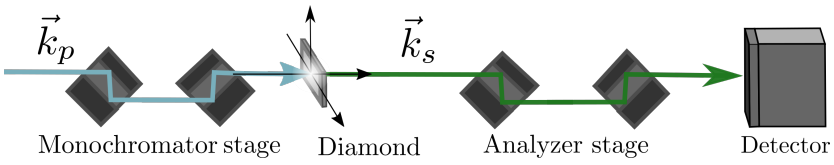

Figure 8.2: Experimental setup for high resolution. A four-bounce configuration (-, +, +, -) is envisioned to suppress the tails of the incident spectrum sufficiently. In addition another four-bounce configuration is used as analyzer stage.

The Si 111 reflection is chosen because it offers a relatively broad bandwidth, and thus allows for the transmission of sufficient flux, on the incident, as well as the detection side.

Instrumental Function Within the scope of this thesis it became apparent, that the instrumental function of the experimental setup needs to be understood in detail to eliminate elastic contributions as signal contamination for the nonlinear effect. Especially for the here applied setup, including a detuned analyzer, this understanding is not entirely achieved. Even though several scattering features (analyzer- and monochromator streaks) were identified, not all contributions are completely understood.
For future investigations a detailed analysis of all scattering contributions is envisioned, such that the investigative research towards low efficiency nonlinear effects is enabled.

Sample Material The additional elastic contributions of the experimental setup can be further reduced by optimizing the sample crystal itself.
Even tough a single crystal CVD-grown diamond is used, the sample contributes with concurrent elastic processes to the detected signal. Imperfections within the crystal, namely dislocations of crystallites and in general a reduced crystallinity add to diffuse background. The usage of a high quality diamond of 'monochromator quality', will improve the setup.
In addition, the mounting of the crystal is crucial, since stress and strain effects impact the scattering of the sample. Both stress and strain on the sample need to be minimized.

Shielding Further reduction of background effects can be achieved by the absence of apertures (as additional sources of scattering) and improved shielding of the detector.
Air scattering can be reduced by the introduction of a helium environment or flight tubes - both eliminating air from the beam path and reducing unwanted, yet concurrent, scattering contributions.

Alignment In addition, the features originating from the instrumental function can be used directly to improve the setup's alignment. Minimizing the features visible in the reciprocal space maps (RSM) via re-alignment of beamline optics and the sample can yield a more precise overall alignment of the experimental setup.

With this reduction of scattering contributions from beamline optics, in combination with improved incident spectrum and analyzer stage, the effect might be detectable with increased acquisition times.

8.1.2 High Bandgap Materials

Next to diamond, which is chosen due to its high crystalline qualities, its transparency in the visible regime and its relatively high bandgap ($E_{gap}^{C^*} \simeq 5.4$ eV), other materials could be chosen as nonlinear material.
The investigation of suitable nonlinear materials can be extended towards high band gap materials, as the parametric conversion can be investigated below the absorption energy. Candidates for these high band gap materials would be aluminum oxide (Al_2O_3) and magnesium oxide (MgO_2). Having band gaps above 7 eV, they are prime candidates as nonlinear material. In addition it is advantageous to have light materials, since absorption, and therefore heat deposition, is low.
Another class of interesting materials are fluorides, such as lithium fluoride (LiF), magnesium fluoride, (MgF_2) or calcium fluoride (CaF_2). These crystalline materials are characterized by their large bandgap energies $E_{gap}^{\mathrm{LiF}} = 10.9$ eV [121], $E_{gap}^{\mathrm{MgF}} = 12.8$ eV [122] and $E_{gap}^{\mathrm{CaF_2}} = 10.0$ eV [123], respectively.
In addition, fluorites with lead (PbF_2), strontium (SrF_2) and barium (BaF_2) are possible candidates. Moreover, all of the above mentioned crystals exhibit a cubic crystal structure; except for MgF_2, which is tetragonal.
Finally, quartz (SiO_2) is another possible material, which is readily being used for hard x-ray applications. For low density quartz ($2.65\mathrm{g/cm^3}$) and high density ($4.28\mathrm{g/cm^3}$), band gap energies of $E_{gap}^{\mathrm{SiO_2}} = 10.1$ eV and 8.9 eV are reported [124], respectively.

The main requirement for their usage is the availability as a single crystal with adequate thickness of approximately $200 - 500$ µm. However, the low heat conductivity might become problematic, as the incident beam might heat the sample. This heat deposition can cause a change at the lattice parameter. Future experiments need to investigate these crystal's applicability.

Benchmarking with new theoretical models The intensity distributions obtained from the QED treatment (see Section 3.3) of non-degenerate XPDC yield elliptically shaped scattering patterns of nonuniform magnitude (Figure 8.3).

The observation of these scattering patterns becomes the ultimate goal to experimentally confirm the conversion of x-rays into visible photons and theory confirmation. Next to the characteristic scattering signature for a sample angle scan, the 2-dimensional scattering profile for a fixed sample angle can be used as a proof for observing XPDC. The increased resolution of the experimental setup proposed in section 8.1.1 will be essential for realizing these experimental parameters.

Beyond the spatial distribution of intensity, which is expected to be existent in a three-dimensional cone for each energy ratio, the determination of the total cross section is still an open question.

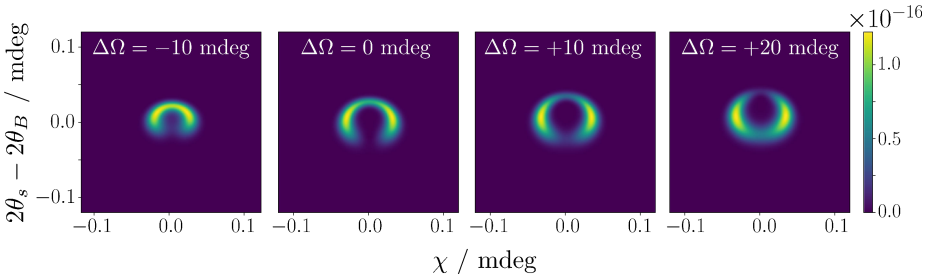

Figure 8.3: Simulation results for two dimensional intensity distributions of XPDC signal photons at selected sample detunings $\Delta\Omega = -10, 0, +10$ and $+20$ mdeg, respectively for the 220 orientation of diamond at 11 keV. The scattering angle $2\theta_s - 2\theta_B$ is defined as before and the scattering along the χ-dimension is orientated perpendicularly. The intensity is given in arbitrary units and varies along the elliptical shape. The Simulations are based on the theoretical approach presented in Section 3.3 and data provided by private communication.

8.2 Experimental Opportunities

Within the following section an outlook for prospective future experiments and applications of the nonlinear conversion effect shall be given. In contrast to the previous section it is not focused on the evidence of the nonlinear effect itself, but rather on possible applications.
Already in early publications concerning the effect of x-ray parametric down-conversion, several applications are presented. These applications mainly exploits the inherent relation of the generated photon pair, ranging from mere correlation in the case of high conversion asymmetry to even (presumed) entanglement, in the case of degeneracy.

The possible applications of x-ray parametric conversion is manifold and ranges from imaging methods, via nonlinear spectroscopies, towards to the exploitation of the quantum nature of the generated photon pair.

8.2.1 Stimulation of XPDC

The effect of x-ray parametric down-conversion, which is spontaneous in nature, can be stimulated.
An active stimulation of the effect is achieved by an additional external light field. The stimulating wavelength needs to be equivalent to the selected idler wavelength of a specific conversion ratio. The incident angle of the external optical field is set to match to internal phase-matching condition on angular constraints and under consideration of the refractive index.
Experimentally this stimulation can be achieved by an optical laser, synchronized to the pulsed x-ray source. It is beneficial, that the pulse lengths of x-ray and optical beam are similar.
It is expected (without a complete corresponding model) that stimulation of the process

itself will result in higher measurable conversion rates.

8.2.2 Photon Correlation

The bosonic nature of light can yield higher order correlations. Especially, the process of parametric down-conversion generates photon pairs with higher correlation properties, which can be used for the following applications.

Exploiting Correlation In general, detection events might be correlated, even in the absence of first-order correlation, and for photons originating from thermal and even different sources. This concept was introduced via the Hanbury-Brown Twiss (HBT) experiment [125], which was applied in astronomy to achieve improved angular resolution, beyond the diffraction limit. HBT was also demonstrated for the x-ray regime [126, 127], where the two-photon correlation of synchrotron sources was measured and used to determine the coherence properties of the source.

A two-photon optical imaging experiment, which exploits the correlation properties of photons - similar as in the HBT - is referred to as 'ghost imaging'. It was investigated for the all optical case [128] in 1995 and yielded an improved resolution. The impact of light correlation in terms of the 'ghost imaging' method is discussed in detail in other works [129].
Ghost imaging has been shown in the x-ray regime in recent years [50]; predominantly as a proof of principle and for thermal light from undulator sources. Improvement on detection sensitivity, as well as on temporal and spatial resolution was achieved.
The studies focused mainly on undulator sources (with thermal photon statistics) or considered XPDC in the degenerate case, in which the correlation (or even entanglement) of the photon pair improves on imaging capabilities.
Beyond that, the highly non-degenerate regime of parametric down-conversion can be considered for ghost imaging [51]. The sample system is exposed to the lower energy idler photons, while the x-ray photons are detected in coincidence. The asymmetry ratio of the signal and idler photon is hereby exploited. The coincidence detection of the x-ray signal photon results in a magnification factor, that enables (in principle) atomic scale resolution [51]. Furthermore, this method enables the reduction of dose, which is especially interesting for (diffraction) imaging of protein nano-crystals and single molecules.

Evidence for Entanglement Being able to exploit the correlation of the generated photon pair, the experimental proof of entanglement is still outstanding. Until now, there have been several successful demonstrations on time and energy correlations for XPDC generated photons [130], however entanglement between signal and idler was not yet observed.
Time- and energy resolution of x-ray detectors are yet not sufficient to reach the Fourier-transform limit. The experimental proof for time, energy and polarization entanglement, remains experimentally challenging. However, the measurement of position/-momentum entanglement appears feasible, similar to approaches taken in the optical

regime [131].

8.2.3 Bell's Inequality in the X-ray Regime

Entanglement for photon pairs generated by parametric down-conversion was theoretically described [5, 132] and experimentally confirmed [132] for the all-optical case. Even though the theoretical considerations are valid in the x-ray regime as well, the experimental evidence for entanglement in this regime, remains an open challenge as described previously.
Yet, applications are already envisioned for entangled x-ray photon pairs: Entangled x-rays would enable to close the detection loophole for proving Bell's inequality.
Bell's theorem states, in short, that quantum physics does not comply with the theory of local hidden variables, i.e., it is incomplete [133, 134]. Inequalities were constructed to distinguish between quantum mechanics and local realistic theories [133, 135, 136]. Bell himself wrote: 'If [a hidden variable theory] is local, it will not agree with quantum mechanics, and if it agrees with quantum mechanics, it will not be local. This is what the theorem says.' [137].
The Einstein-Podolski-Rosen paradox [134] was experimentally realized for optical photons [131] and Bell's inequality in the optical regime was shown in several experiments [138, 139]. However, the so-called 'detection-loophole' is the most relevant problem for these optical experiments.
For enabling a loophole free detection of this inequality, quantum efficiencies of detectors must exceed 82.8% [140]. For optical photons this limit is challenging and not achieved today. But for the x-ray regime, detectors with quantum efficiencies of above 95% are readily available.
With entangled x-ray photon pairs the famous investigation of Bell's inequality can be extended into the x-ray regime; profiting from high detection efficiencies available.

8.2.4 Spectroscopic Applications

Reduced Dose It has been proposed to use the generated photon pair for x-ray absorption spectroscopy with highly reduced dose [51, 141]. The methods exploits the correlation of the photon pair. One photon is being send to probe the sample, passing onto the detector, while the other photon is used as reference. Thereby, an overall reduced intensity is required to obtain a similar signal quality: reducing the required dose, this approach will be a beneficial method for fragile biological samples.

Improved Statistics The exact number of photons interacting with the sample can be identified (except for additional detection limitations) on the basis of converted photon pairs. Once the correlation property is known, the one photon is sent to the sample, while the other is used as reference. The use of down-converted photon pairs for spectroscopy or imaging methods improves the statistics to sub-poissonian statistics [50]. Conventional I_0 measurements are invasive to the incident beam as an additional element is inserted into the beam path. Determination of incident photons via photon pairs makes conventional monitoring obsolete. Yet however, the overall flux is reduced immensely due to the low conversion rate.

Two-Photon Spectroscopy Theory on linear two-photon spectroscopy [142,143] has been developed and the concept has been applied in the visible regime [144, 145]. The transition into the x-ray regime is proposed as well [146].
Furthermore, x-ray parametric conversion processes can be used for imaging ultrafast electron dynamics. Specifically, this method was proposed (theoretically) for sum frequency diffraction [147], with its challenging experimental implementation yet outstanding.

Spectroscopy with Quantum Light A detailed and extensive summary on the nature of quantum light and its applications for spectroscopies is presented by Mukamel et al. [146].
Quantum light paves the way for novel approaches of spectroscopy by exploiting parameters of these quantum states and the accompanying variations of photon statistics. The quantum light can be used as a versatile tool for sensing and spectroscopy. It has the potential to reveal novel observables, which are not accessible by classical light.

Beyond applications for spectroscopy, the quantum nature of the down-converted photon pair can be used for experiments within the field of quantum optics itself. XPDC enables, for example, the preparation of pure Bell states with x-ray wavelengths [47]. Again the experimental evidence of these states is outstanding.

Time Resolved Probe Indifferent of the specific method, imaging or spectroscopic nature, the effect remains intrinsically spontaneous. It is therefore a promising candidate to be used at x-ray free electron laser sources, exploiting the capabilities of short, bright pulses. Being spontaneous in nature and linear in intensity dependence, the effect can be used as a temporal probe to study dynamics - its time resolution being dependent from the sources' pulse length and exploiting the above introduced concepts for imaging, spectroscopy and quantum mechanics.

Appendices

Parameters of Light Sources and Beamlines

		DLS	ESRF	Petra III
Filling mode		Standard	7/8 +1 Hybrid	Timing
Number of bunches		900	868 + 2+ 1	40
Interbunch spacing	ns	2; 72 (gap)	2; 176	192
Pulse charge	nC	0.2	0.56 and 5.62	16
Total current	mA	300	200	100
Circumference	m	500	844	2304
Electron energy	GeV	3	6	6
Round trip time	µs	2.0	2.81	7.7

Table 1: Table of parameters for the different light sources DLS, ESRF and Petra III.

Light Source Beamline	Diamond Light Source [148] I16	ESRF [84, 149] ID20	Petra III [150] P08
Source brilliance	$5 \cdot 10^{19}$ ph/s/mm^2/mrad^{2}0.1%bw	$5 \cdot 10^{19}$ ph/s/mm^2/mrad^{2}0.1%bw	10^{18} ph /s/0.1%bw/mA
Undulator length	2 m	6 m	2 m
Fundamental energy E	10 keV	10 and 11 keV	10 keV
Flux after main mono	$1.0 \cdot 10^{13}$ s^{-1} (6 keV)	$7.0 \cdot 10^{13}$ s^{-1} (9.7 keV)	$\sim 10^{11}$ s^{-1} (10 keV)
1st Monochromator	Si 111	Si 111	Si 111
2nd Monochromator	n.a.	Si 311	Si 511
Resolution $\Delta E/E$	$1.1 \cdot 10^{-4}$	$2.8 \cdot 10^{-5}$	$2.0 \cdot 10^{-4}$
Focused beam ($v \times h$)	35×184 µm	9×18 µm	2×30 µm^2
Beam divergence ($v \times h$)	$0.04\,(v) \times 0.11(h)$ mrad^2	20 µrad	5.5×8.7 µrad^2
Polarization	horizontal	horizontal	horizontal
Diffractometer	6-circle Kappa	2-circle (horizontal)	6-cirlce Eulerian
Analyzer crystal	Si 111 (3-bounce)	Si 440 (2-bounce)	Si 440 (2-bounce)
Analyzer resolution	1.3 eV	1.3 eV	0.3 eV
Detector	FMB Oxford [95]	MaxiPix [85]	Pilatus 100k [151]
Detector type	APD	CCD	CCD
Pixel size	5000 µm	55 µm	172 µm
Sensor thickness	300 µm	500 µm	1000 µm

Table 2: Table of beamline parameters for different the light sources: Diamond Light Source, ESRF and Petra III.

Rocking Curves

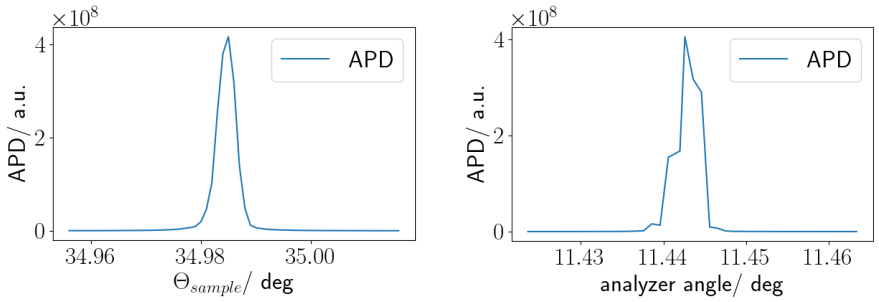

(a) (b)

Figure 4: The Rocking curve of diamond in 220 orientation in transmission geometry is shown in (a) and the rocking curve of the analyzer crystal for the Bragg condition of the diamond shown in (b) acquired with 10 keV incident beam at Diamond Light Source, I16.

Coincidence Setup

Unequivocal evidence for parametric down-conversion is obtained by coincident detection of the generated photon pair. It requires the measurement of both, x-ray signal and optical (or infrared) idler photon by fast single photon counting detectors in combination with fast coincidence electronics (Figure 5).
For the coincidence detection a custom made megahertz data acquisition (MHz DAQ) system based on micro TCAs[1], with high-speed digitizers (SP Devices) is used [152]. The digitizer consist of four 12-bit analog-to-digital converters (ADCs) accompanied by a Field Programmable Gate Array (FPGA; Xilinx Virtex 6), which is capable of sampling signals with 2 GS/s in up to four different channels. For the coincidence setup the MHz DAQ is used in a configuration, where the acquisition trigger is given by the x-ray detector. The x-ray signal is detected via an APD [95] (FMB Oxford) and

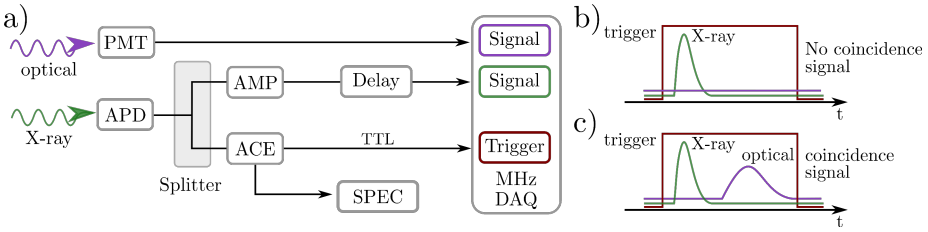

Figure 5: Schematic setup up coincidence electronics used to measure x-ray signal and optical idler simultaneously. The x-ray signal from the APD is split: one fraction is used as the later trigger for the MHz DAQ system and the other fraction is sampled as the x-ray signal itself. Additional electronics, i.e., amplifiers and delay stages account for sufficient signal levels and arrival time discrepancies.

is subsequently split into two identical signal pulses, of which one serves as the trigger, since the DAQ requires a TTL signal of at least 1 V amplitude as trigger source. The other pulse is fed into the so called ACE box[2], where the signal pulse is digitized and read by the beamline acquisition system (SPEC). The ACE box additionally delivers a synchronized TTL signal, which is used to trigger the MHz DAQ. The other part of the APD signal is amplified, which is necessary due to the reduction in signal amplitude by the splitter. In addition the signal pulse is delayed, since it needs to reach the MHz

[1] also micro TCA for *mirco Telecommunication Computing Architecture*
[2] Further information can be found in Ref. [95]

DAQ after the trigger signal, which is itself delayed by the conversion within the ACE box.
In comparison to directly triggering the DAQ by the machine frequency, this configuration has the advantage, that all events, in which an x-ray pulse impinges the sample but the APD detects no photons are ignored. The amount of data is drastically reduced compared to a continuous (machine-)triggered configuration.
Each time the APD detects an x-ray photon, the MHz DAQ is triggered and the acquisition gate is set. All pulses, both x-ray and optical, which are detected within this acquisition window are sampled and recorded by the MHz DAQ system. The coincidences could than be determined via the arrival time within the acquisition window.

Detection of Optical Idler Photons

The down-converted photon pair consists of a hard x-ray and an optical photon, depending on the chosen phase-matching condition. Both photons should thus be detected in coincidence. The detection of the idler photon is enabled by using a photomultiplier, which is sensitive to UV-VIS light (here a head-on photosensor, model H10492 from Hamamatsu).

For the detection of optical photons two different techniques are used: A spectrometer with a CCD camera to measure the total emission spectrum and a fast photomultiplier tube (PMT) for coincidence detection.
Since the fluorescent properties vary for different samples, dependent on the amount of impurities and vacancies, the x-ray induced fluorescent spectrum needs to be characterized for each sample individually. Over the typical scan range of a few hundred millidegrees the optical fluorescence spectrum remains unchanged. The fluorescent spectrum from the diamond crystal is analyzed with an optical spectrometer (Acton SP2150; Princeton Instruments [153]), containing switchable gratings in combination with a CCD camera (Pro EM 512 BX3 [154]). For the selected idler wavelength of 620 nm (2 eV) a 150 g/mm grating with 500 blaze is chosen (with $\sim 60\%$ efficiency). The camera itself has an average quantum efficiency of 95% around 620 nm.
For this experiment, the synchrotron (here: ESRF) is operated in four bunch mode with an interbunch spacing of 0.7 µs (357 kHz repetition rate). With this frequency, scattering events are generated in the diamond sample crystal. The scattered x-ray photons are filtered by the channel-cut crystal analyzer (not shown in Figure 6) and detected with an APD. The short signals from the APD ($<$30 µs pulse width) thus allow to set a corresponding short coincidence time window, since the PMT pulses (via optical photons) are equally short in time.
The emitted fluorescent optical light is collected by a lens and focused into a multimode optical fiber. The lens is positioned in 13 cm distance to the sample and covers a solid angle of 0.03 sr.
In a first step, the collected light is analyzed by the spectrometer, which is used together with the CCD camera (Figure 6 b) to determine the x-ray induced fluorescent spectrum.
After this initial characterization of fluorescent emission, the spectrometer setup is exchanged with the photomultiplier tube (PMT) for detecting single optical photons

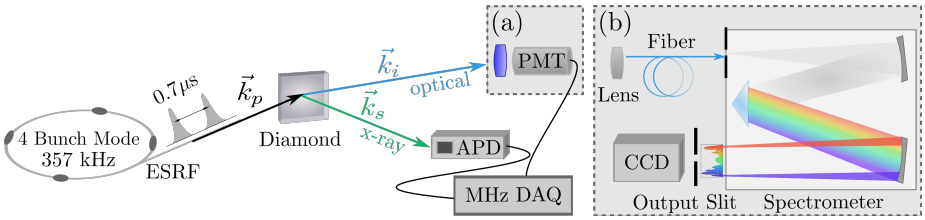

Figure 6: Schematics of the experimental setup for parallel detection of x-ray signal and optical idler photons at ESRF, which is operated in 4-bunch mode (357 kHz). The down-converted photon pair is generated in the diamond sample crystal. X-ray photons are filtered by analyzer crystal and the optical photons are focused into an optical fiber leading to the entrance slit of the optical spectrometer. The spectrum is detected by a CCD camera (b). Alternatively, the optical wavelength range is selected by an optical filter and detected via the PMT. For coincidence, the x-ray and visible detector are connected to the data acquisition system (DAQ).

(Figure 6 a) for coincidence detection. The PMT is positioned at the same position as the lens and optical fiber, the photosensor has a diameter of 25 mm, and thereby covers almost the same solid angle as the lens. A bandpass filter with a central wavelength of 620 nm ($\pm$20 nm) is positioned in front of the PMT to reduce count rates of different optical wavelengths. The photomultiplier is capable of working in the single photon counting regime. It yields a rise and decay time of 2.5 ns and a pulse width of 5 ns (200 MHz bandwidth). The PMT is sensitive in the optical range from 300 nm to 700 nm.

In summary, the coincidence detection could not successively be applied to study the XPDC process due to two main reasons: First, since the XPDC signal could not clearly be distinguished from elastic background effects. Second, also on the optical detection side, the potential optical idler photons could not effectively be distinguished from the fluorescent photons. In combination these findings made the application of a coincidence setup, as presented here, not feasible. However, if an additional method or parameter (e.g., polarization of the photons) would be found to effectively separate the converted photons, a coincidence detection would be possible.

X-ray Induced Optical Fluorescence

With the optical spectrometer described in Appendix 8.2.4 the x-ray induced emission of the diamond crystal is measured (Figure 7) at ID20 beamline at ESRF. The emis-

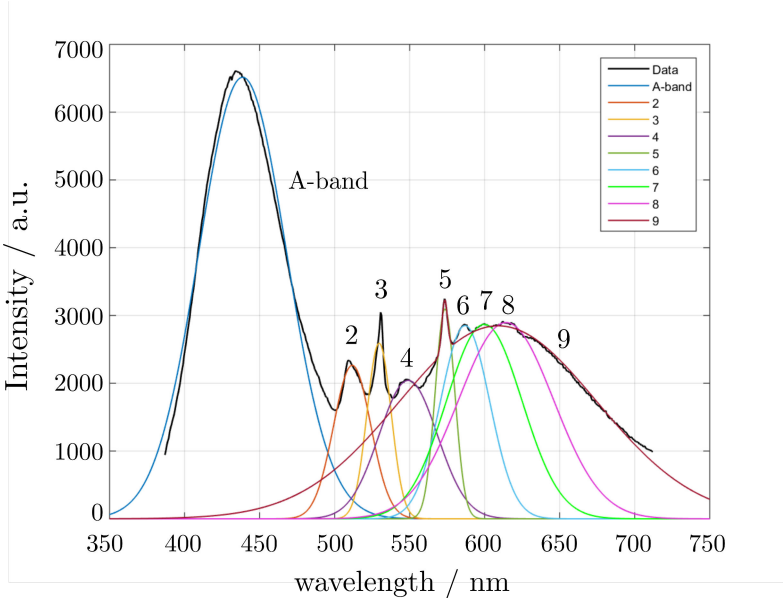

Figure 7: X-ray induced emission of diamond sample. The crystal is illuminated with 11 keV and the visible emission is measured via the optical spectrometer. Clearly observable is the strong contribution of the 'A-band' with its central wavelength of 420 nm. The emission band is attributed to transitions at dislocations. Next to a variety of smaller peaks a broad pronounced peak is observable at 620 nm.

sion spectrum exhibits two broad and several less pronounced peaks (Figure 7). The strongest feature is found around 440 nm and a weaker, yet broad peak at 620 nm.
The first peak can be attributed to the so called *A-band* [155], which is typically a relatively narrow peak at 440 nm. This peak is usually observed at low-nitrogen type

II diamonds and the fluorescence stems from purely non-decorated dislocations of the diamond lattice. The peaks' intensity by reducing the amount of nitrogen within the sample.
The second peak at 620 nm is most typically caused by transitions from nitrogen atoms located next to vacancies and is referred to as *NV-0* [155]. Furthermore, there are several narrow peaks within this wavelength range, which can be attributed to combinations of impurities and dislocations. Defect centers are denoted by H3 and H4. The H3 defect defect center is the most commonly optical feature observed for natural diamonds [156], but is also detected for synthetic diamonds. The H4 defect center also originates from nitrogen atoms in combination with vacancies, but in another geometry [157]. An assignment of all detected peaks within the visible spectrum are listed in Table 3.
The peaks 5 to 8 are assigned to the zero phonon lines (ZPL) of the neutral nitrogen-

Feature	CWL data nm	CWL fit data nm	FWHM nm	Assignment
A-band	434	438.7	68.67	
2	509	511.7	29.28	H4 (512 nm)
3	530	529.6	18.94	H3
4	549	549.1	45.72	480 nm abs. band
5	573	573.6	15.43	ZPL NV-0
6	586	586.9	38.73	ZPL NV-0
7	600	599.7	59.40	ZPL NV-0
8	617	614.3	74.49	ZPL NV-0
9	611	608.9	159.52	480 nm abs. band

Table 3: Description and assignment of detected fluorescent emission contributions for diamond sample irradiated wit 11 keV x-rays. The zero-phonon-lines (ZPL) of the nitrogen-vacancies are given.

vacancy center.
Additional and detailed information on the nature and origin of luminescent effects within diamond is found in the literature [158].

Bibliography

[1] C. Giacovazzo, H. L. Monaco, G. Artioli, D. Viterbo, G. Ferraris, and C. Giacovazzo, *Fundamentals of crystallography*, vol. 7. Oxford University Press Oxford, 2002.

[2] J. Als-Nielsen and D. McMorrow, *Elements of modern X-ray physics*. John Wiley & Sons, 2011.

[3] P. Ewald, "Introduction to the dynamical theory of x-ray diffraction," *Acta Crystallographica Section A: Crystal Physics, Diffraction, Theoretical and General Crystallography*, vol. 25, no. 1, pp. 103–108, 1969.

[4] Y. Shvyd'Ko, *X-ray Optics: High-energy-resolution Applications*, vol. 98. Springer, 2013.

[5] M. H. Rubin, D. N. Klyshko, Y. Shih, and A. Sergienko, "Theory of two-photon entanglement in type-ii optical parametric down-conversion," *Physical Review A*, vol. 50, no. 6, p. 5122, 1994.

[6] T. E. Keller and M. H. Rubin, "Theory of two-photon entanglement for spontaneous parametric down-conversion driven by a narrow pump pulse," *Physical Review A*, vol. 56, no. 2, p. 1534, 1997.

[7] Y. Shih, A. Sergienko, M. H. Rubin, T. Kiess, and C. Alley, "Two-photon entanglement in type-ii parametric down-conversion," *Physical Review A*, vol. 50, no. 1, p. 23, 1994.

[8] I. Freund and B. Levine, "Parametric conversion of x-rays," *Physical Review Letters*, vol. 23, no. 15, p. 854, 1969.

[9] B. Levine and I. Freund, "Parametric down conversion of x-rays," *Optics Communications*, vol. 1, no. 9, pp. 419–422, 1970.

[10] J. Armstrong, N. Bloembergen, J. Ducuing, and P. Pershan, "Interactions between light waves in a nonlinear dielectric," *Physical review*, vol. 127, no. 6, p. 1918, 1962.

[11] D. Kleinman, "Theory of optical parametric noise," *Physical Review*, vol. 174, no. 3, p. 1027, 1968.

[12] A. H. Compton, "Scattering of x-ray quanta and the j phenomena," *Nature*, vol. 113, no. 2831, pp. 160–161, 1924.

[13] Z. G. Pinsker, "Dynamical scattering of x-rays in crystals," 1978.

[14] P. Debye, "Interferenz von röntgenstrahlen und wärmebewegung," *Annalen der Physik*, vol. 348, no. 1, pp. 49–92, 1913.

[15] I. Waller, "Zur frage der einwirkung der wärmebewegung auf die interferenz von röntgenstrahlen," *Zeitschrift für Physik*, vol. 17, no. 1, pp. 398–408, 1923.

[16] P. Eisenberger and S. McCall, "X-ray parametric conversion," *Physical Review Letters*, vol. 26, no. 12, p. 684, 1971.

[17] P. Eisenberger and S. McCall, "Mixing of x-ray and optical photons," *Physical Review A*, vol. 3, no. 3, p. 1145, 1971.

[18] Y. Yoda, T. Suzuki, X.-W. Zhang, K. Hirano, and S. Kikuta, "X-ray parametric scattering by a diamond crystal," *Journal of synchrotron radiation*, vol. 5, no. 3, pp. 980–982, 1998.

[19] B. Adams, P. Fernandez, W.-K. Lee, G. Materlik, D. M. Mills, and D. V. Novikov, "Parametric down conversion of x-ray photons," *Journal of synchrotron radiation*, vol. 7, no. 2, pp. 81–88, 2000.

[20] B. Adams, Y. Nishino, D. Novikov, G. Materlik, and D. Mills, "Parametric down conversion of x-rays, recent experiments," *Nuclear Instruments and Methods in Physics Research Section A: Accelerators, Spectrometers, Detectors and Associated Equipment*, vol. 467, pp. 1019–1020, 2001.

[21] S. Shwartz, M. Fuchs, J. Hastings, Y. Inubushi, T. Ishikawa, T. Katayama, D. Reis, T. Sato, K. Tono, M. Yabashi, *et al.*, "X-ray second harmonic generation," *Physical review letters*, vol. 112, no. 16, p. 163901, 2014.

[22] P. Chakraborti, B. Senfftleben, B. Kettle, S. Teitelbaum, P. Bucksbaum, S. Ghimire, J. Hastings, H. Liu, S. Nelson, T. Sato, *et al.*, "Multiple fourier component analysis of x-ray second harmonic generation in diamond," *arXiv preprint arXiv:1903.02824*, 2019.

[23] A. Nazarkin, S. Podorov, I. Uschmann, E. Förster, and R. Sauerbrey, "Nonlinear optics in the angstrom regime: Hard-x-ray frequency doubling in perfect crystals," *Physical Review A*, vol. 67, no. 4, p. 041804, 2003.

[24] P. Franken and J. Ward, "Optical harmonics and nonlinear phenomena," *Reviews of Modern Physics*, vol. 35, no. 1, p. 23, 1963.

[25] I. Freund, "Nonlinear diffraction," *Physical Review Letters*, vol. 21, no. 19, p. 1404, 1968.

[26] C. Doppler, *Über das farbige Licht der Doppelsterne und einiger anderer Gestirne des Himmels*. 1842.

[27] I. Freund, "Nonlinear x-ray diffraction. determination of valence electron charge distributions," *Chemical Physics Letters*, vol. 12, no. 4, pp. 583–588, 1972.

[28] A. M. Zarubin, "Three-dimensional generalization of the van cittert-zernike theorem to wave and particle scattering," *Optics communications*, vol. 100, no. 5-6, pp. 491–507, 1993.

[29] H. Danino and I. Freund, "Parametric down conversion of x rays into the extreme ultraviolet," *Physical Review Letters*, vol. 46, no. 17, p. 1127, 1981.

[30] W. K. Tobiska and A. A. Nusinov, "Status of iso draft international standard for determining solar irradiances (dis 21348)," *J. Adv. Space Research*, 2005.

[31] "LiF attenuation length, howpublished = `http://henke.lbl.gov/cgi-bin/atten.pl`, note = Accessed: 2020-04-17."

[32] "LiF Bragg angle at Cu - K_α emission line, howpublished = `https://x-server.gmca.aps.anl.gov/`, note = Accessed: 2020-04-17."

[33] K. Tamasaku and T. Ishikawa, "Interference between compton scattering and x-ray parametric down-conversion," *Physical review letters*, vol. 98, no. 24, p. 244801, 2007.

[34] K. Tamasaku and T. Ishikawa, "Idler energy dependence of nonlinear diffraction in x$\rightarrow$ x+ euv parametric down-conversion," *Acta Crystallographica Section A: Foundations of Crystallography*, vol. 63, no. 5, pp. 437–438, 2007.

[35] K. Tamasaku, K. Sawada, and T. Ishikawa, "Determining x-ray nonlinear susceptibility of diamond by the optical fano effect," *Physical review letters*, vol. 103, no. 25, p. 254801, 2009.

[36] K. Tamasaku, et al., "Visualizing the local optical response to extreme-ultraviolet radiation with a resolution of $\lambda/380$," *Nature physics*, vol. 7, no. 9, pp. 705–708, 2011.

[37] K. Tamasaku, T. Ueda, D. Miwa, and T. Ishikawa, "Goniometric and topographic characterization of synthetic iia diamonds," *Journal of Physics D: Applied Physics*, vol. 38, no. 10A, p. A61, 2005.

[38] U. Fano, "Effects of configuration interaction on intensities and phase shifts," *Physical Review*, vol. 124, no. 6, p. 1866, 1961.

[39] B. Levine and I. Freund, "Double quantum scattering of x rays," *Optics Communications*, vol. 3, no. 4, pp. 197–200, 1971.

[40] B. Barbiellini, Y. Joly, and K. Tamasaku, "Explaining the x-ray nonlinear susceptibility of diamond and silicon near absorption edges," *Physical Review B*, vol. 92, no. 15, p. 155119, 2015.

[41] A. Volkov, P. Macchi, L. Farrugia, C. Gatti, P. Mallinson, T. Richter, and T. Koritsanszky, "Xd2006-a computer program package for multipole refinement, topological analysis of charge densities and evaluation of intermolecular energies from experimental and theoretical structure factors," *University at Buffalo, State University of New York, NY, USA*, 2006.

[42] B. L. Henke, E. M. Gullikson, and J. C. Davis, "X-ray interactions: photoabsorption, scattering, transmission, and reflection at e= 50-30,000 ev, z= 1-92," *Atomic data and nuclear data tables*, vol. 54, no. 2, pp. 181–342, 1993.

[43] T. Glover, D. Fritz, M. Cammarata, T. Allison, S. Coh, J. Feldkamp, H. Lemke, D. Zhu, Y. Feng, R. Coffee, *et al.*, "X-ray and optical wave mixing," *Nature*, vol. 488, no. 7413, p. 603, 2012.

[44] E. Shwartz and S. Shwartz, "Difference-frequency generation of optical radiation from two-color x-ray pulses," *Optics express*, vol. 23, no. 6, pp. 7471–7480, 2015.

[45] I. Freund and B. Levine, "The polarization properties of the parametric decay of x-rays," *Physics Letters A*, vol. 31, no. 8, pp. 456–457, 1970.

[46] D. N. Klyshko, *Photons Nonlinear Optics*. Routledge, 2018.

[47] S. Shwartz and S. Harris, "Polarization entangled photons at x-ray energies," *Physical review letters*, vol. 106, no. 8, p. 080501, 2011.

[48] J. Stöhr, "Two-photon x-ray diffraction," *Physical review letters*, vol. 118, no. 2, p. 024801, 2017.

[49] D. Strekalov, A. Sergienko, D. Klyshko, and Y. Shih, "Observation of two-photon "ghost" interference and diffraction," *Physical review letters*, vol. 74, no. 18, p. 3600, 1995.

[50] D. Pelliccia, A. Rack, M. Scheel, V. Cantelli, and D. M. Paganin, "Experimental x-ray ghost imaging," *Physical review letters*, vol. 117, no. 11, p. 113902, 2016.

[51] Z. Li, N. Medvedev, H. N. Chapman, and Y. Shih, "Radiation damage free ghost diffraction with atomic resolution," *Journal of Physics B: Atomic, Molecular and Optical Physics*, vol. 51, no. 2, p. 025503, 2017.

[52] A. Schori, D. Borodin, K. Tamasaku, and S. Shwartz, "Ghost imaging with paired x-ray photons," *Physical Review A*, vol. 97, no. 6, p. 063804, 2018.

[53] D. Krebs and N. Rohringer, "Quantum theory of x-ray parametric processes." manuscript in preparation.

[54] W. Eberhardt, "Synchrotron radiation: A continuing revolution in x-ray science—diffraction limited storage rings and beyond," *Journal of Electron Spectroscopy and Related Phenomena*, vol. 200, pp. 31–39, 2015.

[55] W. C. Röntgen, *Wilhelm Conrad Röntgen: Über eine neue Art von Strahlen. Drei Aufsätze über die Entdeckung der Röntgenstrahlen*. SEVERUS Verlag, 2012.

[56] H. Winick and A. Bienenstock, "Synchrotron radiation research," *Annual Review of Nuclear and Particle Science*, vol. 28, no. 1, pp. 33–113, 1978.

[57] J. Schwinger, "On the classical radiation of accelerated electrons," *Physical review*, vol. 75, no. 12, p. 1912, 1949.

[58] S. Glenzer, L. Fletcher, E. Galtier, B. Nagler, R. Alonso-Mori, B. Barbrel, S. Brown, D. Chapman, Z. Chen, C. Curry, *et al.*, "Matter under extreme conditions experiments at the linac coherent light source," *Journal of Physics B: Atomic, Molecular and Optical Physics*, vol. 49, no. 9, p. 092001, 2016.

[59] M. Eriksson, J. F. van der Veen, and C. Quitmann, "Diffraction-limited storage rings–a window to the science of tomorrow," *Journal of synchrotron radiation*, vol. 21, no. 5, pp. 837–842, 2014.

[60] P. F. Tavares, S. C. Leemann, M. Sjöström, and Å. Andersson, "The max iv storage ring project," *Journal of synchrotron radiation*, vol. 21, no. 5, pp. 862–877, 2014.

[61] P. Raimondi, "Esrf-ebs: The extremely brilliant source project," *Synchrotron Radiation News*, vol. 29, no. 6, pp. 8–15, 2016.

[62] M. Altarelli, R. Brinkmann, M. Chergui, W. Decking, B. Dobson, S. Düsterer, G. Grübel, W. Graeff, H. Graafsma, J. Hajdu, *et al.*, "The european x-ray free-electron laser technical design report," *DESY*, vol. 97, no. 2006, p. 4, 2006.

[63] W. Decking and T. Limberg, "European xfel post-tdr description," *XFEL. EU TN-2013-004-01, European XFEL GmbH, Hamburg, Germany*, 2013.

[64] W. Decking, S. Abeghyan, P. Abramian, A. Abramsky, A. Aguirre, C. Albrecht, P. Alou, M. Altarelli, P. Altmann, K. Amyan, *et al.*, "A mhz-repetition-rate hard x-ray free-electron laser driven by a superconducting linear accelerator," *Nature Photonics*, pp. 1–7, 2020.

[65] I. Inoue, T. Hara, Y. Inubushi, K. Tono, T. Inagaki, T. Katayama, Y. Amemiya, H. Tanaka, and M. Yabashi, "X-ray hanbury brown-twiss interferometry for determination of ultrashort electron-bunch duration," *Physical Review Accelerators and Beams*, vol. 21, no. 8, p. 080704, 2018.

[66] M. Yabashi, H. Tanaka, and T. Ishikawa, "Overview of the sacla facility," *Journal of synchrotron radiation*, vol. 22, no. 3, pp. 477–484, 2015.

[67] G. Geloni, E. Saldin, L. Samoylova, E. Schneidmiller, H. Sinn, T. Tschentscher, and M. Yurkov, "Coherence properties of the european xfel," *New Journal of Physics*, vol. 12, no. 3, p. 035021, 2010.

[68] J. Feldhaus, E. Saldin, J. Schneider, E. Schneidmiller, and M. Yurkov, "Possible application of x-ray optical elements for reducing the spectral bandwidth of an x-ray sase fel," *Optics Communications*, vol. 140, no. 4-6, pp. 341–352, 1997.

[69] E. Saldin, E. Schneidmiller, Y. V. Shvyd'ko, and M. Yurkov, "X-ray fel with a mev bandwidth," in *AIP Conference Proceedings*, vol. 581, pp. 153–161, American Institute of Physics, 2001.

[70] J. Amann, W. Berg, V. Blank, F.-J. Decker, Y. Ding, P. Emma, Y. Feng, J. Frisch, D. Fritz, J. Hastings, *et al.*, "Demonstration of self-seeding in a hard-x-ray free-electron laser," *Nature photonics*, vol. 6, no. 10, pp. 693–698, 2012.

[71] I. Inoue, T. Osaka, T. Hara, T. Tanaka, T. Inagaki, T. Fukui, S. Goto, Y. Inubushi, H. Kimura, R. Kinjo, *et al.*, "Generation of narrow-band x-ray free-electron laser via reflection self-seeding," *Nature Photonics*, vol. 13, no. 5, pp. 319–322, 2019.

[72] G. Geloni, V. Kocharyan, and E. Saldin, "A novel self-seeding scheme for hard x-ray fels," *Journal of Modern Optics*, vol. 58, no. 16, pp. 1391–1403, 2011.

[73] S. Liu, W. Decking, V. Kocharyan, E. Saldin, S. Serkez, R. Shayduk, H. Sinn, and G. Geloni, "Preparing for high-repetition rate hard x-ray self-seeding at the european x-ray free electron laser: Challenges and opportunities," *Physical Review Accelerators and Beams*, vol. 22, no. 6, p. 060704, 2019.

[74] A. H. Compton, S. K. Allison, *et al.*, "X-rays in theory and experiment," 1935.

[75] W. H. Zachariasen *et al.*, "Theory of x-ray diffraction in crystals," 1945.

[76] A. Authier, "Dynamical theory of x-ray diffraction," *International Tables for Crystallography*, pp. 626–646, 2006.

[77] C. G. Darwin, "Xxxiv. the theory of x-ray reflexion," *The London, Edinburgh, and Dublin Philosophical Magazine and Journal of Science*, vol. 27, no. 158, pp. 315–333, 1914.

[78] L. Rebuffi and M. S. del Rio, "Oasys (orange synchrotron suite): an open-source graphical environment for x-ray virtual experiments," in *Advances in Computational Methods for X-Ray Optics IV*, vol. 10388, p. 103880S, International Society for Optics and Photonics, 2017.

[79] P. Debye, "Zur theorie der spezifischen wärmen," *Annalen der Physik*, vol. 344, no. 14, pp. 789–839, 1912.

[80] M. Sánchez del Río, N. Canestrari, F. Jiang, and F. Cerrina, "Shadow3: A new version of the synchrotron x-ray optics modelling package," *Journal of synchrotron radiation*, vol. 18, pp. 708–16, 09 2011.

[81] L. Rebuffi and M. Sánchez del Río, "Shadowoui: a new visual environment for x-ray optics and synchrotron beamline simulations," *Journal of synchrotron radiation*, vol. 23, no. 6, pp. 1357–1367, 2016.

[82] O. Diat, P. Bösecke, C. Ferrero, A. Freund, J. Lambard, and R. Heintzmann, "Ultra-small-angle x-ray scattering with a bonse-hart camera on the high brilliance beamline at the esrf," *Nuclear Instruments and Methods in Physics Research Section A: Accelerators, Spectrometers, Detectors and Associated Equipment*, vol. 356, no. 2-3, pp. 566–572, 1995.

[83] "Hochaufloesende Beugung vorlesung 07." `http://lehre.ikz-berlin.de/physhu/scripte/roentgen/Vorlesung07_Hochaufloesende_Beugung_presentation.pdf`. Accessed: 2020-03-13.

[84] S. Huotari, C. J. Sahle, C. Henriquet, A. Al-Zein, K. Martel, L. Simonelli, R. Verbeni, H. Gonzalez, M.-C. Lagier, C. Ponchut, *et al.*, "A large-solid-angle x-ray raman scattering spectrometer at id20 of the european synchrotron radiation facility," *Journal of synchrotron radiation*, vol. 24, no. 2, pp. 521–530, 2017.

[85] C. Ponchut, J. Rigal, J. Clément, E. Papillon, A. Homs, and S. Petitdemange, "Maxipix, a fast readout photon-counting x-ray area detector for synchrotron applications," *Journal of Instrumentation*, vol. 6, no. 01, p. C01069, 2011.

[86] S. P. Collins, A. Bombardi, A. R. Marshall, J. H. Williams, G. Barlow, A. G. Day, M. R. Pearson, R. J. Woolliscroft, R. D. Walton, G. Beutier, and G. Nisbet, "Diamond beamline i16 (materials & magnetism)," *AIP Conference Proceedings*, vol. 1234, no. 1, pp. 303–306, 2010.

[87] M. Moretti Sala, K. Martel, C. Henriquet, A. Al Zein, L. Simonelli, C. Sahle, H. Gonzalez, M.-C. Lagier, C. Ponchut, S. Huotari, *et al.*, "A high-energy-resolution resonant inelastic x-ray scattering spectrometer at id20 of the european synchrotron radiation facility," *Journal of synchrotron radiation*, vol. 25, no. 2, pp. 580–591, 2018.

[88] A. M. Zaitsev, *Optical properties of diamond: a data handbook*. Springer Science & Business Media, 2013.

[89] W. Saslow, T. Bergstresser, and M. L. Cohen, "Band structure and optical properties of diamond," *Physical Review Letters*, vol. 16, no. 9, p. 354, 1966.

[90] C. A. Klein and R. DeSalvo, "Thresholds for dielectric breakdown in laser-irradiated diamond," *Applied physics letters*, vol. 63, no. 14, pp. 1895–1897, 1993.

[91] F. Uhlén, D. Nilsson, A. Holmberg, H. M. Hertz, C. G. Schroer, F. Seiboth, J. Patommel, V. Meier, R. Hoppe, A. Schropp, *et al.*, "Damage investigation on tungsten and diamond diffractive optics at a hard x-ray free-electron laser," *Optics express*, vol. 21, no. 7, pp. 8051–8061, 2013.

[92] A. M. Khounsary, R. K. Smither, S. Davey, and A. Purohit, "Diamond monochromator for high heat flux synchrotron x-ray beams," in *High Heat Flux*

Engineering, vol. 1739, pp. 628–642, International Society for Optics and Photonics, 1993.

[93] S. Colbran, *Element Six CVD Diamond Handbook*. 07 2019.

[94] A. Schori, C. Bömer, D. Borodin, S. Collins, B. Detlefs, M. M. Sala, S. Yudovich, and S. Shwartz, "Parametric down-conversion of x rays into the optical regime," *Physical review letters*, vol. 119, no. 25, p. 253902, 2017.

[95] "FMB Oxford APD technical description." `https://www.fmb-oxford.com/wp-content/uploads/bsk-pdf-manager/APDs_March_2019_23.pdf`. Accessed: 2020-01-13.

[96] A. Mikhalychev, A. Benediktovitch, T. Ulyanenkova, and A. Ulyanenkov, "Ab initio simulation of diffractometer instrumental function for high-resolution x-ray diffraction," *Journal of applied crystallography*, vol. 48, no. 3, pp. 679–689, 2015.

[97] U. Pietsch, V. Holy, and T. Baumbach, *High-Resolution X-Ray Scattering*. Springer-Verlag New York, 2 ed., 2004.

[98] F. J. Duarte, "Multiple-prism grating solid-state dye laser oscillator: optimized architecture," *Applied optics*, vol. 38, no. 30, pp. 6347–6349, 1999.

[99] T. Niebauer, J. E. Faller, H. Godwin, J. L. Hall, and R. Barger, "Frequency stability measurements on polarization-stabilized he–ne lasers," *Applied optics*, vol. 27, no. 7, pp. 1285–1289, 1988.

[100] "Diamond crystal structure, howpublished = `http://lampx.tugraz.at/~hadley/ss1/crystalstructure/structures/diamond/diamond.php`, note = Accessed: 2020-01-15."

[101] A. Papadopoulos and E. Anastassakis, "Optical properties of diamond," *Physical Review B*, vol. 43, no. 6, p. 5090, 1991.

[102] D. Borodin, S. Levy, and S. Shwartz, "High energy-resolution measurements of x-ray into ultraviolet parametric down-conversion with an x-ray tube source," *Applied Physics Letters*, vol. 110, no. 13, p. 131101, 2017.

[103] D. Borodin, A. Schori, J.-P. Rueff, J. Ablett, and S. Shwartz, "Evidence for collective nonlinear interactions in x ray into ultraviolet parametric down-conversion," *Physical Review Letters*, vol. 122, no. 2, p. 023902, 2019.

[104] S. Sofer, O. Sefi, E. Strizhevsky, H. Aknin, S. Collins, G. Nisbet, B. Detlefs, C. J. Sahle, and S. Shwartz, "Observation of strong nonlinear interactions in parametric down-conversion of x-rays into ultraviolet radiation," *Nature Communications*, vol. 10, no. 1, pp. 1–8, 2019.

[105] R. W. Cheary, A. A. Coelho, and J. P. Cline, "Fundamental parameters line profile fitting in laboratory diffractometers," *Journal of Research of the National Institute of Standards and Technology*, vol. 109, no. 1, p. 1, 2004.

[106] A. Zuev, "Calculation of the instrumental function in x-ray powder diffraction," *Journal of applied crystallography*, vol. 39, no. 3, pp. 304–314, 2006.

[107] O. Masson, E. Dooryhée, and A. Fitch, "Instrument line-profile synthesis in high-resolution synchrotron powder diffraction," *Journal of applied crystallography*, vol. 36, no. 2, pp. 286–294, 2003.

[108] S. Lambert and F. Guillet, "Application of the x-ray tracing method to powder diffraction line profiles," *Journal of Applied Crystallography*, vol. 41, no. 1, pp. 153–160, 2008.

[109] L. Rebuffi and P. Scardi, "Calculation of the instrumental profile function for a powder diffraction beamline used in nanocrystalline material research," in *Advances in Computational Methods for X-Ray Optics III*, vol. 9209, p. 92090J, International Society for Optics and Photonics, 2014.

[110] L. Rebuffi, M. Sánchez del Río, E. Busetto, and P. Scardi, "Understanding the instrumental profile of synchrotron radiation x-ray powder diffraction beamlines," *Journal of synchrotron radiation*, vol. 24, no. 3, pp. 622–635, 2017.

[111] D. Brüggemann and M. Bollig, "An efficient algorithm for frequency integration of voigt profiles," *Journal of Quantitative Spectroscopy and Radiative Transfer*, vol. 48, no. 1, pp. 111–114, 1992.

[112] P. Van der Sluis, "The three-dimensional resolution function of the four-reflection monochromator: a route to a higher intensity," *Journal of applied crystallography*, vol. 27, no. 1, pp. 50–55, 1994.

[113] F. Gozzo, A. Cervellino, M. Leoni, P. Scardi, A. Bergamaschi, and B. Schmitt, "Instrumental profile of mythen detector in debye-scherrer geometry," *Zeitschrift für Kristallographie Crystalline Materials*, vol. 225, no. 12, pp. 616–624, 2010.

[114] T. Sabine, "A powder diffractometer for a synchrotron source," *Journal of applied crystallography*, vol. 20, no. 3, pp. 173–178, 1987.

[115] A. Freund, J. Hoszowska, J. Sellschop, R. Burns, and M. Rebak, "An initial evaluation of high quality synthetic diamond single crystals for synchrotron x-ray monochromators," in *AIP Conference Proceedings*, vol. 521, pp. 242–246, American Institute of Physics, 2000.

[116] S. Polyakov, V. Denisov, N. Kuzmin, M. Kuznetsov, S. Y. Martyushov, S. Nosukhin, S. Terentiev, and V. Blank, "Characterization of top-quality type iia synthetic diamonds for new x-ray optics," *Diamond and Related Materials*, vol. 20, no. 5-6, pp. 726–728, 2011.

[117] N. Toda, H. Sumiya, S. Satoh, and T. Ishikawa, "High-quality synthetic diamonds for the monochromator of synchrotron radiation beams," in *High Heat Flux and Synchrotron Radiation Beamlines*, vol. 3151, pp. 329–336, International Society for Optics and Photonics, 1997.

[118] H. Johann, "Intense x-ray spectra obtained with concave crystals," *Z. Phys*, vol. 69, p. 185, 1931.

[119] Y.-R. Shen, "The principles of nonlinear optics," *New York, Wiley-Interscience, 1984, 575 p.*, 1984.

[120] W. Bartels, "Characterization of thin layers on perfect crystals with a multipurpose high resolution x-ray diffractometer," *Journal of Vacuum Science & Technology B: Microelectronics Processing and Phenomena*, vol. 1, no. 2, pp. 338–345, 1983.

[121] R. C. Chaney, E. E. Lafon, and C. C. Lin, "Energy band structure of lithium fluoride crystals by the method of tight binding," *Physical Review B*, vol. 4, no. 8, p. 2734, 1971.

[122] C. Jouanin and C. Gout, "Valence band structure of magnesium fluoride by the tight-binding method," *Journal of Physics C: Solid State Physics*, vol. 5, no. 15, p. 1945, 1972.

[123] R. A. Heaton and C. C. Lin, "Electronic energy-band structure of the calcium fluoride crystal," *Physical Review B*, vol. 22, no. 8, p. 3629, 1980.

[124] S. Maj, "Energy gap and density in sio 2 polymorphs," *Physics and chemistry of minerals*, vol. 15, no. 3, pp. 271–273, 1988.

[125] R. H. Brown and R. Q. Twiss, "A test of a new type of stellar interferometer on sirius," *Nature*, vol. 178, no. 4541, pp. 1046–1048, 1956.

[126] E. Gluskin, E. Alp, I. McNulty, W. Sturhahn, and J. Sutter, "A classical hanbury brown–twiss experiment with hard x-rays," *Journal of Synchrotron Radiation*, vol. 6, no. 5, pp. 1065–1066, 1999.

[127] Y. Kunimune, Y. Yoda, K. Izumi, M. Yabashi, X.-W. Zhang, T. Harami, M. Ando, and S. Kikuta, "Two-photon correlations in x-rays from a synchrotron radiation source," *Journal of synchrotron radiation*, vol. 4, no. 4, pp. 199–203, 1997.

[128] T. Pittman, Y. Shih, D. Strekalov, and A. V. Sergienko, "Optical imaging by means of two-photon quantum entanglement," *Physical Review A*, vol. 52, no. 5, p. R3429, 1995.

[129] S. Ragy and G. Adesso, "Nature of light correlations in ghost imaging," *Scientific reports*, vol. 2, p. 651, 2012.

[130] R. Shakhmuratov, F. Vagizov, V. Antonov, Y. Radeonychev, M. O. Scully, and O. Kocharovskaya, "Transformation of a single-photon field into bunches of pulses," *Physical Review A*, vol. 92, no. 2, p. 023836, 2015.

[131] J. C. Howell, R. S. Bennink, S. J. Bentley, and R. Boyd, "Realization of the einstein-podolsky-rosen paradox using momentum-and position-entangled photons from spontaneous parametric down conversion," *Physical Review Letters*, vol. 92, no. 21, p. 210403, 2004.

[132] A. Joobeur, B. E. Saleh, T. S. Larchuk, and M. C. Teich, "Coherence properties of entangled light beams generated by parametric down-conversion: Theory and experiment," *Physical Review A*, vol. 53, no. 6, p. 4360, 1996.

[133] J. S. Bell, "On the einstein podolsky rosen paradox," *Physics Physique Fizika*, vol. 1, no. 3, p. 195, 1964.

[134] A. Einstein, B. Podolsky, and N. Rosen, "Can quantum-mechanical description of physical reality be considered complete?," *Physical review*, vol. 47, no. 10, p. 777, 1935.

[135] J. F. Clauser and A. Shimony, "Bell's theorem. experimental tests and implications," *Reports on Progress in Physics*, vol. 41, no. 12, p. 1881, 1978.

[136] J. F. Clauser, M. A. Horne, A. Shimony, and R. A. Holt, "Proposed experiment to test local hidden-variable theories," *Physical review letters*, vol. 23, no. 15, p. 880, 1969.

[137] J. S. Bell, "Speakable and unspeakable in quantum mechanics," *Cambridge University*, 1987.

[138] P. G. Kwiat, A. M. Steinberg, and R. Y. Chiao, "High-visibility interference in a bell-inequality experiment for energy and time," *Physical Review A*, vol. 47, no. 4, p. R2472, 1993.

[139] J. Rarity and P. Tapster, "Experimental violation of bell's inequality based on phase and momentum," *Physical Review Letters*, vol. 64, no. 21, p. 2495, 1990.

[140] A. Garg and N. D. Mermin, "Detector inefficiencies in the einstein-podolsky-rosen experiment," *Physical Review D*, vol. 35, no. 12, p. 3831, 1987.

[141] W.-T. Liao and S. Ahrens, "Gravitational and relativistic deflection of x-ray superradiance," *Nature Photonics*, vol. 9, no. 3, p. 169, 2015.

[142] K. P. Heeg, J. Haber, D. Schumacher, L. Bocklage, H.-C. Wille, K. S. Schulze, R. Loetzsch, I. Uschmann, G. G. Paulus, R. Rüffer, *et al.*, "Tunable subluminal propagation of narrow-band x-ray pulses," *Physical review letters*, vol. 114, no. 20, p. 203601, 2015.

[143] K. P. Heeg, C. Ott, D. Schumacher, H.-C. Wille, R. Röhlsberger, T. Pfeifer, and J. Evers, "Interferometric phase detection at x-ray energies via fano resonance control," *Physical review letters*, vol. 114, no. 20, p. 207401, 2015.

[144] X. Kong, W.-T. Liao, and A. Palffy, "Field control of single x-ray photons in nuclear forward scattering," *New Journal of Physics*, vol. 16, no. 1, p. 013049, 2014.

[145] S. Mukamel, M. Freyberger, W. P. Schleich, M. Bellini, A. Zavatta, G. Leuchs, C. Silberhorn, R. W. Boyd, L. S. Soto, A. Stefanov, *et al.*, "Roadmap on quantum light spectroscopy," *Journal of Physics B: Atomic, Molecular and Optical Physics*, 2020.

[146] K. E. Dorfman, F. Schlawin, and S. Mukamel, "Nonlinear optical signals and spectroscopy with quantum light," *Reviews of Modern Physics*, vol. 88, no. 4, p. 045008, 2016.

[147] J. R. Rouxel, M. Kowalewski, K. Bennett, and S. Mukamel, "X-ray sum frequency diffraction for direct imaging of ultrafast electron dynamics," *Physical Review Letters*, vol. 120, no. 24, p. 243902, 2018.

[148] S. Collins, A. Bombardi, A. Marshall, J. Williams, G. Barlow, A. Day, M. Pearson, R. Woolliscroft, R. Walton, G. Beutier, *et al.*, "Diamond beamline i16 (materials & magnetism)," in *AIP Conference Proceedings*, vol. 1234, pp. 303–306, American Institute of Physics, 2010.

[149] "Beamline characteristics ID20, ESRF, howpublished = `https://www.esrf.eu/home/usersandscience/experiments/emd/id20/beamline-characteristics.html`, note = Accessed: 2020-06-04."

[150] "Beamline characteristics P08, Petra III, howpublished = `https://photon-science.desy.de/facilities/petra_iii/beamlines/p08_highres_diffraction/unified_data_sheet_p08/index_eng.html`, note = Accessed: 2020-06-04."

[151] P. Kraft, A. Bergamaschi, C. Broennimann, R. Dinapoli, E. Eikenberry, B. Henrich, I. Johnson, A. Mozzanica, C. Schlepütz, P. Willmott, *et al.*, "Performance of single-photon-counting pilatus detector modules," *Journal of synchrotron radiation*, vol. 16, no. 3, pp. 368–375, 2009.

[152] A. Britz, T. A. Assefa, A. Galler, W. Gawelda, M. Diez, P. Zalden, D. Khakhulin, B. Fernandes, P. Gessler, H. Sotoudi Namin, *et al.*, "A multi-mhz single-shot data acquisition scheme with high dynamic range: pump–probe x-ray experiments at synchrotrons," *Journal of synchrotron radiation*, vol. 23, no. 6, pp. 1409–1423, 2016.

[153] "SpectraPro 2150 Monochromators and Spectrographs, howpublished = `https://www.princetoninstruments.com/userfiles/files/assetlibrary/datasheets-spectroscopy/princeton_instruments_spectrapro-2150-q2-7-29-19.pdf`, note = Accessed: 2020-03-31."

[154] "ProEM-HS:512:BX3, howpublished = `https://www.princetoninstruments.com/userfiles/files/assetlibrary/datasheets/proem-hs-512-p4-7-7-16.pdf`, note = Accessed: 2020-03-31."

[155] M. Gaft, R. Reisfeld, and G. Panczer, *Modern luminescence spectroscopy of minerals and materials*. Springer, 2015.

[156] C.-K. Lin, H.-C. Chang, M. Hayashi, and S. Lin, "Excitation properties of the h3 defect center in diamond: A theoretical study," *Chemical Physics Letters*, vol. 475, no. 1-3, pp. 68–72, 2009.

[157] A. Collins, M. Thomaz, and M. Jorge, "Excitation and decay of h4 luminescence in diamond," *Journal of Physics C: Solid State Physics*, vol. 16, no. 28, p. 5417, 1983.

[158] M. W. Doherty, N. B. Manson, P. Delaney, F. Jelezko, J. Wrachtrup, and L. C. Hollenberg, "The nitrogen-vacancy colour centre in diamond," *Physics Reports*, vol. 528, no. 1, pp. 1–45, 2013.

Acknowledgments

This thesis and especially the presented experiments were enabled by the contributions and affords of many, to whom I would like to address my gratitude.

First of all, I would like to thank Prof. Dr. Christian Bressler for giving me the opportunity to conduct a PhD thesis at European XFEL. I appreciate the encouragement and the many degrees of freedom he provided to follow my curiosity to explore the field of x-ray nonlinearities. In this context I would like to thank Dr. Andreas Galler for his ongoing support of this project; from its earliest stages, via proposal writing, beamtime preparation and conduction to finally discussion of the data analysis.
Furthermore, I like to thank Prof. Dr. Nina Rohringer in the first approximation for becoming my second supervisor, but in addition for her boundless and ongoing support, for providing creative feedback and stimulating ideas.
I would like to thank Prof. Dr. Wilfried Wurth (who sadly passed away) for supporting a bold idea.
My warmest thanks goes to those, who made my doctorate time worthwhile, enjoyable and a constant adventure: my fellow students and colleagues. A special thanks to Michael Diez, Florian Otte, Tae Kyu Choi and Manuel Harder for joining and surviving the numerous beamtimes all over the world - at both day and night time. You are the fantastic four. It has been a great pleasure to work with you.
A very special thanks, for yet the smallest contribution (efficiencies as low as 10^{-16}) go to Dietrich Krebs for his theoretical support, (almost) endless discussions, the first joint conference talk and finally for the courage to dare a collaboration with an experimentalist.
I like to express my gratitude to all members of the FXE group of European XFEL for their help, support and advises throughout the years. A special thanks is to be addressed to Paul Frankenberger, who engineered essential parts in various implementations and who supported the project by constructive engineering.
Marco Schrage and Sandra Rost from the mechanical workshop managed to produce parts and adapters always in time and incredible precision, for which I am very thankful.
The famous support of the XFEL IT team needs to be mentioned, namely Bartosz Poljancewicz, who saved me several times from password struggle or with immediate help in case of disappeared hardware. In addition, I would like to thank Frank Babies for helping to implement acquisition electronics under all circumstances.
A reoccurring thanks goes to the incredible beamline support at the ESRF during multi-

ple beamtimes: Dr. Marco Moretti, Dr. Christoph Sahle, Blanka Detlefs and Christian Henriquet. Merci bien.
At the Diamond Light Source I would like to thank Dr. Garth Nisbeth and Dr. Steve Collins for providing vital support. At Petra III I would like to say thanks to Dr. Florian Bertam from the P08 beamline together with Jonas Warias from the University of Kiel for supporting the risky undertaking of stimulating XPDC.
I would also like to express my gratitude towards Prof. Dr. Sharon Shwartz for inviting to, joining and sharing beamtimes at different sources and stimulating discussions.
I thank Prof. Dr. Ralf Röhlsberger and Dr. Yuri Shvyd'ko for interesting and fruitful discussions on high resolution x-ray optics and future projects.

Last but not least, möchte ich meinen Eltern und meiner Schwester für ihre immer währende Unterstützung danken. Ihr seid großartig.

Eidestattliche Erklärung

Hiermit erkläre ich an Eides statt, dass ich die vorliegende Dissertationsschrift selbst verfasst und keine anderen als die angegebenen Quellen und Hilfsmittel benutzt habe.

I hereby declare, on oath, that I have written the present dissertation by my own and have not used other than the acknowledged resources and aids.

Hamburg, den